UNIVERSITY OF CALIFORNIA

Los Angeles

Low dispersion, high spectral efficiency, RF photonic transmission systems and low loss grating couplers for Silicon-on-Insulator nanophotonic integrated circuits.

A dissertation submitted in partial satisfaction

of the requirements for the degree Doctor of Philosophy

in Electrical Engineering

by

Adithyaram Narasimha

2004

The dissertation of Adithyaram Narasimha is approved.

Bahram Jalali

Hong-Wen Jiang

Ming C. Wu

Eli Yablonovitch, Committee Chair

University of California, Los Angeles

2004

TABLE OF CONTENTS

List of Figures ……………………………………..……………………………vi

List of Tables ………………………………………………………………………ix

Acknowledgments …………………………………………………………...…..x

Vita ……………………………………………………………………………..xiv

Publications and Presentations ……………………………………………..xv

Abstract of the Dissertation …..…………………………………………..xvii

Chapter 1 Introduction ……………………………………………………………1

1.1 Motivation……………………………………………………………..1

1.2 The single sideband technique ……………………………………………..4

1.3 Organization of the thesis ……………………………………………….7

Chapter 2 Optical Single Sideband Modulation ……………………………..10

2.1 Introduction ……………………………………………………………10

2.2 Optical single sideband modulation …………………………………………10

2.3 Mathematical formulation of optical single sideband ………………………10

2.4 Dispersion performance of optical single sideband signal ………………….15

2.5 The case for *tandem* single sideband ………………………………………..15

Chapter 3 Tandem single sideband transmitter demonstration and evaluation …..17

3.1 Experimental Setup ……………………………………………….……17

3.2 Experimental Results …………………………………………………..…19

3.3 Performance evaluation of tandem single sideband modulator …………..…24

3.4 Discussion and Conclusion ……………………………………………..…29

Chapter 4 Tandem single sideband reception ………………………………………..…31

4.1 Experimental Setup and Principle of Operation ……………………………31

4.2 Experimental Results and Discussion …………………………………….…35

4.3 Conclusions ……………………………………………………………………40

Chapter 5 Multifunctional microwave fiber optic links ……………………………..42

5.1 RF frequency translation and doubling ……………………….…………43

5.2 RF spectral inversion over an RF photonic link ………………………..……45

5.3 Downconverting RF photonic link …………………………………………46

5.4 Code-selective RF photonic mixing ………………………………………47

5.5 Conclusions ……………………………………………………………………50

Chapter 6 Silicon-on-Insulator Nanophotonics ……………………………………...52

6.1 Silicon-on-Insulator Optoelectronics……………………...……………53

6.2 The Coupling Problem ……………………….………………………...55

6.3 Requirements from a fiber-IC interface ……………………………………56

6.4 Possible candidates ……………………………………………………57

6.5 Conclusions ……………………………………………………………………60

Chapter 7 Grating Coupler Design …………………………………......................61

7.1 The Design Problem……………………...……………………………63

7.2 Prior Work ………………………..………………………………………64

7.3 Momentum matching ……………………………………………………66

7.4 The grating as an array of scattering elements………………………………68

7.5 Reflection from a leaky wave surface……………………………………..73

7.6 Proof of concept design……………………...…………………………76

7.7 Designing the coupler for a given input beam ……………………..….……78

7.8 Proof of concept design parameters ……………………….…………..…80

7.9 Conclusions ……………………………………………………………82

Chapter 8 Fabrication of waveguide grating couplers……………………………....83

8.1 The high Δn material system……………………………………………….. 83

8.2 Waveguide fabrication ……………………….……………………………..85

8.3 Grating fabrication………………………………………………………..87

8.4 Conclusions………………………………………………………………93

Chapter 9 Characterization of waveguide grating couplers……………….........94

9.1 Experimental Parameters………………...………………………………..95

9.2 Experimental Setup ……………………….………………………………97

9.3 Experimental Results and Discussion………………………………………101

9.4 Conclusions……………………………………………………………106

Chapter 10 Conclusions………………...108

References …………………………………………………………………………..116

LIST OF FIGURES

Figure 1.1 Amplitude modulation produces an upper and lower sideband on either side of the carrier frequency……………………………………….5

Figure 1.2 A primitive way of achieving single sideband transmission………………...6

Figure 1.3 A method of generating electrical single sideband signals using balanced modulators and phase shifters……………………………………..6

Figure 1.4 A coherent communication system……………………………………….7

Figure 2.1 Block diagram of optical single sideband modulator…………………....11

Figure 2.2 Optical spectrum at output of single sideband modulator …………………12

Figure 2.3 a) Pure SSB systems need guardbands and b) Tandem single sideband signals enable carriers to be twice as far apart without wasting bandwidth…………………………………………………………………..16

Figure 3.1 Block diagram of tandem single sideband transmitter……………………..18

Figure 3.2 Spectral response of fiber grating filter……………………………………19

Figure 3.3 Sideband rejection obtained from dual-electrode modulator ……………...20

Figure 3.4 Received 500 Mb/s eye diagrams when both sidebands were reflected into photodetector……………………………………………………….21

Figure 3.5 BER curves when both sidebands were reflected into photodetector……...22

Figure 3.6 Received 500 Mb/s eye diagrams when only upper sideband was reflected into photodetector……………………………………………..23

Figure 3.7 BER curves when only upper sideband was reflected into photodetector…24

Figure 3.8 Inter-sideband cross-talk as a function of RF power mismatch……………26

Figure 3.9 Inter-sideband cross-talk as a function of bias deviation…………………..27

Figure 3.10 Inter-sideband cross-talk as a function of phase mismatch……………......28

Figure 3.11 Phase-bias compensation for inter-sideband cross-talk…………………...29

Figure 4.1 Block diagram of tandem single sideband receiver………………………..32

Figure 4.2 Receiver performance for purely LSB signals……………………………36

Figure 4.3 Receiver performance for tandem single sideband signals………………..37

Figure 4.4 BER data for a tandem single sideband transmission system……………..39

Figure 5.1 Output spectra for a frequency doubling TSSB link………………………44

Figure 5.2 Experimental setup to demonstrate code-selective RF photonic mixing…………………………………………………………………...48

Figure 5.3 Signal obtained at 6 GHz…………………………………………………..49

Figure 5.4 Signal obtained at 9 GHz……………………………………….…………50

Figure 6.1 The Silicon-on-Insulator material system……………………………………54

Figure 6.2 To scale representation of single mode fiber core next to photonic crystal waveguide…………………………………………………………………56

Figure 6.3 Schematic of an adiabatic taper……………………………………………58

Figure 6.4 Planar waveguide grating coupler……………………………………………59

Figure 7.1 The interfaces and structures surrounding a grating affect its coupling length……………………………………………………………….62

Figure 7.2 The Design Problem…………………………………………………………64

Figure 7.3 Momentum matching in grating couplers……………………………………67

Figure 7.4 The grating coupler in out-coupling configuration…………………………..68

Figure 7.5 A grating with a mirror underneath. This eliminates half the available phase space for the light to couple out into……………………...……………69

Figure 7.6 The grating as a series of scattering elements……………………………..71

Figure 7.7 The reflected beam has two components when the grating is excited by an input beam…………………………………………………………73

Figure 7.8 Input field profile as a function of scattering center…………………………74

Figure 7.9 Reflected beam profiles as a function of scattering center for various Coupling strengths………………………………………………………75

Figure 7.10 The high index contrast dielectric stack…………………………………….77

Figure 7.11 Reflection from a non-uniform grating coupler…………………………….79

Figure 7.12 Proof-of-concept design parameters and spectral performance…………….81

Figure 8.1 Simulated and measured reflectometry curves for the SOI wafer obtained from SOITEC, France………………...……………………………………84

Figure 8.2 Top view schematic and SEM image of waveguides fabricated on SOI chip……………………………………………………………...….86

Figure 8.3 Gratings may be fabricated by a) etching directly into the silicon waveguide or b) by housing them in an oxide layer deposited right above the waveguide………………………………………………………………87

Figure 8.4 Process flow for the fabrication of grating couplers…………………………88

Figure 8.5 Oxide reactive ion etch rate calibration………………………………………91

Figure 8.6 SEM micrographs of fabricated gratings……………………………………..92

Figure 9.1 Grating configurations for efficiency measurement………………………….95

Figure 9.2 Top view schematic of the sample…………………………………………...98

Figure 9.3 Block diagram and photograph of experimental setup………………………99

Figure 9.4.Waveguide loss calibration……………………………..………………..102

Figure 9.5 Plot of efficiency vs. insertion loss for grating coupler in dielectric stack…103

Figure 9.6 Insertion loss vs. deviation from optimum angle…………………………...104

Figure 9.7 Insertion loss vs. deviation in x position……………………………………105

Figure 9.8 Insertion loss vs. deviation in y position……………………………………105

LIST OF TABLES

Table 4.1 Heterodyning terms present after photodetector when no FFP is used……34

ACKNOWLEDGMENTS

This dissertation would not have been possible without the support, love and encouragement of my father, Honnalgere Narasimha, who has helped me make it through every phase in my life, and who has managed the extraordinary feat of being two parents wrapped in one.

I am deeply indebted to Prof. Eli Yablonovitch for introducing me to the field of physical electronics, and for his academic, financial and moral support throughout my stay in graduate school. I have learned much from his insights into science, industry, and his philosophy of research. Working with him over the course of my graduate career has been a huge opportunity and honor. My thanks are also due to Prof. Ming Wu for lab space, along with the test and measurement equipment necessary for some of the experiments, and for useful discussions during the initial phase of the tandem single sideband project. I thank Prof. Bahram Jalali and Prof. Hong-Wen Jiang, for sitting on my dissertation committee, and for coming without the slightest complaint to my early morning qualifying examination.

I owe a huge debt of gratitude to Xue Jun (Michael) Meng for his experimental assistance with fiber optic systems, for taking the time to teach me about optical components, and for acting as a mentor to me during my first couple of years at graduate school.

My colleagues from the Optoelectronics and Integrated Photonics Labs have given me a great deal of help and support over the years. In particular, I would like to thank Cedric Lam, for his initial mentoring and encouragement, Ivan Alvarado-

Rodriguez, for his many little nuggets of wisdom regarding the dry etching of dielectrics and III-V semiconductors, as well as for alignment strategies for bulk optical test-beds, Thomas Szkopek for being a valuable and ready sounding board for scientific ideas, Hans Robinson, for hugely absorbing and informative discussions spanning low dimensional semiconductor physics, classical music, politics, linguistics, religion and economics, Subal Sahni for helpful discussions regarding photodetection in Ge/Si diodes, Prab Bandaru for many hours spent training me in the fine art of electron beam lithography, and for being a ready reference for any materials questions, Josh Conway for his support during the job-hunt process, Sagi Mathai and Saif Islam for helpful RF photonics discussions, Wibool Piyawattanametha for his perennial exuberance, and for lending me signal sources in a crunch, Tejaswi Indukuri for doing thermal oxidation runs on some of my silicon wafers, and Ivair Gontijo for his undying efforts to introduce the concept of a social outing to a bunch of lab-locked engineers. I would also like to thank Rutger Vrijen, George Witzgall and Thomas Jung for assistance rendered during my first couple of years at UCLA.

The devices discussed in this dissertation were fabricated in the UCLA Nanoelectronics Research Facility (NRF). This was facilitated in no small part by the very excellent staff there. I would like to make a special mention of Steve Franz, Hoc Ngo and Tom Lee. Hoc, in particular, was extremely industrious in getting broken equipment up and running as soon as possible, and was always close at hand to help with stuck wafers, malfunctioning pumps, temperamental gages, leaky valves, jammed crucibles and fussy electron guns.

Graduate school occasionally involved a surprising amount of paperwork, and I would never have survived it without help from the administrative staff at the Electrical Engineering Department. In this regard, I am especially thankful to Jaymie Otayde-Mateo, Cheryle Childress, Janie Lee-Docter, Leticia Dominguez, Jamie Jung, Ilhee Choi and Deeona Columbia for making life much easier than it otherwise might have been.

My family has been extremely supportive through my stay in grad school. A huge thank you to my sister Sudha, brother-in-law Prasad, and niece Priya, for tolerating my frequent presence in their home in the San Francisco bay area. I would often go up there for rest, good conversation, and much needed nourishment. I also thank my aunts, Krupa Rangarajan, Kshama Sreenath and Prabha Iyengar for their love and encouragement. Thanks also to Lakshmi and Eric Eknath, and to Ranjini and Sampath Iyengar for welcoming me in their homes, and for many packed goodies when I first came to Los Angeles.

My friends from college who moved to the Los Angeles area were a very great source of support and friendship. My thanks to Deepak Rao, who inspired me to study photonics during a late night conversation we had over coffee when we were undergrads. I've known Deepak for nearly ten years, and he has never ceased to inspire me with his combination of smartness and tenacity. I also thank Ramesh Chokkalingam, who never allowed me to feel homesick. Using his phenomenal culinary skills he would dish up a feast for every Indian festival. Thanks also to my long time friend, Shilpa Sambashivan, and her boyfriend Saurabh Kumar, for being great company over the weekends, and for being part of our four member hiking team. Our hikes in the Southern California area are the stuff of legend.

Finally, a word about the coolest, cutest girl in the observable universe….. my girlfriend, Pavitra, whom I am also married to by a fortuitous coincidence. She coaxed, encouraged, tolerated, understood, and endured every up and down of graduate school. She makes it all worth it.

I am grateful to the Sumitomo Osaka Cement Co. for supplying the dual-electrode Mach-Zehnder modulators used in this project. Thanks also to the engineers at Micron Optics Inc. for their efforts in optimizing the reflection mode suppression of the fiber Fabry Perot devices used for the experiments in this dissertation.

The work in this dissertation was funded in part by the Defense Advanced Research Projects Agency (DARPA) Next Generation Internet (NGI) program, the Office of Naval Research (ONR) RF Photonics Multi University Research Initiative (MURI), the DARPA Chip Scale-WDM project, the California Nano Systems Institute (CNSI) and the Center for Nanoscience Innovation for Defense (CNID).

VITA

January 17, 1977	Born, Bangalore, India
1996	Intern Software Technology Park, Bangalore, India
1998	Design Engineer Intern Signal Processing IC Group Siemens Components Pte. Ltd. (now Infineon), Singapore
1998	B. Eng. (Honors) Electrical & Electronics Engineering Birla Institute of Technology & Science, Pilani, India
1998-1999	UC Graduate Fellow
1999-2004	Graduate Student Researcher Optoelectronics Lab Electrical Engineering Department University of California, Los Angeles
2000	Teaching Assistant Electrical Engineering Department University of California, Los Angeles
2001-2002	UCLA Graduate Division Fellowship
2001	M.Sc. Electrical Engineering University of California, Los Angeles

PUBLICATIONS AND PRESENTATIONS

1. A. Narasimha and E. Yablonovitch, “Low loss optical fiber-chip interface for Silicon-on-Insulator (SOI) nanophotonic integrated circuits”, (invited paper), Intl. Symposium on Integrated Optoelectronics, Meeting of the Electrochemical Society, Honolulu HI, October 2004.
2. A. Narasimha and E. Yablonovitch, “Efficient optical coupling into single mode Silicon-on-Insulator thin films using a planar grating coupler embedded in a high index contrast dielectric stack”, paper CWA46, IEEE/OSA Conference on Lasers & Electro Optics (CLEO), Baltimore MD, June 2003.
3. A. Narasimha and E. Yablonovitch, “Code-selective frequency shifting by RF photonic mixing in a dual-electrode Mach-Zehnder modulator”, Electronics Letters, vol. 39, no. 7, 3 April 2003, pp. 619-620.
4. A. Narasimha**,** X.J. Meng, C.F. Lam, M.C. Wu and E. Yablonovitch, “Maximizing spectral utilization in WDM systems by microwave domain filtering of tandem single sidebands.”, IEEE Transactions on Microwave Theory & Techniques, vol. 49, no. 10, Oct 2001, pp. 2042-7.
5. A. Narasimha, X.J. Meng, M.C. Wu and E. Yablonovitch, “A tandem single sideband modulation scheme for doubling the spectral efficiency of analog fiber links”, Electronics Letters, vol. 36, no. 13, 22 June 2000, pp. 1135-6.
6. A. Narasimha and E. Yablonovitch, "Code-selective RF photonic mixing for use in optical CDMA demultiplexers", paper TuO5, IEEE LEOS Annual Meeting Conference Proceedings, San Diego CA, November 2001.

7. A. Narasimha, X..J. Meng, M.C. Wu and E. Yablonovitch, "Full optical spectral utilization by microwave domain filtering of tandem single sidebands", paper WDD44, Technical Digest of the Optical Fiber Communication Conference (OFC), Anaheim CA, March 2001.
8. A. Narasimha, X.J. Meng, M.C. Wu and E. Yablonovitch, "A tandem single sideband fiber optic scheme using a dual-electrode Mach-Zehnder modulator", paper CMR6, Technical Digest, IEEE Conference on Lasers & Electro Optics (CLEO), San Francisco CA, May 2000.
9. A. Narasimha and E. Yablonovitch, “Fiber-chip interface for Silicon-on-Insulator (SOI) nanophotonic integrated circuits”, Center for Nanoscience Innovation for Defence (CNID), Riverside CA, August 2003.
10. A. Narasimha and E. Yablonovitch, “High efficiency grating couplers for sub-micrometric Silicon-on-Insulator (SOI) waveguides”, UCLA Electrical Engineering Department Annual Research Review, Westwood CA, October 2002.
11. A. Narasimha, X.J. Meng, M.C. Wu and E. Yablonovitch, "Carrying RF signals over tandem single sideband optical links", Office of Naval Research RF Photonics MURI, Boulder CO, October 2000.
12. A. Narasimha, X.J. Meng, C.F. Lam, M.C. Wu and E. Yablonovitch, "Tandem single sideband optical communications", DARPA Next Generation Internet Principal Investigator Meeting, McLean VA, October 2000.
13. A. Narasimha, X.J. Meng, M.C. Wu and E. Yablonovitch, "High spectral efficiency optical communications", DARPA Heterogeneous Optoelectronics Technology Center (HOTC), Santa Barbara CA, July 2000.

ABSTRACT OF THE DISSERTATION

Low dispersion, high spectral efficiency RF photonic transmission systems and low loss grating couplers for Silicon-on-Insulator nanophotonic integrated circuits.

by

Adithyaram Narasimha

Doctor of Philosophy in Electrical Engineering
University of California, Los Angeles, 2004
Professor Eli Yablonovitch, Chair

There has been tremendous interest in applying the sophistication present in electrical communication to the field of fiber optic communications. This includes the area of coherent detection, which has eluded optics due to the absence of stable and noise free optical local oscillators. The first half of this dissertation discusses the design and experimental demonstration of high spectral efficiency, low dispersion transmission systems that use the strengths of electrical communication to compensate for areas in which optics is lacking. We propose a system that achieves high spectral efficiency by using microwave filtering to compensate for the slow roll-off in optical filters. We also demonstrate coherent detection without an optical local oscillator, by using microwave photonic mixing rather than all-optical mixing.

The receivers described here use high-performance modulators to perform the function of microwave photonic mixing. Adding such sophistication to optical

communications circuits is currently impeded by the cost and complexity of the different optical components that currently exist in diverse material systems. In order to truly exploit the potential of optical functionalities across a broad range of applications, it is essential to realize ultra-compact multi-functional optics on a single platform. Silicon-on-Insulator (SOI) is a material system that shows great promise in this regard. Silicon is ubiquitous in the electronics industry, and processing techniques are well established. The superficial silicon of SOI presents us with a high index contrast layer in which miniaturized optics and electronics could coexist in a high density optoelectronic IC. This could lead to a hybrid photonic/electronic circuit that would be compatible with CMOS technology.

However, the high index contrast system comes with a penalty. The need for single mode optical waveguides in the silicon, requires a waveguiding layer that is 200-300 nm thick. This results in a huge mode mismatch with single mode fiber, precluding the use of simple end-fire coupling to interface the fiber with the nanophotonic chip.

The second half of this dissertation discusses the design, fabrication and characterization of a grating coupler that addresses this problem. A novel design is proposed to enhance coupling efficiency, and a proof-of-concept experiment is performed.

Chapter 1 Introduction

This dissertation is divided into two main sections. The first section deals with RF photonic and fiber wireless transmission systems for high spectral efficiency and low dispersion optical communications. The second section addresses the problem of designing and demonstrating a low insertion loss interface to couple light from single mode optical fiber into Silicon-on-Insulator (SOI) nanophotonic integrated circuits. This chapter describes the motivation and background for the first section of this dissertation contained in Chapters 1 through 5. Motivation for the second half of the dissertation is discussed briefly in this chapter, but is developed in much greater detail in Chapter 6.

1.1 Motivation

The first part of this dissertation is largely concerned with single sideband modulation and coherent detection. Single sideband modulation has been used in radio communication systems in an effort to improve their bandwidth requirements and hence their spectral efficiency [1]. Recently there has been considerable interest in applying these concepts to fiber optic communication systems [2-4]. Fiber optic single sideband systems offer the additional advantage of reducing the dispersion penalty associated with the long distance transmission of the signal [5].

The growth of Internet usage and the proliferation of numerous new network applications have revolutionized the field of optical communications. Every Hertz available in optical fibers is now valuable for carrying network traffic. The prevailing trend for capacity optical communications is dense WDM technology. However dense WDM systems were not very dense at the beginning of this project. 10 Gb/s channels were being carried over wavelengths spaced a 100 GHz apart. Present systems are no more than 2X better. Future DWDM systems are projected to carry 40 Gb/s channels on wavelengths spaced 50 GHz apart. Clearly the electrical bandwidth is increasing, while the optical guard-band is decreasing. The rapid increase in electrical circuit speed as well as the advent of Erbium doped fiber amplifiers (EDFA) has made most optical links dispersion limited rather than loss limited. The requirements for both high spectral efficiency as well as tolerance to dispersion as described above, have made optical single sideband transmission a very important technique.

Apart from the applications detailed above, there has been great interest in developing the millimeter wave frequency band for future wireless communications [6]. Low loss fiber links are a very attractive method for the efficient delivery of mm wave signals in wireless networks. The complexity of electronics in base stations is significantly reduced, by transmitting the signal as a millimeter wave directly over fiber. This eliminates the need for upconverting mixers and other frequency manipulations at base stations. A number of techniques for the generation, modulation and transport of these kinds of signals have already been discussed in the literature [7-15]. Optical single sideband transmission has emerged as the ideal way to carry mm waves over fiber without being prone to the chromatic dispersion penalties associated with such large radio frequency differences [5]. The transmission of multiple mm wave frequencies with different information over a single wavelength is a form of sub-carrier multiplexing (SCM) which has previously been exploited to increase the granularity of wavelength channels for applications such as video transmission [16]. A combination of SCM and

Optical single sideband could lead to increased granularity on a wavelength channel together with low dispersion.

Despite the obvious advantages of single sideband communications, they have some drawbacks. We will show in Chapter 2, that a pure single sideband signal is still unable to achieve complete spectral utilization in a WDM system, the spectral efficiency being limited by the quality of the optical filters used. Also, a single sideband signal is still prone to certain chromatic dispersion induced penalties that we shall talk about in Chapter 5.

This project aims at finding solutions to these problems, by proposing a modification of the single sideband system in which both sidebands are transmitted with different data. In addition, we design and demonstrate a receiver that exploits the sharpness of microwave filters to avoid depending on the quality of optical filters, in order to achieve complete spectral utilization in a WDM system. The receiver uses a dual-electrode Mach-Zehnder modulator to achieve coherent detection without the use of an optical local oscillator. This project also draws upon the techniques proposed to demonstrate the implementation of certain radio functionalities in the optical domain: techniques that could be very valuable to the transport and manipulation of RF signals over photonic links. Throughout the course of this work, both applications viz. fiber-wireless as well as high capacity WDM are kept in mind.

The second half of this dissertation discusses the design and experimental demonstration of low insertion loss grating couplers for SOI nanophotonic integrated circuits. SOI is attracting attention as a platform for the integration of both electronic and optical functions on a single substrate. Silicon is the material of choice of the electronics industry, and as such, processing techniques are well established and are widely used. The superficial silicon of SOI presents us with a layer in which miniaturized optics and electronics could conceivably coexist in a high density optoelectronic IC. The vision is that of a hybrid nanophotonic /electronic circuit that would be completely compatible with CMOS fabrication technology.

Despite the advantages in integration, the high index contrast system comes with a penalty. As we will show in Chapter 7, the need for single mode optical waveguides in the SOI nanophotonic ICs, requires that the waveguiding layer be approximately 200 nm thick. This results in a huge mode mismatch with single mode fiber, the core of which is roughly 50 X larger. This precludes the use of simple end-fire coupling to interface the optical fiber of the outside world with the nanophotonic circuit.

The project aims at finding a solution to this problem, by discussing the design of a low insertion loss grating coupler. The approach towards the design is more intuitive than rigorous, and the tone of the discussion is directed towards gaining a thorough physical understanding of grating coupler action, in order to yield a new coupler design, rather than towards developing numerical models for the quantitative assessment of efficiencies or other grating parameters. We also fabricate and experimentally demonstrate a low insertion loss grating coupler.

1.2 The single sideband technique

In this section, we will review some of the basic concepts of modulation and single sideband modulation from electrical communications. These concepts will form the basis for the design of optical single sideband and tandem single sideband transmitters. The simplest communication systems use amplitude modulation (AM). In an AM signal the transmitted signal is used to modulate the amplitude of a carrier frequency. The transmitted information is carried in the form of sidebands which appear on either side of the carrier during the modulation process (Fig 1.1). A simple AM receiver simply mixes the transmitted carrier with the sidebands to give the demodulated signal. No local oscillator is required at the receiver.

Even though both sidebands were used in the above case, it can easily be shown that the baseband signal can be recovered in a similar manner even if only one sideband is available [1]. There is an obvious advantage in doing so, since spectral space is used more economically. In principle twice the amount of information can be transmitted in the same bandwidth. However, such a signal cannot be recovered by simple envelope detection since there is no amplitude variation at the baseband frequency to which an envelope detector can respond.

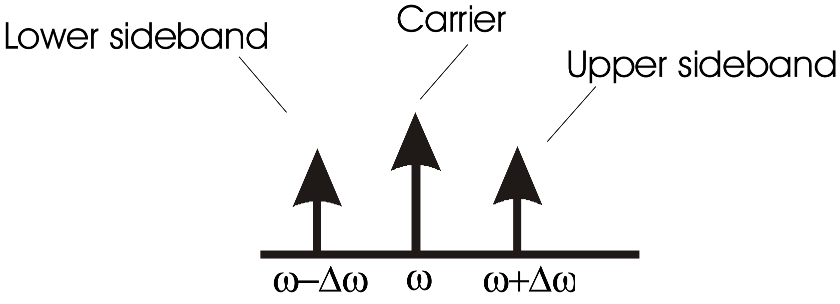

Figure 1.1 Amplitude modulation produces an upper and lower sideband on either side of the carrier frequency

Single sideband transmission can be achieved by simply filtering out one of the sidebands as shown in Fig. 1.2 by a more sophisticated modulation scheme as shown in Fig. 1.3 [1].

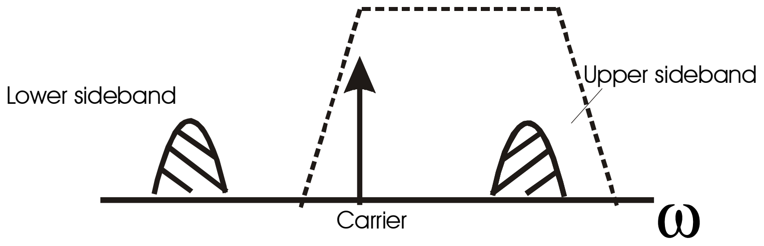

Figure 1.2 A primitive way of achieving single sideband transmission is to filter out one of the sidebands

In this modulation scheme phase quadratures of the carrier frequency and the baseband signal are used to obtain cancellation of one of the sidebands. The optical single sideband modulators we will talk about in this project, are based on a similar principle.

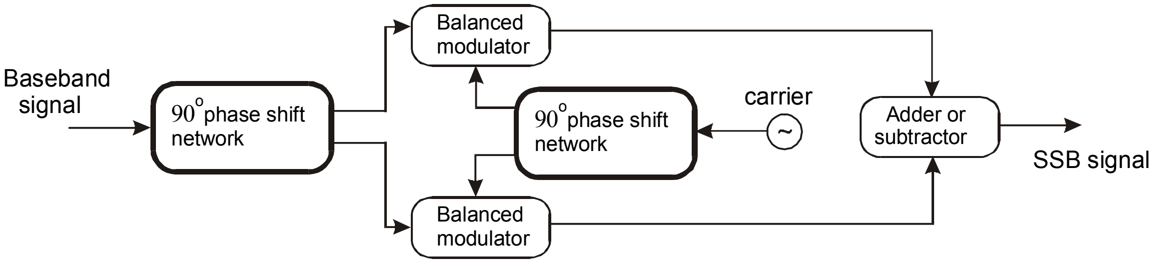

Figure 1.3 A method of generating electrical single sideband signals using balanced modulators and phase shifters. The choice of addition or subtraction determines whether the upper sideband or the lower sideband is chosen.

Baseband recovery is achieved in a single sideband communications channel by heterodyning the received signal with a local carrier signal that is coherent with the carrier used at the transmitting end to generate the single sideband (Fig 1.4). It is important that the coherence be maintained to a high order of precision in order to ensure faithful recovery of the transmitted signal. Highly stable coherent local oscillators are difficult to achieve in optical communications.

On the face of it, single sideband communication is quite complicated requiring the use of very stable local oscillators. However in optical single sideband communication, the transmitted carrier is used as a local oscillator, thus making it simpler than supplying a phase matched, frequency matched, polarization aligned oscillator at the receiver.

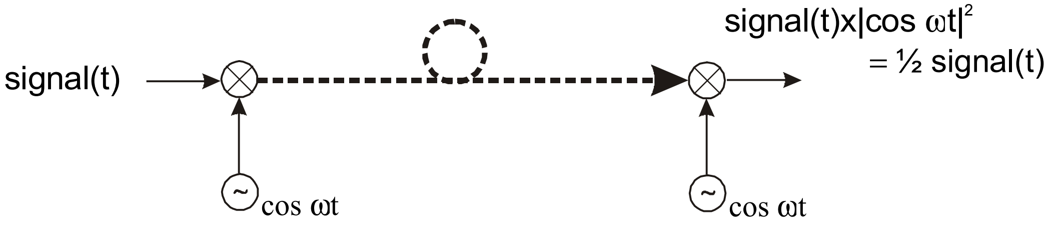

Figure 1.4 A coherent communication system in which the signal is recovered through the use of a phase synchronized local oscillator at the receiver.

1.3 Dissertation Organization

In this chapter, we stated the objective of the project, and gave a very brief introduction to electrical single sideband systems. Chapter 2 will deal with a general review of optical single sideband systems and their ability to decrease the dispersion penalty present in the long distance communication of the signal. We will show how the spectral efficiency of a single sideband system is limited by the quality of optical filters available, and show how this problem can be solved through the use of a tandem single sideband system: a system in which both sidebands of the same optical carrier are transmitted with different data on each of them. Chapter 3 will deal with an experimental demonstration of a tandem single sideband transmitter constructed using off-the-shelf components, as well as the experimental performance evaluation of such a transmitter in the presence of imperfections in those components. In Chapter 4, we will describe a new type of spectrally efficient receiver that can receive tandem single sideband signals through a heterodyning process that does not require the use of an optical local oscillator. Chapter 5 draws heavily on our transmitter and receiver designs from Chapter 3 and 4, to describe experiments that demonstrate radio operations in the photonic domain together with the transport of an RF signal. We demonstrate a technique for active code-selective direct sequence demultiplexing which has the potential to reduce the problems of cumulative shot noise and speckle in optical CDMA systems.

Chapter 6 introduces the second half of the dissertation by developing the motivation for integrated photonics and describing the SOI platform for the integration of both electronic and optical functions on a single IC. It also introduces the fiber-waveguide coupling problem associated with the high index contrast material system, and outlines the broad approach that we will use to solve it. Chapter 7 deals with the theory of grating couplers from a physical standpoint. The aim is to gain a thorough physical understanding of the sources of inefficiency in a grating coupler in order to come up with a new design to reduce insertion loss. We will show how the addition of a high index contrast dielectric stack above the coupler can serve to enhance coupling efficiency by creating desirable interference patterns within the coupler structure. The chapter also reviews prior work in the area of efficient grating coupler design. Chapter 8 describes the CMOS compatible fabrication of waveguide grating couplers for SOI nanophotonic integrated circuits, and Chapter 9 describes the design and implementation of an optical test bed to characterize the couplers. An experiment is performed to demonstrate reduced insertion loss from a novel grating design. Chapter 10 concludes this dissertation.

Chapter 2 Optical Single Sideband Modulation

2.1 Introduction

In the recent past, there has been a huge amount of interest in optical single sideband (OSSB) systems as a way to increase the spectral efficiency of optical communication systems while decreasing the dispersion penalty associated with the long distance transmission of the signal. Approaches involving simple filtering of the sideband have been proposed [17], but this project deals with an approach implemented using a dual-electrode Mach-Zehnder modulator [2] that very closely mimics the electrical single sideband modulator described in Chapter 1, in terms of functionality.

2.2 Optical Single sideband modulation using a dual-electrode Mach-Zehnder modulator.

Smith, Novak and Ahmed have proposed an optical single sideband modulator based on a dual-electrode Mach-Zehnder modulator [2]. In this section, we will describe an experimental setup similar to theirs and reproduce their mathematical formulation for the single sideband modulation process [5]. This is helpful in understanding how the single sideband signal is created, and what are the parameters affecting the performance of such a modulator. These ideas will carry across to tandem single sideband modulation as well.

The setup is shown in Fig. 2.1. Light from a laser diode at 1550 nm is coupled into the dual-electrode Mach-Zehnder modulator through a polarization controller which is necessary since the modulator works only in the TM mode. The modulator is biased at quadrature ensuring that a 90 degree optical phase difference exists between the two arms of the modulator.

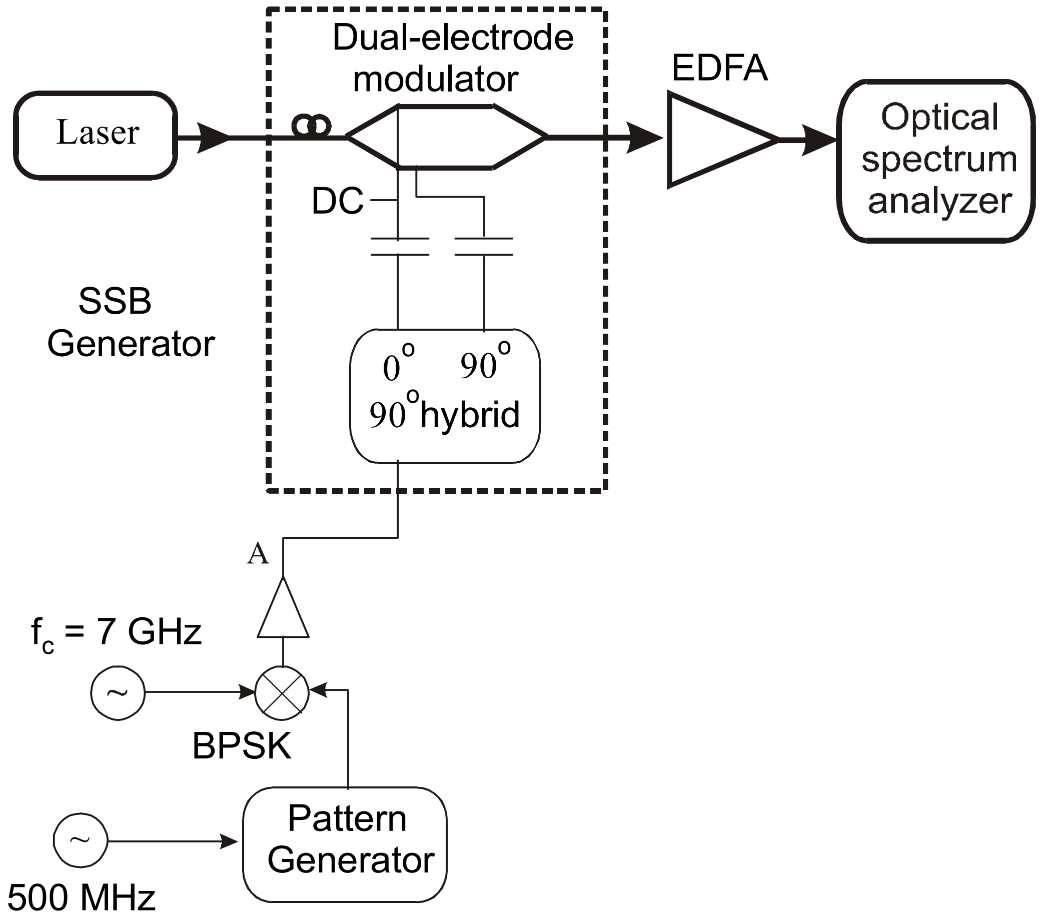

Figure 2.1 Block diagram of an optical single sideband modulator implemented using a dual-electrode Mach-Zehnder modulator.

An externally triggered pattern generator with 2^{23} –1 pseudo random bit sequences (PRBS) provided the baseband signal. The data was placed on an RF sub-carrier of 17 GHz using Binary Phase Shift Keying (BPSK). The modulated signal was connected to the input of the 90^0 hybrid coupler as shown in the figure. The outputs of the 90^0 hybrid coupler are used to drive the DE-MZM through bias-Ts. The signal that emerges from the DE-MZM is an optical single sideband signal consisting of an optical carrier at f_{oc} GHz and a lower sideband (LSB) at (f_{oc}-f_l) GHz. The upper sideband (USB) at (f_{oc}+f_l) GHz is suppressed as indicated in Fig. 2.2.

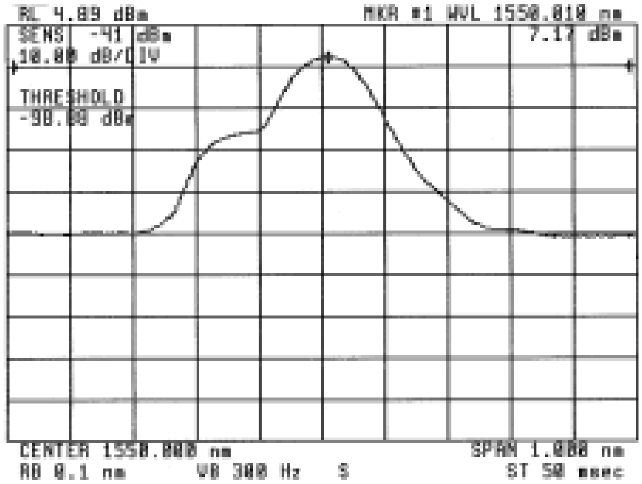

Figure 2.2 Optical spectra at output of optical single sideband modulator. The lower sideband is visible while the upper sideband is suppressed.

2.3 Mathematical Formulation of Optical Single Sideband

Let us denote the independent time varying pseudo-random bit sequences by L(t). For convenience of notation we will assume the time dependence and refer to it just as L. This is a digital bit stream that may be modeled as two level signals that assume values of either +1 or –1. The BPSK modulation of a carrier of frequency ω can be represented as [18]:

$$2LA\sin\omega t \tag{2.1}$$

where the carrier is $2A\sin\omega t$.

When this signal is connected to an ideal 90 degree hybrid coupler, the outputs may then be represented as:

$$\begin{aligned}&\textit{Output 1: } LA\ \sin\ \omega t\\&\textit{Output 2: } LA\ \cos\ \omega t\end{aligned} \tag{2.2}$$

These two inputs are fed to electrodes A and B of the dual-electrode modulator. We represent the optical carrier of frequency Ω by:

$$\sqrt{2}E\exp[j\Omega t]$$

To describe the modulation of the light signal we use the theory of the dual-electrode Mach-Zehnder modulator [5]. The upper arm of the DE-MZM is biased at quadrature with zero bias applied to the lower arm. In the upper arm of the DE-MZM we have:

$$\mathrm{E}(t)_{upper} = E\exp[j(\Omega t + \gamma\pi + \alpha\cos\omega t)] \tag{2.3}$$

where $\gamma = V_{bias}/V\pi, \alpha = \pi\, LA/V\pi$

Expressing equation (3) as a product of two series with Bessel function coefficients and using $\gamma = ½$ for quadrature bias of the DE-MZM we get:

$$\begin{aligned}\mathrm{E}(t)_{upper} &= jE\exp[j\Omega t]\bullet\exp[j\alpha\cos\omega t]\\&= jE\exp[j\Omega t]\\&\times[J_0(\alpha) + jJ_1(\alpha)\exp(j\omega t) + jJ_1(\alpha)\exp(-j\omega t) + ...]\end{aligned}$$

$$
\begin{aligned}
&= E\exp[j\Omega t]\{jJ_0(\alpha)\}\\
&+ E\exp[j(\Omega-\omega)t]\{-J_1(\alpha)\}\\
&+ E\exp[j(\Omega+\omega)t]\{-J_1(\alpha)\}\\
&+ \textit{ higher order terms.}
\end{aligned} \tag{2.4}
$$

By a similar analysis, in the lower arm of the modulator using $\gamma = 0$, we have:

$$\mathrm{E}(t)_{lower} = E\exp[j(\Omega t + \alpha\sin\omega t)$$

$$
\begin{aligned}
&= E\exp[j\Omega t]\{J_0(\alpha)\}\\
&+ E\exp[j(\Omega-\omega)t]\{-J_1(\alpha)\}\\
&+ E\exp[j(\Omega+\omega)t]\{J_1(\alpha)\}\\
&+ \textit{ higher order terms.}
\end{aligned} \tag{2.5}
$$

At the output of the modulator we have:

$$\mathrm{E}(t)_{signal} = \mathrm{E}(t)_{upper} + \mathrm{E}(t)_{lower} \tag{2.6}$$

Using (4) and (5) in (6) we get:

$$
\begin{aligned}
&\mathrm{E}(t)_{signal}\\
&= E\exp[j\Omega t]\{J_0(\alpha)\}(1+j)\\
&+ E\exp[j(\Omega-\omega)t]\{-2J_1(\alpha)\}\\
&+ E\exp[j(\Omega+\omega)t]\{0\}\\
&+ \textit{ higher order terms.}
\end{aligned} \tag{2.7}
$$

For $\alpha<0.4$, the higher order Bessel functions vanish and $J_0(x)$ and $J_1(x)$ may be approximated by *1* and *x/2* respectively. Equation (2.7) becomes:

$$
\begin{aligned}
&\mathrm{E}(t)_{signal}\\
&= E\exp[j\Omega t](1+j)\\
&- \alpha E\exp[j(\Omega-\omega)t]
\end{aligned}
$$

The data has ended up in the lower sideband while the upper sideband has been canceled. The two phase shifts at the input and the output of the modulator cancel each other out and do not have to be factored into the calculation.

It is important to note, that in practical situations especially such as those we will be describing in this thesis, it is important to have a highly linearized modulator since the modulation depth may not be very small.

2.4 Dispersion performance of the optical single sideband signal

Fig. 1 in reference [5] shows the received RF power against distance for a double sideband RF signal. The chromatic dispersion in the fiber causes the two sidebands to swing periodically out of phase and then back in phase. When the two sidebands have a 180 degree phase difference between them, there is complete cancellation of the RF power and no signal is received. Transmitting a single sideband signal avoids this problem. Since the sideband is only one side of the optical carrier, the RF power received is almost constant with distance as seen in Fig. 5 of reference [5]. This is the most compelling advantage of optical single sideband systems.

2.5 The case for "tandem" single sideband.

Despite the fact that optical single sideband improves the spectral efficiency by utilizing only half the bandwidth, optical single sideband channels cannot be packed close together in a WDM spectrum owing to the poor roll-off of optical filters used to demultiplex the signal. Fig. 2.3a makes this clearer. Since the adjacent optical carrier from the next channel is right next to the channel being selected, it is impossible to completely suppress the neighboring optical carrier. This will result in significant interference in the recovered single sideband signal.

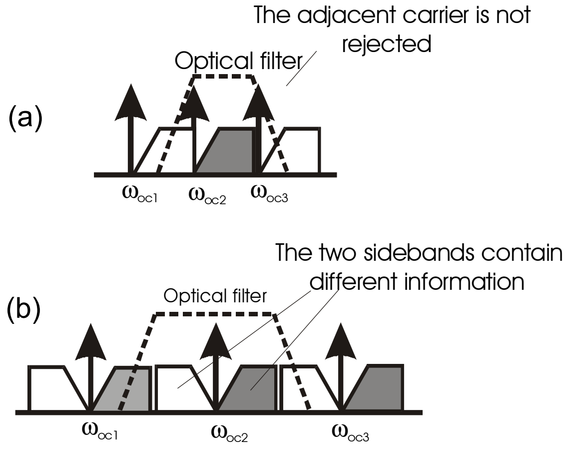

Figure 2.3a) Pure SSB WDM systems need guardbands to prevent adjacent carriers from interfering with the desired signal. b) Tandem single sideband signals enable carriers to be twice as far apart without wasting bandwidth. Optical channels may be separated by coarse optical filtering since the sidebands are finally separated by sharp filters in the electrical domain.

In a tandem single sideband signal both sidebands are transmitted with different data. This enables the optical carriers to be spaced twice as far apart, without a compromise in spectral efficiency. Fig. 2.3b illustrates this point. Such a transmitter will be demonstrated in Chapter 3. Since the optical carriers are spaced by two sidebands a regular coarse optical filter can be used to separate adjacent channels. The sidebands of the adjacent channels that are also accepted, constitute an out-of-band cross-talk that is easily rejected by sharp microwave filtering as will be seen in Chapter 4.

Chapter 3 Tandem Single Sideband Transmitter Demonstration and Performance Evaluation

In this chapter, we describe the design and experimentally demonstrate our *tandem* single sideband transmitter. This transmitter uses a combination of interconnected off-the-shelf microwave components with a dual-electrode Mach-Zehnder modulator to transmit different information in the two sidebands of the same optical carrier. For the purpose of demonstrating the modulator we use a coarse optical filtering approach to separate the sidebands. While the experiment described in this chapter, transmits different information in the two sidebands, unfortunately the spectral efficiency is limited by the quality of the optical filter used to separate the sidebands.

We will also show, that the performance of this system is dependent on the quality of the microwave components used and we will evaluate the susceptibility of the modulator performance to imperfections in the microwave components used.

3.1 Experimental Setup

The block diagram of the experimental setup used to demonstrate tandem single sideband transmission is shown in Fig. 3.1. The light source was an external cavity tunable laser diode (ECT-LD), tunable around 1550 nm. The light from the ECT-LD was coupled into a dual electrode Mach-Zehnder modulator (DE-MZM) through a polarization controller. An externally triggered pattern generator with 2^{23} -1 pseudo random bit sequences provided the two baseband signals. The data was modulated using Binary Phase Shift Keying (BPSK) onto a sub-carrier at a frequency f_c = 10 GHz. The power in each of the two arms A and B, was 17 dBm. The two signals were then fed to the two inputs of a 90 degree hybrid coupler. The outputs of the 90 degree hybrid were used to drive the DE-MZM through bias-Ts. The DE-MZM was biased at quadrature. An erbium-

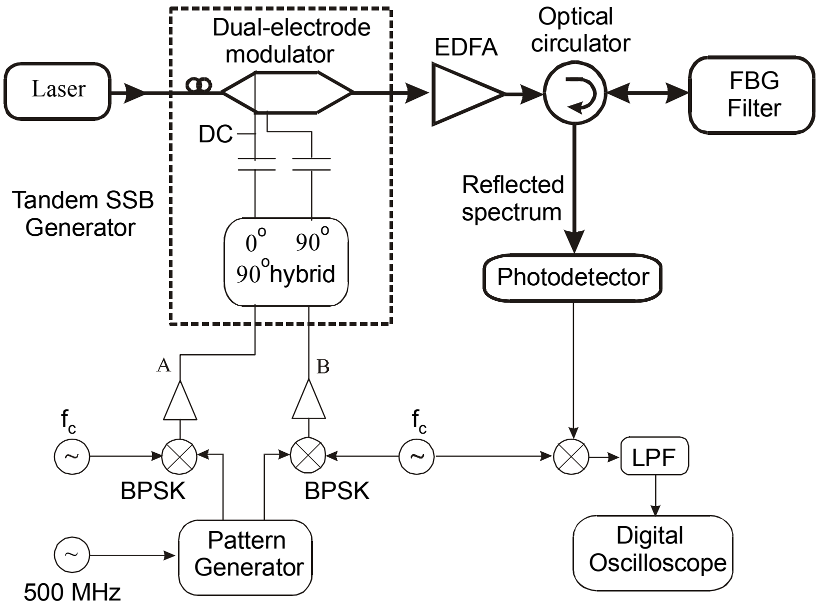

Fig 3.1 Block diagram of tandem single sideband transmitter. For verification of tandem single sideband transmission a coarse reflective fiber grating optical filter is used to distinguish between the sidebands.

doped fiber amplifier (EDFA) was used to boost the output optical power. At the receiver, both the upper and the lower sidebands were separated by a combination of an Optical Circulator (OC) and a reflective fiber grating (FBG Filter) with a Full Width Half Maximum of 20 GHz centered at around 193.7 THz (Fig. 2). The signal was detected by a photo-detector (HP Lightwave Converter 11982A) with a conversion gain of 300 V/W. No other electrical amplification was used. The output was connected to a low pass filter (LPF) followed by a digital oscilloscope (HP 54542C) to monitor eye diagrams.

The setup was used to transmit only one sideband while suppressing the other one by connecting a signal to only one of the two inputs of the 90 degree hybrid. Tandem single sideband operation was achieved by connecting different signals to each of the two inputs of the 90 degree hybrid.

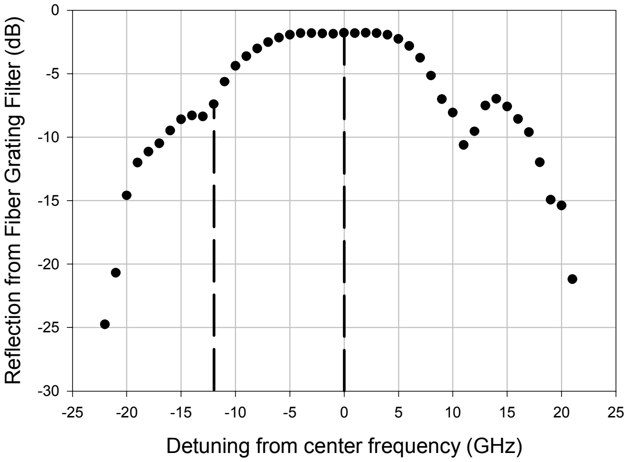

Fig. 3.2 Spectral response of reflective fiber grating filter. The dashed lines indicate the wavelengths at which the experiment was performed.

3.2 Experimental Results

Fig. 3.3 shows the sideband suppression obtained from the dual-electrode modulator. As a preliminary test, a pure RF frequency of 5 GHz. was connected to input B of the 90 degree hybrid, with no signal at input A. As can be seen in Fig. 3.3, the modulator suppressed the upper frequency sideband by more than 20 dB.

The actual experiment was performed at two different wavelengths of the laser source. In the first case the laser frequency was chosen to correspond with the center frequency of the fiber grating (0 GHz in Fig. 2). This ensured that both sidebands were almost equally reflected by the fiber grating filter. Fig 4(a) shows the received eye diagram for the case of a signal connected to input A of the 90 degree hybrid, with no signal at input B, thus placing the signal on the upper frequency sideband and suppressing the lower frequency sideband. Fig. 4(b) shows the eye diagram for the opposite case with a signal only at input B of the 90 degree hybrid, thus placing the signal on the lower frequency sideband while suppressing the upper one. Fig. 3.4(a) and 3.4(b) show that the upper and lower sidebands were almost equally reflected by the fiber grating, and that the transmission was successful when they were transmitted individually. Fig 3.4(c) shows the received eye diagram for the case when different signals were connected to both inputs A and B of the 90 degree hybrid coupler, thus

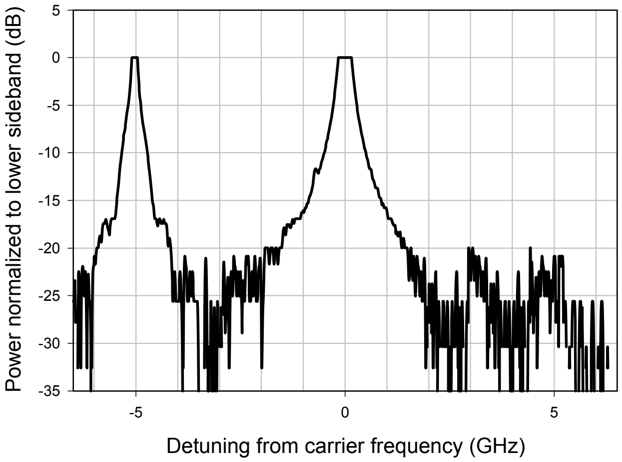

Fig. 3.3 Sideband rejection obtained from Dual-Electrode Mach-Zehnder modulator. The upper sideband, 5 GHz above the carrier frequency was suppressed by more than 20 dB relative to the lower sideband.

transmitting the two optical sidebands in tandem. The severely degraded eye diagram indicates that there were different signals on each of the sidebands.

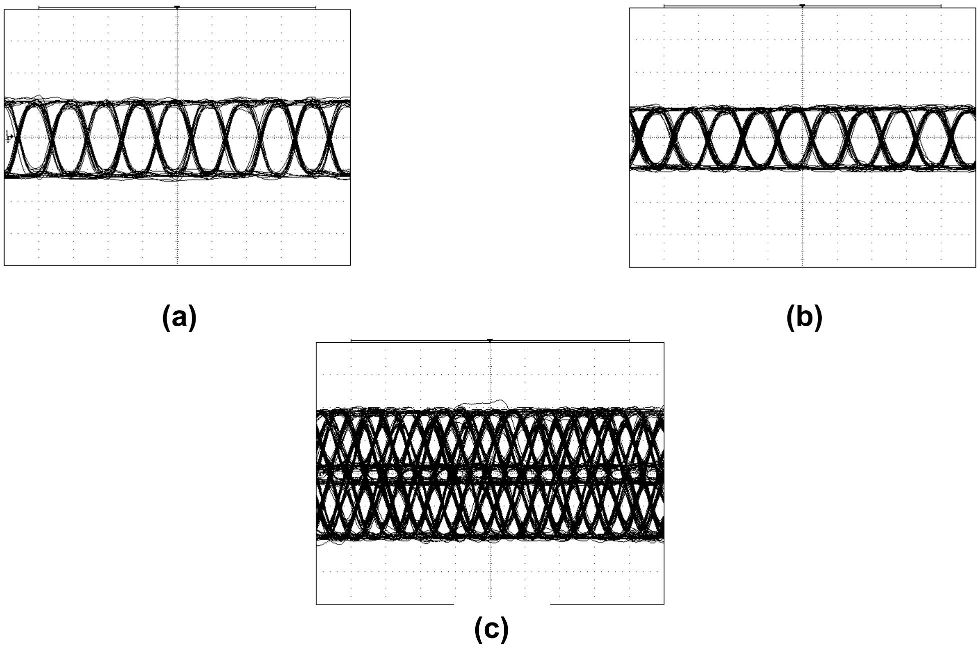
(a)

(b)

(c)

Fig. 3.4 Received 500 Mb/s eye diagrams when both sidebands were reflected into photodetector for the case of a) only upper sideband transmitted, b) only lower sideband transmitted and c) both sidebands transmitted in tandem. Since both sidebands had different pseudo random data, the eye diagram in c) is severely interfered.

Fig. 3.5 shows BER data corresponding to the situation in Fig. 3.4(a) and 3.4(c). The second BER curve indicates the strong interference also confirming that there is different data on each of the two sidebands.

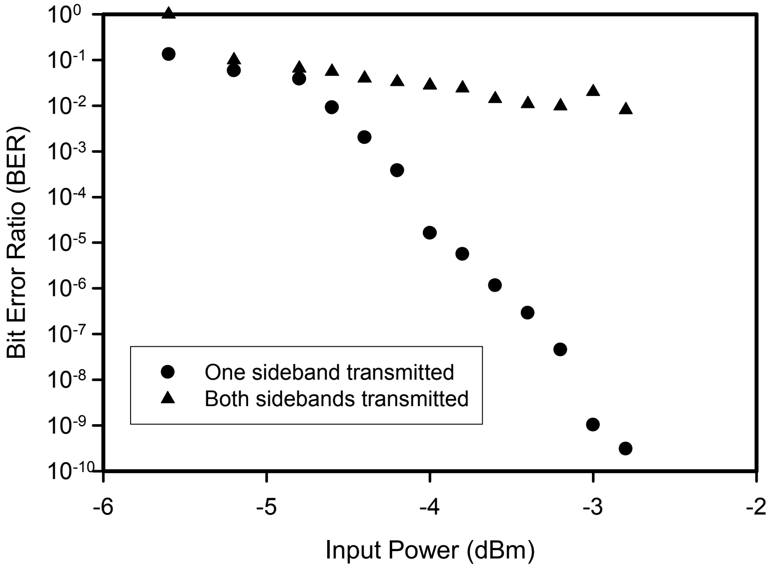

Fig. 3.5 BER curves for the case when both sidebands were reflected by the fiber grating into the photodetector. Since both sidebands contained different pseudo random data, a very high BER floor was seen when both sidebands were transmitted.

The experiment was repeated with the laser frequency downshifted by 12 GHz as shown in Fig. 3.2. Fig. 3.6(a) and 3.6(b) show the cases when the sidebands were transmitted individually. The fiber grating reflected the higher frequency (lower wavelength) sideband, while almost completely rejecting the lower frequency (higher wavelength) sideband as can be seen from Fig. 3.6(a) and 3.6(b). The rejection of the lower frequency sideband resulted in an excellent eye diagram in Fig. 3.6(c) even when both sidebands were transmitted in tandem.

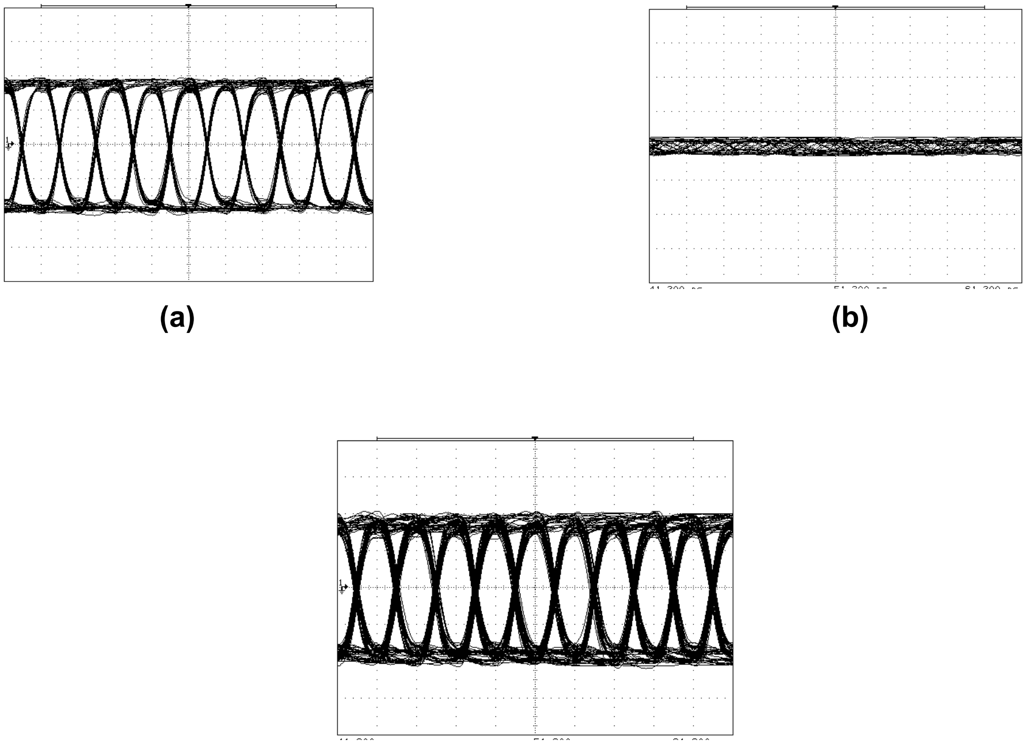

(a)

(b)

(c)

Fig. 3.6 Received 500 Mb/s eye diagrams when only the upper sideband was reflected into the photodetector for the case of a) only upper sideband transmitted, b) only lower sideband transmitted and c) both sidebands transmitted in tandem. Since the lower sideband was almost completely rejected by the optical filter, case c) shows an excellent eye diagram.

Fig. 3.7 shows BER data for the situations in Figs. 3.6(a) and 3.6(c). The rejection of the lower sideband by the fiber grating filter resulted in an obtainable BER of 1E-9 when both sidebands were transmitted in tandem.

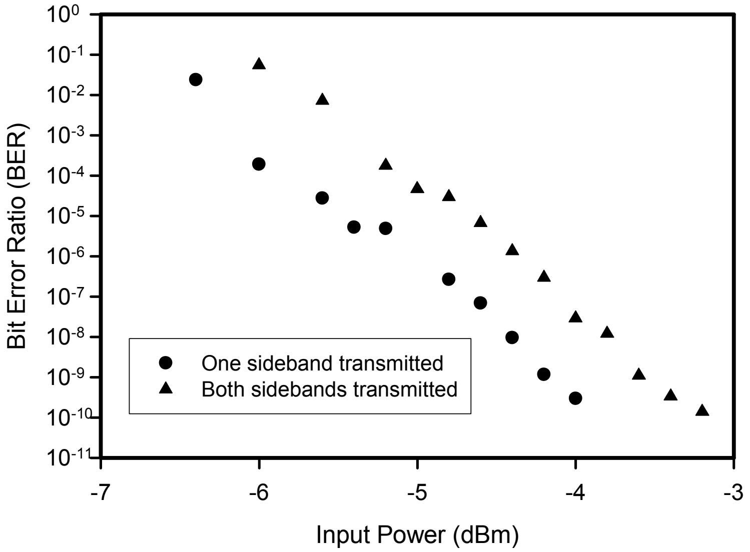

Fig. 3.7 BER curves for the case when only the upper sideband was reflected by the Fiber Grating into the photodetector. Since the lower sideband was almost completely rejected, a good BER curve was obtained even when both sidebands were transmitted.

3.3 Performance Evaluation of Tandem single sideband modulator.

The mathematical analysis in Chapter 2, assumed absolutely perfect microwave components and hence perfect balance between the two microwave arms connected to the two electrodes of the dual-electrode modulator as well as perfect balance between the two arms of the modulator itself. However, in practical systems these paths are not necessarily completely balanced. Several factors contribute to this: the unbalanced output powers from the two outputs of the 90 degree hybrid resulting in unequal drive voltages on the modulator electrodes, deviations in the bias of the modulator from quadrature as well as phase errors in the 90 degree hybrids. The net effect of these imperfections is to cause inter-sideband cross-talk.

To evaluate the performance of the proposed transmitter using non-ideal components, we used a single tone RF frequency of 5 GHz connected to input B of the 90 degree hybrid (Fig. 3.1). This had the effect of suppressing the upper sideband as seen in Fig. 3.3. We define an *inter-sideband cross-talk ratio* as follows:

$$\textit{Inter-sideband cross-talk} = 10\log_{10}\frac{P_{upper}}{P_{lower}} \tag{3.1}$$

where P_{upper} and P_{lower} are the powers in the upper and lower sideband respectively.

A. RF Power Mismatch

The cancellation of cross-talk terms when we add equations (2.4) and (2.5) in Chapter 2, depends on the terms being of exactly equal amplitude. Any imbalance in the RF power between the two arms would result in different drive voltages at the two electrodes and hence imperfect cancellation of the cross-talk terms. The inter-sideband cross-talk caused by RF power mismatch between the two electrodes of the DE-MZM was measured by introducing an attenuator in arm A of Fig. 3.1 and varying the attenuation. Fig. 3.8 shows an experimental plot of inter-sideband cross-talk suppression as a function of RF power mismatch. An inter-sideband cross-talk of less than –20 dB is seen for a power mismatch of less than 3 dB. This tolerance allows for the adjustment of the electrode voltages, and hence the modulator chirp which is important in increasing the maximum transmission distance of the link [5].

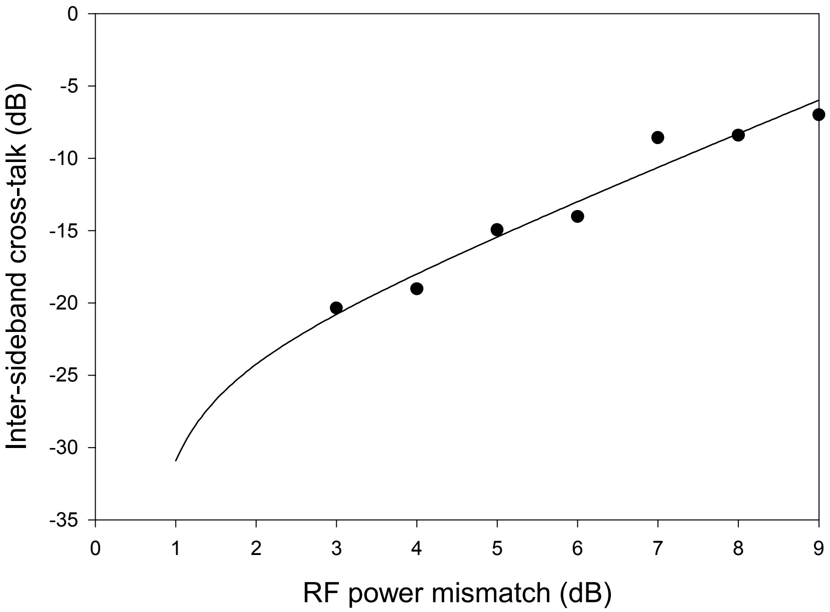

Fig. 3.8 Inter-sideband cross-talk as a function of RF power mismatch at the two electrode of the DE-MZM. The modulator suppresses cross-talk by more than 20 dB for a power mismatch of less than 3 dB. The plotted points are experimental data. The solid curve is a guide to the eye.

B. Deviations of Bias from the Quadrature Point

The dual-electrode modulator is biased at quadrature for tandem single sideband operation. Deviations from quadrature bias would result in imperfect cancellation of the inter-sideband cross-talk terms present in equation (4) and (5) in Chapter 2.

Fig. 3.9 shows an experimental plot of inter-sideband cross-talk against the normalized deviation of the modulator bias from the quadrature point. An inter-sideband cross-talk of better than 20 dB is seen for deviations from the quadrature point of less than 0.2 V_π

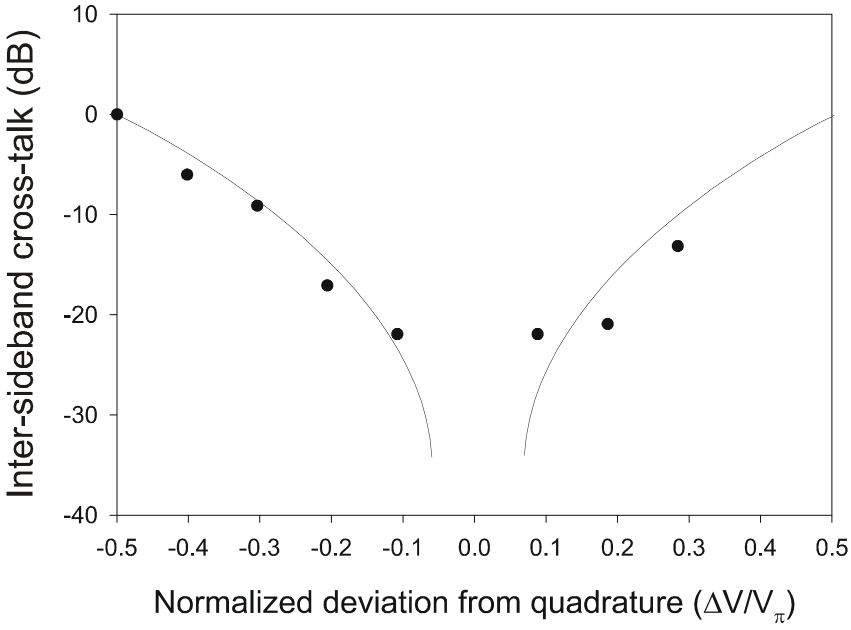

Fig. 3.9 Inter-sideband cross-talk as a function of the deviation of bias from the quadrature point, normalized to V□. The solid lines are to guide the eye.

C. Phase mismatch between the two arms

The analysis in Chapter 2 shows that cancellation of inter-sideband cross-talk terms requires a 90 degree phase difference between the two electrodes of the DE-MZM. The phase difference between the two electrodes of the DE-MZM was varied by introducing a microwave phase shifter in arm A. Fig. 3.10 shows an experimental plot of the inter-sideband cross-talk suppression as a function of the phase deviation from 90 degrees at the two outputs of the 90 degree hybrid.

A tolerance of roughly ± 30 degrees is observed, for more than 20 dB of sideband suppression which is in good agreement with theoretical predictions made from mathematical models of the dual-electrode modulator [19].

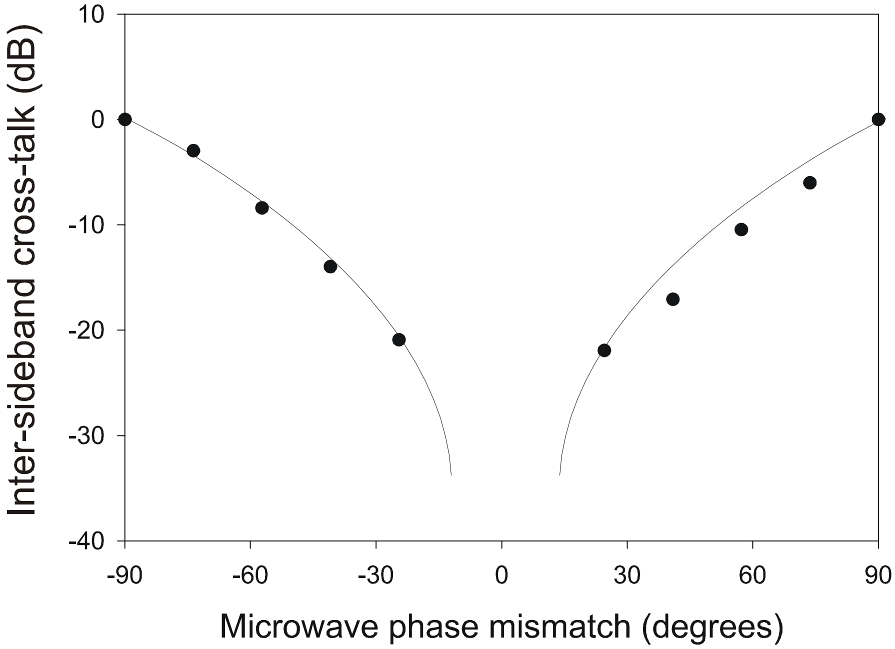

Fig. 3.10 Inter-sideband cross-talk as a function of phase mismatch between the two electrodes of the DE-MZM. The modulator suppresses cross-talk by more than 20 dB for a phase mismatch of ± 30 degrees. The dots are experimental data. The solid curves are a guide to the eye.

D. *Phase-Bias Compensation*

Fig. 3.11 shows the phase curves at three different values of bias. From the figure we see that maximum suppression can be obtained even at a phase difference of 30 degrees by varying the bias appropriately. This phase-bias relationship implies that minor variations in phase, can be compensated for by tuning the bias. This would however, also affect the chirp parameter and the maximum length of the link [4]. The best bias point has to be determined by optimizing the bias point for cross-talk suppression as well as for chirp.

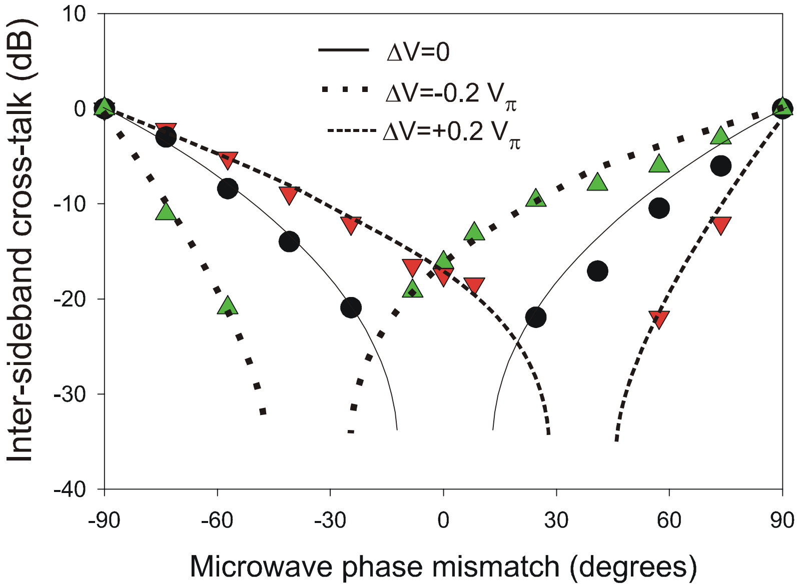

Fig. 3.11 Inter-sideband cross-talk as a function of microwave phase mismatch at three different modulator bias voltages. The dots are experimental data. The curves are to guide the eye.

3.4 Discussion and Conclusion

The observation that there was different information in each of the sidebands, indicates that the tandem single sideband transmission was successful. We have doubled the information capacity of a single wavelength by transmitting different data in each of the two sidebands of the same optical carrier. This enables increased capacity on an RF frequency in fiber-wireless networks. The scheme does not require increased modulator bandwidth since both sidebands of the optical carrier are used. The increased number of channels enhances the potential of SCM as a broadcast tool and is useful for wavelength routing schemes since it minimizes delay time while maximizing throughput, both of which are extremely desirable [20].

The performance of the tandem single sideband modulation scheme using imperfect components was experimentally evaluated. The results indicate that the technique is relatively robust with respect to imperfections in the components used, demonstrating a phase tolerance of close to ± 30 degrees and a tolerance in amplitude difference of a little under 3 dB for an inter-sideband cross-talk suppression of more than 20 dB. These experimental results are in agreement with theoretical predictions for the dual-electrode Mach-Zehnder modulator [19]. The results also suggest that a desired inter-sideband cross-talk suppression can be obtained by compensating an imperfection in the 90 degree hybrid coupler by tuning the modulator bias. This however, must be done carefully since changing the bias affects the chirp parameter and thus the transmission distance [5], and the nonlinear performance of the modulator. In any case, trying to pack more SCM channels on a single optical wavelength involves raising the modulation depth of the external modulator. This may be a problem due to modulator non-linearities. As such, in the long run if the true advantage of such a scheme is to be realized, highly linearized external modulators will be necessary.

Chapter 4 Tandem single sideband reception and heterodyne detection without the use of an optical local oscillator

Although tandem single sideband transmission makes for a doubling of the wavelength capacity on a single channel and a doubling of the capacity on a single sub-carrier frequency, the spectral efficiency of the system described in the previous chapter is still severely limited by the slow roll-off of the optical filter used to distinguish between the sidebands. In order to achieve maximum spectral efficiency in the presence of poor optical filters, we recognize the need for heterodyne detection. Conventional heterodyne detection, however calls for an optical local oscillator and it's associated polarization tracking and phase noise complications.

Here we propose the reception of tandem single sideband signals using a receiver that achieves heterodyne detection without the need for an optical local oscillator. Sharp electrical filtering is used to differentiate between the two sidebands, thus ensuring that the spectral efficiency is not limited by the poor quality of optical filters.

4.1 Experimental Setup and Principle of Operation

As mentioned in Chapter 2, on account of chromatic dispersion present in optical fibers, no matter what the phase relationship between the signals at the transmitter, there is no telling what phase relationship they will have at the receiver. Complete flexibility with respect to the length of fiber traversed, requires a receiver scheme that has no dependence on the phase relationship between the two sidebands. A tandem single sideband signal that has propagated over an arbitrary length of fiber would have an arbitrary phase relationship between the sidebands, which would cause them to interfere in the microwave domain when they fall on a photodetector. Thus a more sophisticated receiver scheme is called for.

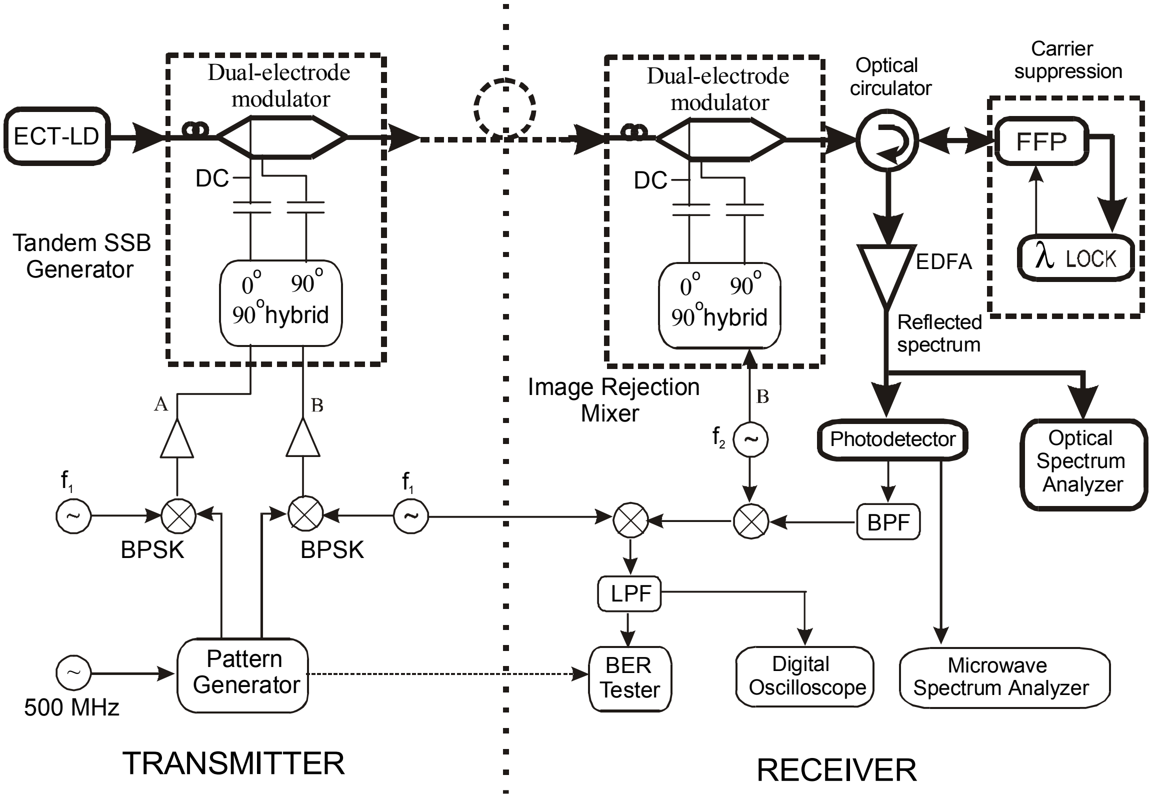

Fig. 4.1 Block diagram of setup to demonstrate highly spectrum efficient tandem single sideband receiver. The receiver demonstrates heterodyne detection without the use of an optical local oscillator.

A block diagram of the receiver design is shown in Fig. 4.1. The transmitter used to generate such signals is similar to the one described in Chapter 3. At the receiver, the signal is first coupled to a quadrature biased DE-MZM. Only input B of the 90^0 hybrid is used and the DE-MZM acts as an image rejection mixer up-shifting the incoming optical spectrum by f_2 GHz, while suppressing the downshifted version [5, Chapter 3]. (We used only a single optical wavelength, however in a WDM system we would need to separate the desired channel by a coarse optical filter like the one in Fig. 2.3 prior to upshifting).

The optical spectrum at this stage would then consist of the original spectrum centered at f_{oc} GHz [carrier at f_{oc} GHz, LSB at $(f_{oc}-f_1)$ GHz, USB at $(f_{oc}+f_1)$GHz] and a copy of it centered at $(f_{oc}+f_2)$ GHz, [carrier at $(f_{oc}+f_2)$ GHz, LSB at $(f_{oc}+f_2-f_1)$ GHz, USB at $(f_{oc}+f_2+f_1)$ GHz]. When this signal is incident on a photodetector, the optical carrier at f_{oc} GHz and the up-shifted version of the optical carrier at $(f_{oc}+f_2)$ GHz, both serve as local oscillators (LO) and beat with the original as well as with the up-shifted sidebands. Since there are two local oscillators and four sidebands (two original and two up-shifted) we would expect a total of 2x4=8 major terms from the heterodyning. The intermediate frequency (IF) at which each term would appear, would be exactly equal to the difference in frequency between the LO and the sideband signal causing it [21].

Table 4.1 shows a list of the eight heterodyne terms expected. For a TSSB signal, clearly the pairs of signals, (3) and (6), as well as (4) and (5) interfere with each other since the LSB and USB appear at the same IF. It is thus impossible to separate the two sidebands by this method if all eight terms are present. Eliminating terms (5) and (6) however, would enable us to recover the LSB and USB data from signals (3) and (4) respectively. Since terms (5) and (6) are obtained by the LSB and USB beating with the up-shifted carrier at $(f_{oc}+f_2)$ GHz, we may suppress them by suppressing this carrier. This does not affect signals (3) and (4) since they are obtained by the sidebands beating with the original optical carrier at f_{oc} GHz.

The up-shifted optical carrier at $(f_{oc}+f_2)$ GHz is suppressed by a Fiber Fabry-Perot (FFP) of free spectral range (FSR) = 10 GHz and a finesse of 200 operating in reflection

Mode as in [22]. A feedback loop keeps the FFP locked to the up-shifted carrier wavelength. This has the effect of suppressing terms (5)-(8), thus enabling the error-free recovery of the LSB and USB from terms (3) and (4) respectively. We may thus conclude that terms (3) and (4) are very desirable to us, while terms (5) and (6) are undesirable. We will use this notion in the remainder of our discussions. Note that we do not really care about terms (1), (2), (7) and (8) since they all appear at f_1 GHz and we have no way of distinguishing between them.

Term #	**Local Oscillator frequency**	**Sideband frequency**	**LSB/USB**	**IF**	**IF (f_1=2.5 GHz; f_2=9.5 GHz)**
1	f_{oc}	$f_{oc}-f_1$	LSB	f_1	2.5
2	f_{oc}	$f_{oc}+f_1$	USB	f_1	2.5
3	f_{oc}	$f_{oc}+f_2-f_1$	LSB	f_2-f_1	7.0
4	f_{oc}	$f_{oc}+f_2+f_1$	USB	f_2+f_1	12.0
5	$f_{oc}+f_2$	$f_{oc}-f_1$	LSB	f_2+f_1	12.0
6	$f_{oc}+f_2$	$f_{oc}+f_1$	USB	f_2-f_1	7.0
7	$f_{oc}+f_2$	$f_{oc}+f_2-f_1$	LSB	f_1	2.5
8	$f_{oc}+f_2$	$f_{oc}+f_2+f_1$	USB	f_1	2.5

Table 4.1 Heterodyning terms present after the photodetector when no Fiber Fabry Perot carrier suppression is used.

The signal reflected from the FFP was amplified by an Erbium Doper Fiber Amplifier (EDFA) and then detected by an Agilent Lightwave Converter 11982A with a conversion gain of 300 V/W. No other electrical amplification was used. The output was connected to a bandpass filter (BPF) centered at (f_1+f_2) GHz followed by two stages of microwave down-conversion to bring the signal back to baseband. The RF local oscillators used for down-conversion were exactly those used for up-conversion enabling exact phase and frequency matching. In practical systems where the transmitter and receiver are far apart, the RF carrier could be recovered through the use of a Costas loop [18]. The baseband signal was connected to a 500 MHz Low Pass Filter (LPF), followed by a digital oscilloscope (HP 54542C) to monitor eye diagrams, and an Error Performance Analyzer to measure Bit Error Ratio (BER).

4.2 Experimental Results and Discussion

In order to test our design we used f_{oc} =193.7 THz, f_1=2.5 GHz and f_2=9.5 GHz with different 500 Mb/s PRBS data on each sideband. The 90^0 hybrid couplers used in the experiment did not go all the way down to DC, thus restricting us to a minimum f_1 of 2.5 GHz. The bandpass nature of the hybrid coupler places a limitation on the ultimate achievable spectral efficiency, but this wastage of bandwidth is constant regardless of the number of subcarriers used, suggesting that the spectral efficiency can be improved by using more subcarriers.

We first tested the receiver with a pure LSB, obtained by connecting a signal to only input A at the transmitter. The optical spectrum entering the receiver consisted of an optical carrier at f_{oc}=193.7 THz, and an LSB at (f_{oc}-2.5) GHz. Fig. 4.2(a) shows that the DE-MZM at the receiver had the effect of creating an up-shifted copy of the spectrum centered at (f_{oc}+9.5) GHz. The optical spectrum was measured immediately after the EDFA both with and without the use of the FFP to suppress the carrier at (f_{oc}+f_2)=(f_{oc}+9.5) GHz.

Fig. 4.2(b) shows the predicted microwave spectra based on Table I, for the optical spectra shown in Fig. 4.2(a). Table I suggests that only the odd numbered terms would be present after the photodetector, while the even numbered terms would be absent since there is no USB. Thus any signal appearing at 12 GHz, would be solely due to term (5),

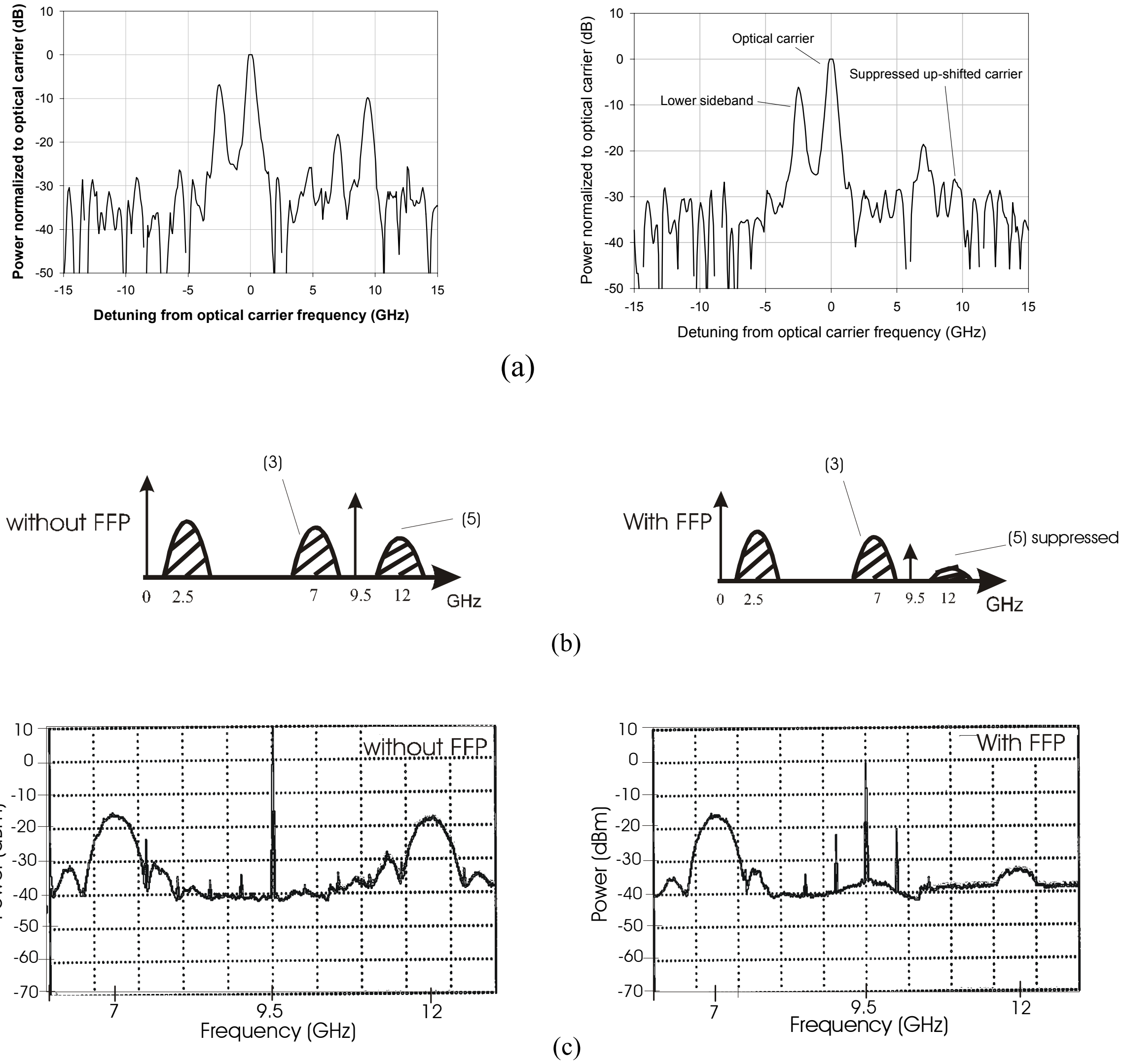

(a)

(b)

(c)

Fig. 4.2 Receiver performance in the case of purely LSB signals a) optical spectra after the DE-MZM both with and without the use of the FFP. Note the upshifted carrier suppression when the FFP is used. b) Projected microwave spectra as obtained from Table 4.1, after heterodyning in the photodetector and c) Measured microwave spectra showing the suppression of the unwanted term at 12 GHz when the FFP is used.

since term (4) would be absent. Tuning the FFP to the up-shifted carrier frequency at (f_{oc}+9.5) GHz, would eliminate term (5).

Fig. 4.2(c) shows measured microwave spectra for these two cases, confirming our predictions. The undesirable LSB term (5) at 12 GHz was suppressed by more than 15 dB.

In Fig. 4.3 we show the receiver operation for a TSSB signal. This time the incoming optical spectrum consisted of an optical carrier at f_{oc}=193.7 GHz, an LSB at (f_{oc}-2.5) GHz, and a USB with different data at (f_{oc}+2.5) GHz. Once again, Fig. 4.3(a) shows the original and up-shifted versions of the tandem single sideband optical spectrum, both without and with the use of the FFP.

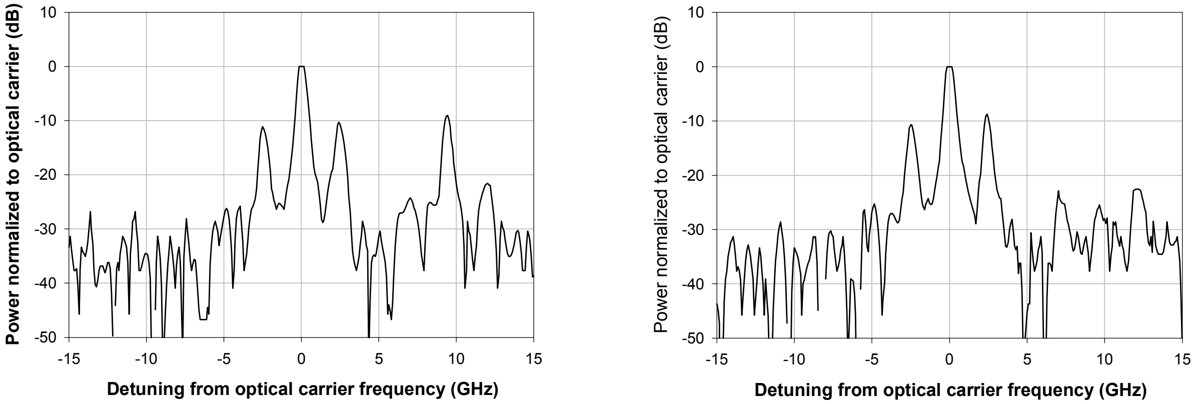

(a)

Figure 4.3 Receiver performance for tandem single sideband signals. a) Optical spectra after the DE-MZM in the receiver both with and without the use of the FFP.

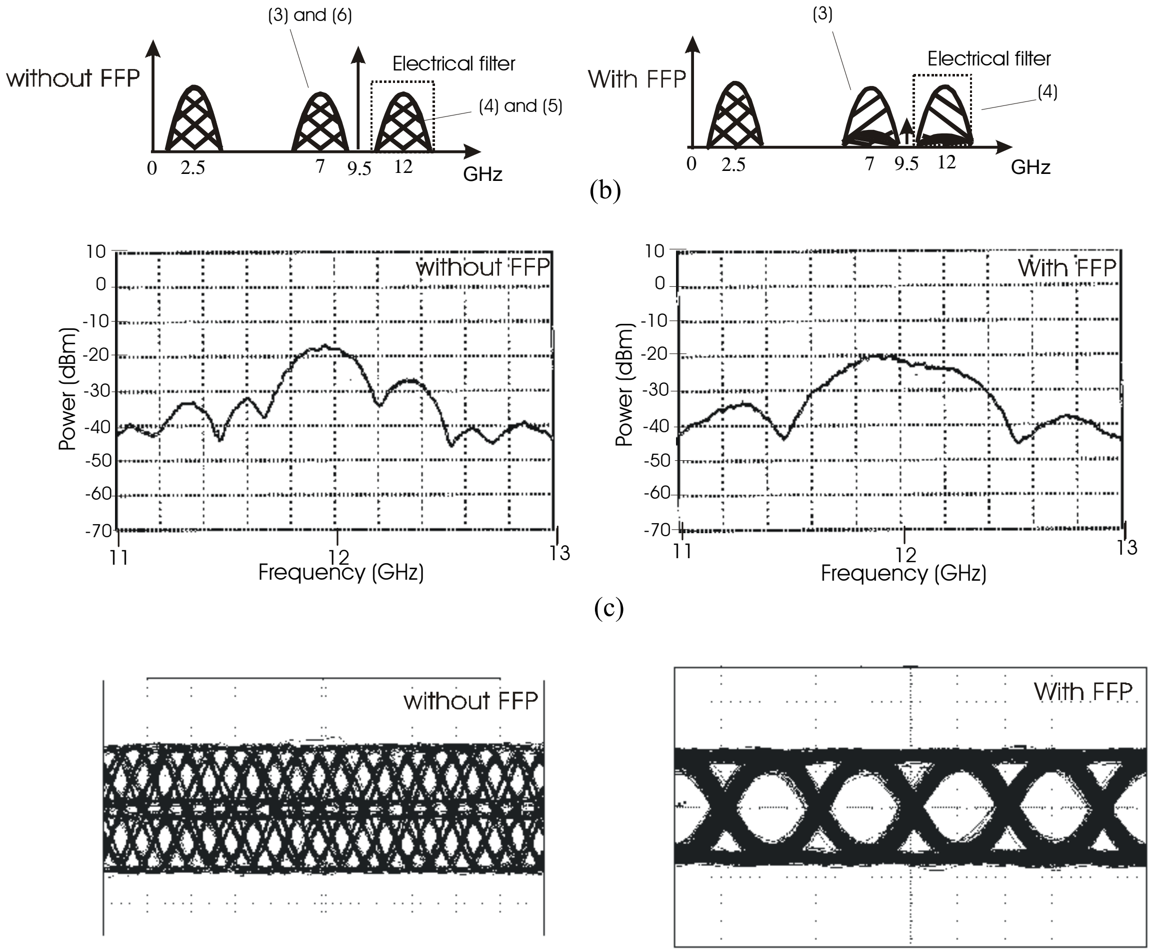

(b)

(c)

(d)

Fig. 4.3 Receiver performance for the case of tandem single sideband signals. b) Projected microwave spectra as obtained from Table I, after heterodyning in the photodetector, c) Measured microwave spectra and d) Eye diagrams of the signal at 12 GHz for both cases. A good eye diagram is obtained when the FFP is used.

Fig. 4.3(b) shows the expected microwave spectrum for both cases. When the FFP is not used, we would expect all eight heterodyning terms from the photodetector, thus resulting in all sidebands interfered with each other. However, when the FFP is used, we would expect to recover the LSB and USB data from signals (3) and (4) at 7 GHz and 12 GHz respectively.

Fig. 4.3(c) shows the measured microwave spectra of the signal at 12 GHz. When the FFP was not used, the PRBS spectrum was severely distorted, giving us a strongly interfered eye diagram in Fig. 4.3(d) and confirming our reasoning. Notice that the distortion of the spectrum was minimal when the FFP was used, resulting in an excellent eye diagram in Fig. 4.3(d).

Fig. 4.4 shows BER data for the case of pure SSB transmission TSSB transmission both with and without up-shifted carrier suppression. When the up-shifted carrier is

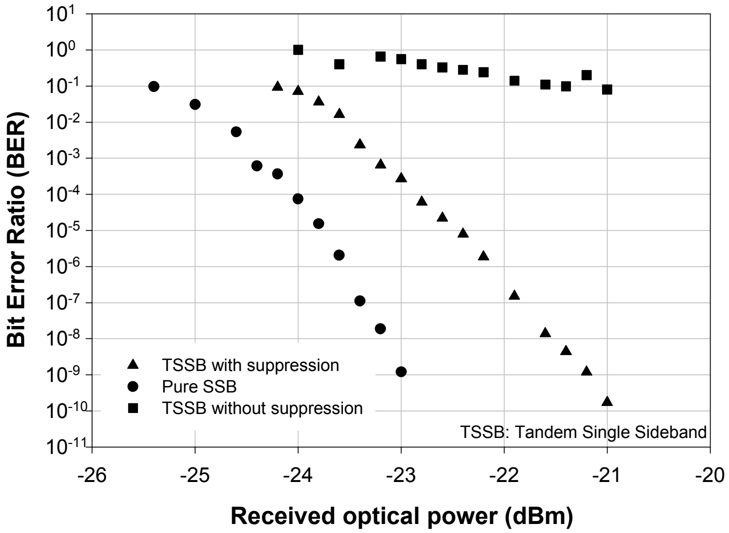

Fig. 4.4 BER data for a tandem single sideband (TSSB) transmission system for the case of purely SSB transmission, TSSB transmission without up-shifted carrier suppression, and TSSB transmission with up-shifted carrier suppression. A good BER curve are obtained for TSSB signals when the up-shifted carrier suppression is employed.

suppressed, a good BER curve is obtained, however there is a power penalty of a little less than 2 dB in comparison to the pure SSB case. We think that this is probably due to the imperfect suppression of the up-shifted carrier and may be improved by using a Fiber Fabry Perot with greater contrast in reflection mode.

In all of the above cases, sharp microwave filtering is used to distinguish between terms (3) and (4) , or the LSB and USB, enabling the system to tolerate the slow roll-off present in optical filters and thus eliminate guardbands.

4.3 Conclusions

We have successfully demonstrated a tandem single sideband receiver that achieves a heterodyning function without the use of an optical local oscillator and it's associated complexities. The heterodyne detection together with the sharp microwave filtering, allows the recovery of spectrally closely packed sidebands, independent of the quality of the optical filters used.

A key feature of the receiver design was the ability to obtain spectral separation between the carrier and the sidebands, and the ability to suppress the up-shifted version of the carrier. The ability to separate carrier from sidebands is an important function which could lead to considerable flexibility in the design of various types of coherent receivers which utilize the transmitted carrier as a local oscillator. In [23], the authors use a clever fiber-loop mirror to separate the carrier from an optical SCM spectrum. This however, would not work for our application since both SCM sidebands contain different data. It is however, functionally similar to the up-shifted carrier suppression that we perform in this chapter. However, we would like the suppression band to be as narrow as possible, while the authors in [23], wanted a slightly wider band in order to reject a broad baseband data stream.

In conclusion, while the receiver demonstrated in this Chapter performs the desired function it is complicated and places heavy demands on both photodetector bandwidth as well as the reflection mode suppression of a fiber fabry Perot which is difficult to achieve and unreliable in practice. A simpler solution must be found, or such components must become more stable if this kind of receiver is to become practical. The demonstration of coherent frequency shifting without the use of a local oscillator, however, opens the door to a number of techniques that hitherto were regarded as impractical owing to the phase locking and polarization tracking complications of a local oscillator. Some of these techniques are discussed in Chapter 5.

Chapter 5 Multifunctional microwave fiber optic links using a dual-electrode Mach-Zehnder modulator.

The interest in fiber-optic microwave and millimeter wave links has also prompted interest in experiments demonstrating the feasibility of implementation of different radio-system functionalities over RF photonic links, however in the past these investigations have involved the use of complex laser sources [26], or they have involved the use of an optical local oscillator [27]. In this chapter, we present various microwave optical link experiments, which demonstrate the implementation of multiple microwave system functionalities in the optical domain without the use of an optical local oscillator. All the experiments are centered around the dual-electrode Mach-Zehnder modulator and most of them will be described as a simple reconfiguration of the transmitter described in Chapter 3 or the receiver described in Chapter 4. This device and combinations of such devices demonstrate great potential for integration and hence may make viable candidates for future economical RF photonic systems.

We will demonstrate the following functionalities, depending on how the transmitter and the receiver in the link are constructed and operated:

1) a frequency shifting optical link that takes an input microwave signal and shifts it to another specified microwave frequency. A frequency doubling optical link, which is a more specific version of the above;
2) an optical link that accomplishes spectral inversion of an input microwave signal. This is useful for recompressing chirped RF pulses with the same circuit that was used to stretch them;

3) a down-converting optical RF link that down-converts input RF signals to baseband, thus reducing photodetector bandwidth requirements and eliminating the need for subsequent microwave down-conversion;
4) an RF photonic link that transports direct sequence microwave CDMA signals over optical links and accomplishes code-selective frequency conversion of selected channels enabling optical demultiplexing of CDMA channels.

5.1 RF Frequency translation and frequency doubling in optical links.

The purpose of this kind of link is to take as input, the original RF signal and the desired frequency shift, to transport the signal across the optical link and to deliver the frequency shifted or frequency doubled signal to the output. It turns out that this function is particularly easy to achieve using a tandem single sideband modulator. We use the USB to carry the microwave data and we use the LSB to carry an RF single tone, which is placed appropriately distant from the carrier frequency in order to provide the desired frequency shift. The maximum frequency shift obtainable from the optical link depends on the bandwidth of the modulator and the photodetector. In the case of the modulator the maximum frequency shift is exactly equal to the electrical bandwidth of the modulator, and in the case of the photodetector, the desired microwave signal after the frequency shift, should lie within the bandwidth of the photodetector. Complete phase correlation is present between the upper and lower sidebands at the transmitter, but chromatic dispersion may induce some phase decorrelation which may in turn cause phase noise in the recovered microwave signal [24]. Frequency doubling is achieved as a special case of frequency shifting wherein the single tone applied to the lower sideband is exactly equal in frequency to the carrier frequency of the microwave signal applied to the USB.

Fig. 6.1a and b show the expected optical and RF spectra and Fig. 6.2c shows the measured microwave spectra from a frequency doubling tandem single sideband link.

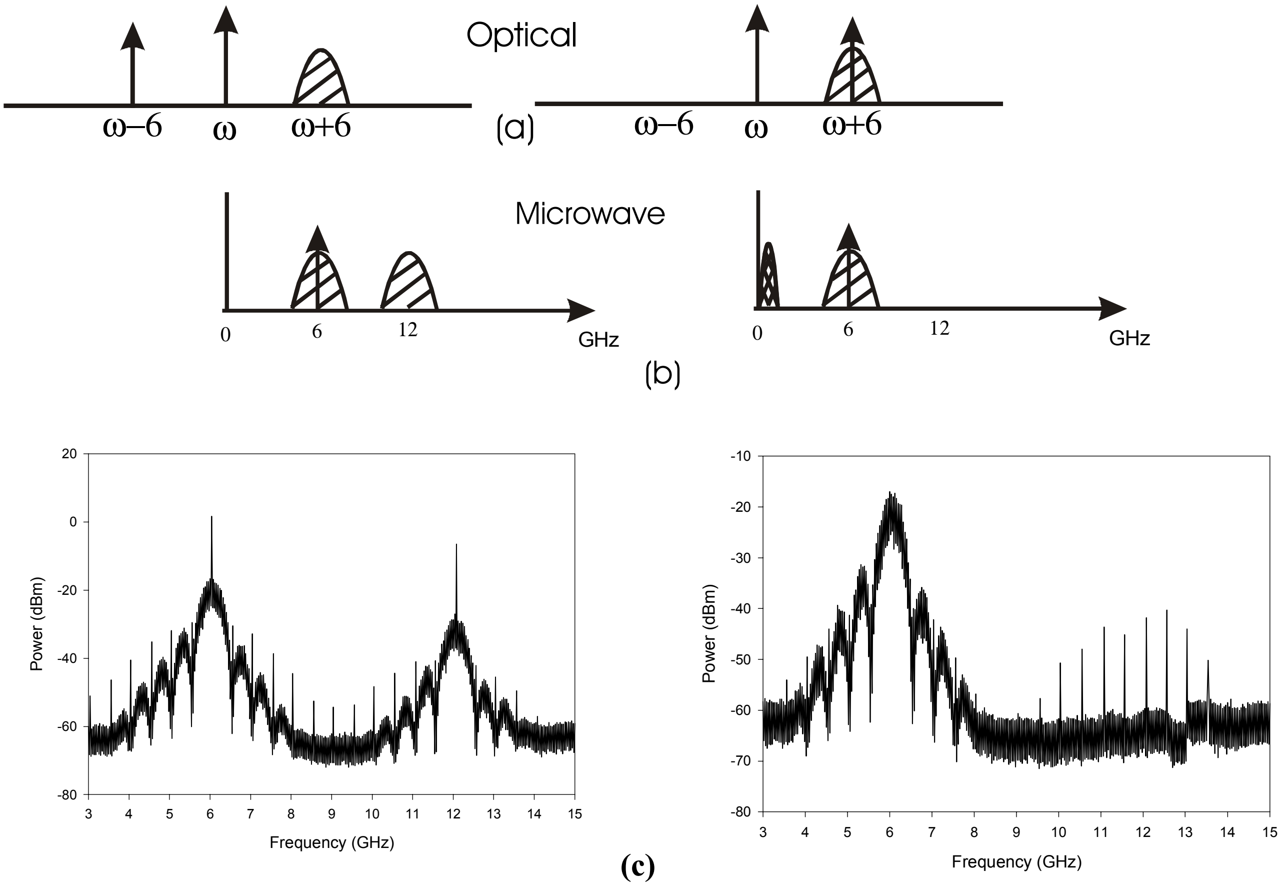

Figure 5.1 Expected a)optical and b)microwave spectra after photodetection obtained from a frequency doubling tandem single sideband link. The measured microwave spectra in c) show the frequency doubling effect when the single tone is placed in the lower sideband. No frequency doubling effect is seen when the signal is placed in the upper sideband. The microwave signal at the original frequency of 6 GHz can be eliminated by using a carrier suppression modulator.

The performance of this kind of link would be enhanced if a carrier suppression modulator were employed. We did not possess such a modulator at the time of this experiment, hence an unwanted out of band signal can be seen at the original microwave frequency. Recent designs of such carrier suppression modulators [28, 29] show great promise for the applications in this chapter.

5.2 RF Spectral Inversion over an RF photonic link

The purpose of this link is to spectrally invert and input microwave signal and supply the inverted signal at either the same carrier frequency or at a different carrier frequency at the output. Both the original signal and a single tone frequency higher than the carrier frequency of the original signal are placed in the USB of an optical carrier. If the original carrier frequency is desired, then the frequency would have to be double the carrier frequency. In this case, a carrier suppression modulator such as the one described in [28] would have to be used.

A second way to accomplish spectral inversion would be in a receiver scheme such as the one described in Chapter 4. It is clear from Fig. 4.2 that the up-shift in the second dual-electrode modulator and the subsequent beating of the LSB with the original optical carrier, causes the LSB to be spectrally inverted in the microwave domain. This kind of link is useful since the same microwave circuit that was used to stretch a chirped RF pulse, may be used to recompress it.

5.3 Downconverting RF photonic link

In this kind of link the microwave signal and it's carrier are placed in the upper sideband. If the input microwave signal is suppressed carrier, the carrier must be recovered by the use of electrical circuitry such as a Costas loop [18] in order to ensure exact phase and frequency matching. We had the luxury of having the carrier source in close physical proximity to the experiment, enabling exact phase and frequency matching with relative ease.

At the photodetector, the input microwave signal appears in the baseband, since its carrier is also transmitted. Fig. 6.1 shows the expected and measured microwave spectra for this case. Since the original carrier was not suppressed, a signal at the original RF carrier frequency is also expected. This can be suppressed by employing a carrier suppression modulator.

A second way to achieve frequency down-conversion is to employ the receiver DE-MZM described in Chapter 4 in LSB mode rather than in USB mode. The net effect will be to shift the whole optical spectrum down. If the appropriate sub-carrier frequency is chosen for down-shift, then the sideband will superimpose itself on the original optical carrier and may be directly detected. A down-shifted carrier suppression filter similar to the one employed in Chapter 4, will have to be used of course. Further experimental investigations in this regard are currently in progress.

5.4 Code-selective RF photonic mixing

The need for multiple access techniques in local area networks has inspired interest in optical code division multiple access (OCDMA), however due to the absence of optical devices capable of adding or dropping channels based on their codes, such networks are generally of a broadcast and select nature. A recent demonstration of OCDMA add-drop multiplexers [30], requires that all channels be received at the photodetector, with undesired channels being cancelled due to orthogonal coding. Receiving all channels at once from within the same bandwidth causes deleterious effects such as cumulative shot noise and speckle, which can seriously limit the number of simultaneous users [31]. In this section, we demonstrate a technique that coherently frequency shifts a direct sequence encoded optical channel by mixing it with an identically encoded RF local oscillator in a dual-electrode Mach-Zehnder modulator (DE-MZM). The spectral separation would reduce the effects of cumulative shot noise and speckle, and full code orthogonality is possible since the bipolar nature of the optical field is recognized by the frequency shifting process.

Figure 6.2 shows a block diagram of the experimental setup. For experimental convenience we do not encode the optical carrier itself but impose an encoded subcarrier on it. Using the subcarrier as an encoded optical carrier allows us to heterodyne the spectrum against the original un-encoded optical carrier to produce a microwave spectrum observable on an RF spectrum analyzer. The light source is a laser diode at f_{oc} GHz coupled into a DE-MZM which is connected in upper single sideband (USB) configuration [5]. To begin with we apply a ‘pure’, unencoded 6 GHz single tone to the first DE-MZM with no code imposed. This results in a ‘pure’ tone at (f_{oc}+6) GHz observable at 6 GHz on the spectrum analyzer as shown in Fig. 6.3a [5]. Applying a 1.5 MHz BPSK code C1(t) corresponding to the (1010) row of a 4x4 Hadamard matrix, to the 6 GHz frequency results in a ‘noisy’, encoded carrier at (f_{oc}+6) GHz observable at 6 GHz as shown in Fig. 6.3b. The BPSK modulation converts the 1s and 0s to phases of 0 and π, thus ensuring the bipolar nature of the code. At the decoder, we apply a low modulation depth 3 GHz signal with code C2(t) to the second DE-MZM, also in USB configuration. This had the effect of up-shifting the signal at (f_{oc}+6) GHz to (f_{oc}+9) GHz as in Chapter 4. The optical signal was then amplified and photodetected, and the signals at 6 GHz and 9 GHz were observed on an RF spectrum analyzer.

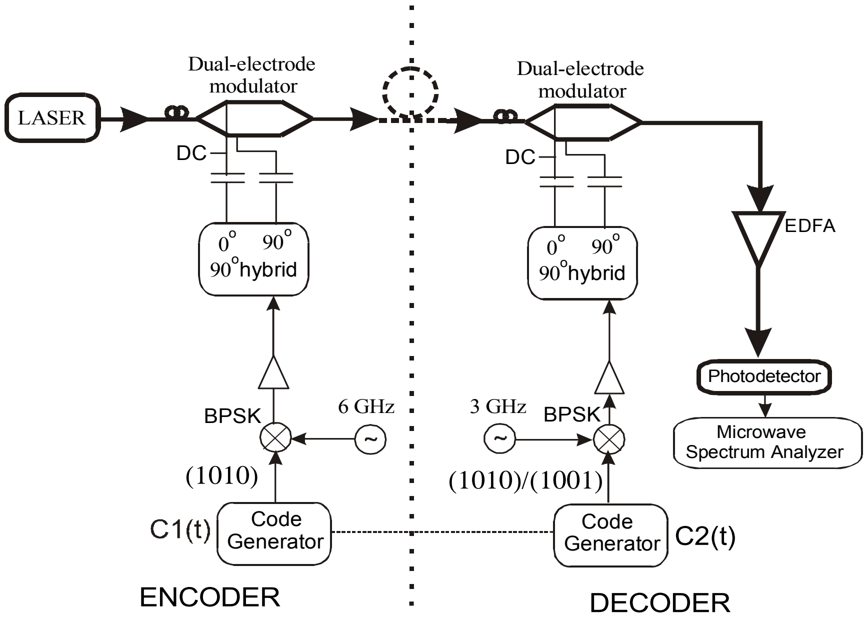

Figure 5.2 Experimental setup to demonstrate code-selective RF photonic mixing

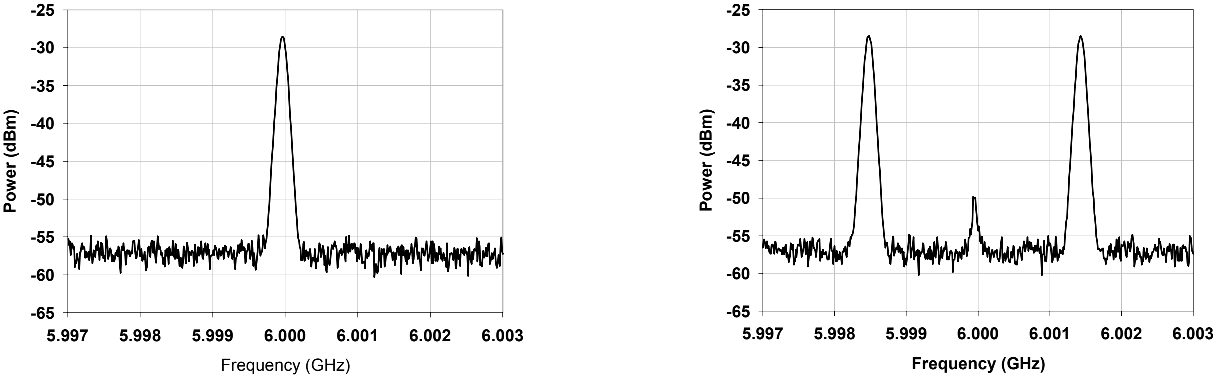

(a) **(b)**

Figure 5.3 Signal obtained at 6 GHz after heterodyning with original optical carrier for a) "pure" unencoded sub-carrier and b) "noisy" sub-carrier encoded with 1.5 MHz chip-rate (1010) code.

We observed the signal at 9 GHz for two different cases of C2. ***Case 1***. Code C2 is identical to C1, i.e. both were (1010) but delayed by an appropriate amount to compensate for the delay through the system. Fig 3a shows the 'pure' un-encoded carrier recovered at 9 GHz. The delay for C2 was tuned to get best carrier recovery. ***Case 2***. Code C2 is chosen to be (1001) i.e. orthogonal to C1, and tuned to get best carrier suppression at 9 GHz, delayed by the same amount as in case 1. In Fig. 3b no carrier is seen at 9 GHz indicating that the up-shift is indeed code selective.

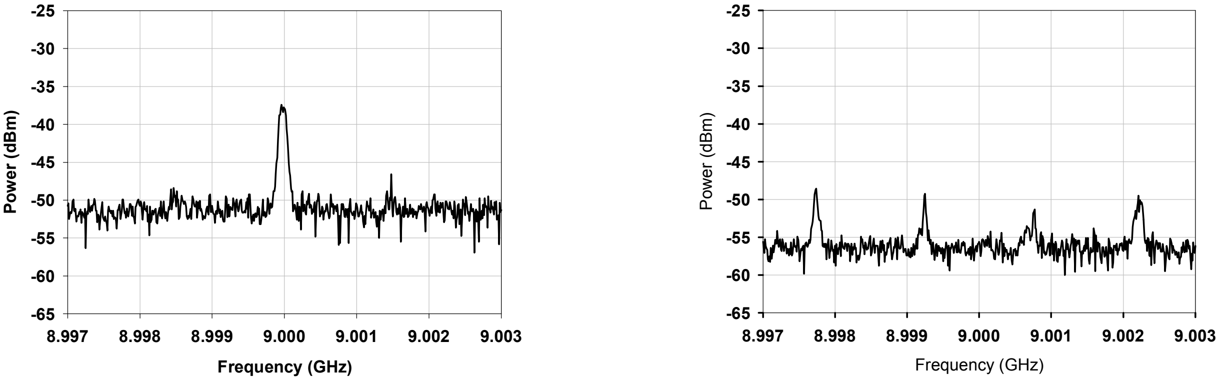

(a) **(b)**

Figure 5.4 Signal obtained at 9 GHz after heterodyning with original optical carrier when code C2(t) is a) (1010) i.e. identical to C1(t) and b) (1001) i.e. orthogonal to C1(t). The carrier is recovered at 9 GHz when the codes are matched. Unmatched codes are rejected indicating the code-selectivity of the wavelength shift.

5.5 Conclusions

Several radio-system functionalities were demonstrated in this chapter. Most of them were implemented through the simple modification of the SSB or TSSB transmitter or receiver. While the proposals are feasible enough from the point of view of the design, further tests need to be done to determine the link performance. The ability to implement these radio system functions while simultaneously achieving transport of an RF signal may have a great deal of application in the fiber-wireless area. In addition the frequency doubling and shifting link described in 5.1 may be used to transport low phase noise RF local oscillators. The phase noise is low on account of common mode cancellation of the phase noise in the USB and LSB since the carrier, USB and LSB are phase correlated from the modulation process.

We also described an experimental demonstration of code-selective wavelength conversion that can be used to demultiplex direct sequence encoded optical CDMA channels. The results we obtained confirm that we have demonstrated code selective wavelength conversion using RF photonic mixing in a DE-MZM. Unmatched channel rejection with the use of an orthogonal code was demonstrated. The bipolar nature of the optical field is recognized since the frequency shift happens before photodetection, thus allowing full code orthogonality. A coherent effect has been achieved without the use of an optical local oscillator and the associated difficulties of optical phase locking and polarization tracking. The spectral separation of the desired channel could lead to reduction in the effects of cumulative shot noise and speckle, which is important in order to support more simultaneous users [31]. The ability to pick out a signal from a spectrum and frequency shift it based on its code may have potential applications in routing techniques such as optical label switching. Such a link could also be used to carry microwave CDMA signals over fiber optic links with the ability to demultiplex them in the optical domain.

While, the demonstration of such functionalities can lend considerable flexibility to RF photonic links, it is important to realize that the dual-electrode Mach-Zehnder modulator is currently an expensive and bulky component. It is important to achieve some level of integration so that these functions can be implemented in an economical way to create flexible and multi-purpose RF photonic links.

Chapter 6 Silicon-on-Insulator Nanophotonics

The transmitter and receiver designs proposed in the previous chapters require the use of expensive active components. These include sophisticated devices such as the dual electrode Mach-Zehnder modulator which was used to perform the function of microwave photonic mixing. Such increased sophistication in communications circuits, as well as the integration of optical functions into other processing and control systems is significantly impeded by the cost and complexity of the different optical components that currently exist in diverse material systems. In order to truly exploit the potential of optical functionalities across a broad range of applications, it is essential to realize ultra-compact multi-functional optics on a single material platform.

Nanophotonic circuits offer one such option. The evolution of microelectronic technology has now reached the stage where device features that are significantly smaller than the optical wavelength can easily be fabricated with very high precision. To take advantage of this trend, it is necessary to make correspondingly small optical devices. A very high degree of miniaturization demands a high index contrast, in order to achieve small bend radii and greater confinement. On the other hand, such high index contrast structures are more susceptible to process inaccuracies and scattering due to surface roughness. These problems are being addressed by continued progress in microelectronics fabrication.

Semiconductor systems such as InP/air and Si/SiO2 offer the high index contrast necessary to create such structures. Additionally, these semiconductors exhibit very low absorption at 1.55 μm, which is the wavelength of interest for optical communications. While the InP/air system is very attractive on account of the potential to integrate optically active and passive devices on a single chip, InP is still beset by processing issues, and is not the material of choice in the electronics industry. This issue assumes special importance since many optical devices require the presence of significant electronic control in order to work effectively. A silicon based material system, on the other hand, offers the possibility of integrating both electronic and optical functions on a single substrate, with processing technology that is already well understood and in wide industrial use. The rest of this chapter will briefly discuss silicon optoelectronics, with specific reference to the Si/SiO2 material system that offers great potential for the integration of both electronic and optical functions on a single substrate. In particular, we will discuss the problem of coupling light into an SOI nanophotonic IC, which will motivate the work in the rest of this dissertation.

6.1 Silicon-on-Insulator Optoelectronics

There has been a great deal of recent interest in Silicon optoelectronics [32-41]. Pioneering work by Soref and others led to the development of numerous passive and active optical devices on Silicon substrates [42-43]. Silicon optoelectronics refers to the integration of both optical and electrical functions on a silicon chip. This offers unique advantages, since processing technologies are very well established in silicon, and the photonics may thus be seamlessly integrated along with the electronics, using a CMOS process. In particular, SOI has attracted great attention on this front [34-35, 42]. SOI has already emerged as a future technology for high-speed, low-power electronics on account of its ability to provide improved circuit performance and guaranteed latch-up free circuits as compared to bulk silicon. Ever since the first successful SOI manufacturing process, there has been considerable effort directed towards resolving the numerous materials issues confronting the technology. In addition to the advantages it offers electronics, SOI offers some unique advantages to optics, such as the existence of a guiding layer as seen in Figure 6.1. The superficial silicon layer sitting over a buried oxide layer forms a high index contrast optically confining layer where both electronic and optical components may be housed. In fact, the potential that SOI offers is being increasingly noticed in the photonics community, with work directed towards making passive spectrally selective devices [42] , couplers [44], as well as active devices such as modulators [45-49] and photodetectors [50-51]. The ultimate vision is that of a photonic/electronic integrated circuit that can be fabricated using a CMOS compatible process.

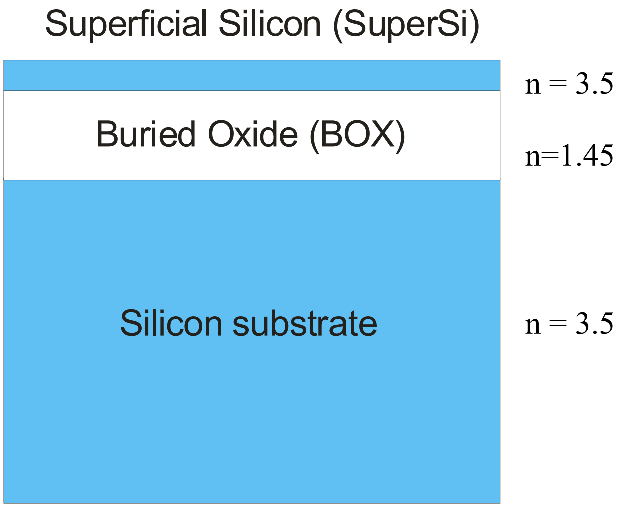

Figure 6.1 The Silicon-on-Insulator material system. Apart from the electronic advantages of such a system, the superficial silicon (SuperSi) may be used as a guiding layer for optics, thus enabling the integration of photonic and electronic devices on a single substrate.

A quick remark about the light source is in order. Even though there have been recent promising developments in the area of developing a silicon-based light source [52], there is still much work to be done in this area. This is a significant disadvantage for a silicon based material system, but it is not prohibitive. A silicon nanophotonic IC could derive its optical power from an off-chip light source in much the same way that an electronic IC uses an off-chip power supply. Such an architecture would require the coupling of light from SMF into the IC, and vice versa.

6.2 The coupling problem

Building photonic devices in a high index contrast material system enables waveguides with smaller bend radii and greater optical confinement. On the other hand, the high index contrast photonic system comes with a penalty. The Si/SiO2 index contrast requires that in order for a single mode condition to be maintained, the waveguiding layer has to be approximately between 200 and 300 nm thick. This results in a huge mismatch with the guided mode in standard single mode fiber (SMF), precluding the use of simple end-fire coupling on account of prohibitive insertion losses.

Figure 6.2 shows a to-scale picture of the SMF core, and the cross section of a photonic crystal waveguide in a thin film of Silicon. The SMF core is approximately 50X larger than the waveguide core, but the difference in mode sizes is larger on account of the difference in index contrast between the two systems. This necessitates the development of a low insertion loss I/O interface.

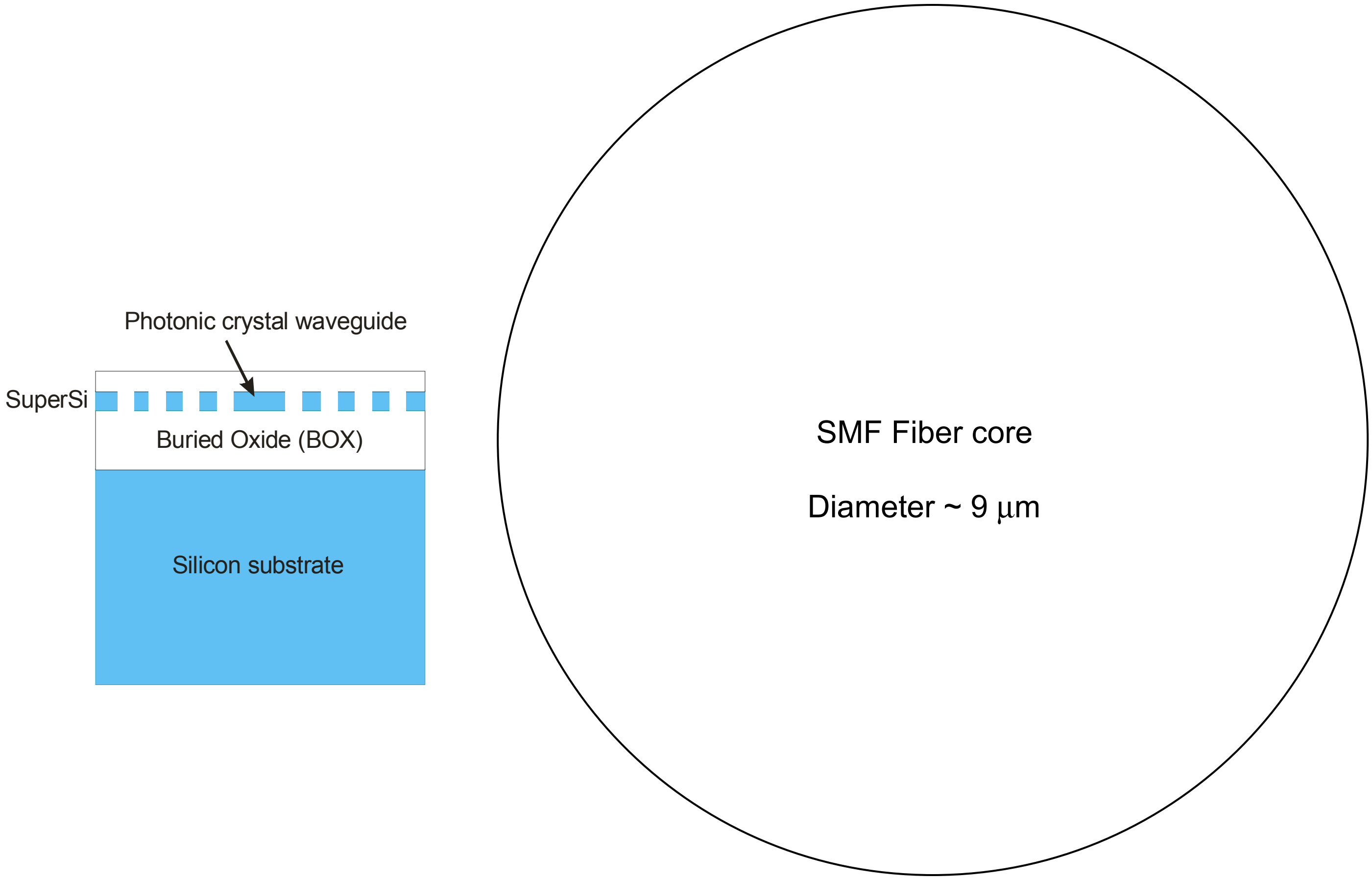

Figure 6.2 To-scale representation of single mode fiber core next to waveguide in a 2D photonic crystal thin film. There is a huge mismatch in the size of the modes making simple end-fire coupling techniques highly inefficient.

6.3 Requirements from the fiber-IC interface

The requirements of such an interface are simple:

1. *Efficiency*

This is, by far, the most important requirement. High insertion losses translate into degraded system performance and may completely preclude the use of silicon photonics in tight power budget systems.

2. *Bandwidth*

The bandwidth needs to be large enough to allow multiple wavelength channels to couple in through one device. The number of channels is decided by system architecture, but the interface needs to couple as large a bandwidth as possible, with as flat a passband as possible.

3. *Low Polarization Dependent Loss (PDL)*

The polarization of light in optical fiber at the end of a link is random and unpredictable. The device needs to couple light in both polarizations into the IC without preference. Any preference translates into power loss which will convert polarization fluctuations into power fluctuations, thus degrading system performance.

The design of a practical device must address these design criteria.

6.4 Possible candidates

Two possible candidates present themselves for the efficient coupling between SMF and the silicon thin film:

1. *Adiabatic tapers*

Figure 6.3 shows an adiabatic taper. Adiabatic tapers start with a large mode and gradually modify the effective index of the waveguide so that the mode can adapt without excessive losses. If the slope is gentle enough to satisfy an adiabatic condition, then it is possible to make very efficient interfaces. While these devices have attracted some attention to solve the coupling problem, tapering in two dimensions implies that the taper must be non-planar, requiring gray scale masking. CMOS processes are usually planar thus making fabrication of such tapers along with electronics an issue. Furthermore, the etch used to fabricate the taper needs to result in a very smooth profile. Any roughness will translate into large scattering losses on account of the high index contrast. A third disadvantage is the reflection that results at the interface between the fiber and the high index silicon taper. The taper needs to be anti-reflection coated, resulting in a further non-planar process.

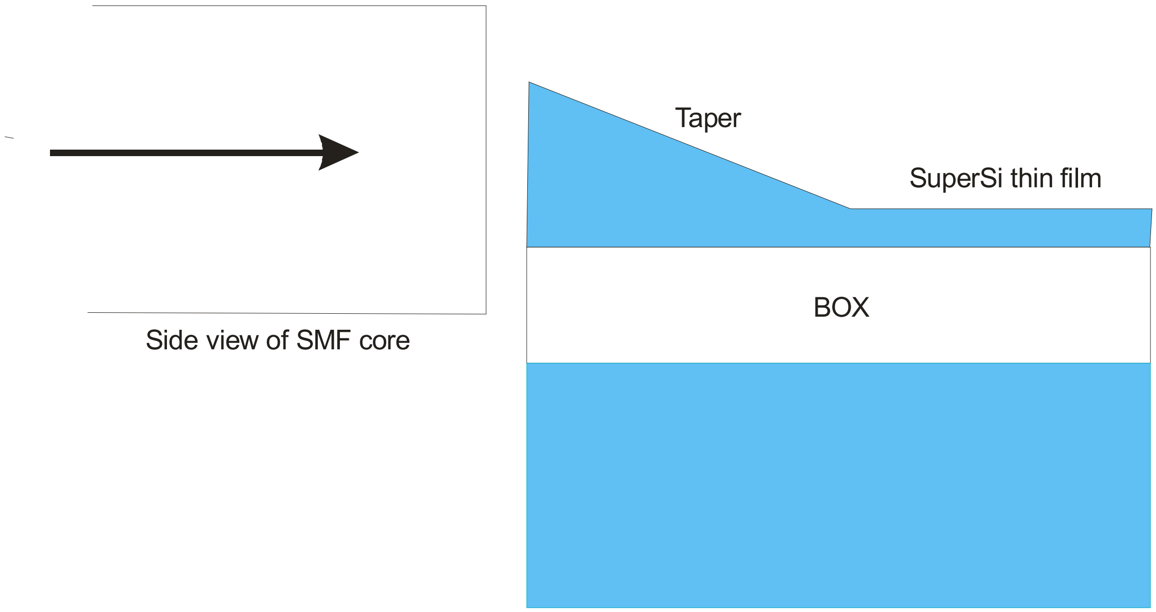

Figure 6.3 Adiabatic tapers may be used to make a gentle transition between the disparate modes, however the fabrication of such tapers involves non-planar processes such as gray scale masking. In addition, surface roughness can lead to excessively lossy tapers.

2. Grating couplers

Figure 6.4 illustrates the the use of a grating coupler to couple the light from SMF into a nanophotonic IC. The grating is a series of perturbations in the waveguide that scatter the light from a fiber into the high index contrast waveguide. Since it is a completely planar device, it is well suited for adaptation to a CMOS process. The grating enables top-side coupling of the light into the waveguide. The anti-reflection features of the grating are built into the design, so no separate non-planar anti-reflection coating is required. The rest of this dissertation describes the main issues confronting the design, fabrication and characterization of such couplers. Designing an efficient grating coupler is an extremely computationally intensive exercise. The chapters that follow will demonstrate this, while attempting to bring physical understanding to the mechanism of low loss grating couplers. Using the understanding developed, we will propose a novel design for a low insertion loss grating coupler, and describe a proof-of-concept experiment to verify it.

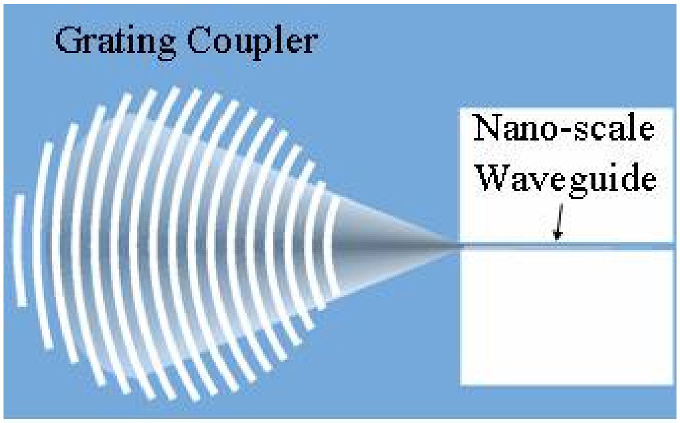

Figure 6.4 Grating couplers are planar devices that may be fabricated by standard CMOS processes. The grating coupler serves to couple light from the fiber into the thin film. Coupling into the nanoscale waveguide may be accomplished by curving the grating teeth, thus accomplishing a simultaneous focusing function.

6.5 Conclusions

Silicon-on-Insulator shows great promise as a material system for the integration of photonics and electronics on a single substrate. However, due to the lack of a well-developed silicon laser, it is necessary to couple light into a silicon photonic IC from an external light source. This requires the development of a key enabling technology viz. an efficient, low insertion loss interface between SMF and the nanophotonic IC.

Chapter 7 Grating coupler design

This chapter deals with the theory of grating couplers, with specific reference to coupling efficiency. While the coupling mechanism of gratings is well understood, the issue of efficiency has not been studied in as much detail. The main perceived disadvantage of grating couplers for low insertion loss fiber-waveguide interfaces, is that a substantial portion of the incident energy is transmitted through the film and then lost in the substrate. For this reason, grating couplers were traditionally considered much less efficient than prism couplers [53].

Grating coupler action can be considered on two levels. The ***microscopic*** study of the grating coupler can be described as the study of variation in coupling strength as a function of the various grating parameters such as depth, refractive index contrast, grating tooth profile, duty cycle and period. While considerable effort has been made to develop analytical [54-56] and numerical [57-58] models to evaluate the grating's microscopic properties, relatively little work has been done to investigate the grating coupler's ***macroscopic*** properties which include a physical understanding of how the grating functions as a whole device, and how its overall properties are affected by surrounding structures. It also includes the understanding of how grating efficiency is affected by external factors such as beam profile and beam alignment. To get a flavor for this, consider, as a simple illustration, the grating shown in Figure 7.1(a). In this case, the microscopic and macroscopic behaviors of the grating are identical. However, adding a single interface underneath the grating as in Fig. 7.1(b), such as exists in a Silicon-on-Insulator (SOI) substrate, can make a substantial difference. This is easily understood, if one considers that light out-coupled into the substrate will now be reflected back into the grating, and undergo additional scattering, with some light coupling back into the waveguide. The successive reflections and scatterings sum up in an infinite geometric progression. This modifies the coupling length, as well as the distribution of power between the substrate and cover. The scattering and power distribution is now a strong function of the thickness of the buried oxide layer [59] since this affects the optical phase of the light that is re-coupled into the waveguide. This simple example of a single interface below the grating, reveals that the eventual efficiencies will be decided by a complex interaction of various beams bouncing around inside the grating structure.

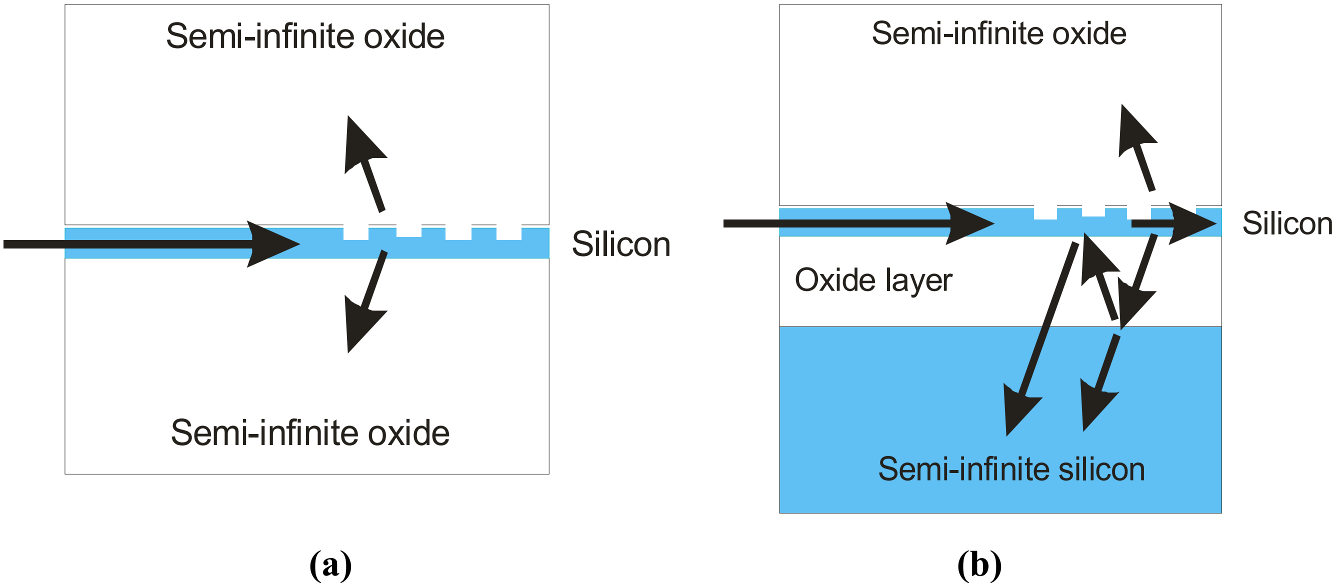

Figure 7.1 The interfaces and structures surrounding a grating affect its its coupling length. The grating in (a) has a coupling length that is modified by the additional interface in (b). The cover/substrate coupling ratio is also affected by the additional layer in (b).

A grating's efficiency and coupling properties may thus be affected by the materials and structures that surround it. This is encouraging from the point of view of efficiency enhancement, since it gives us additional control over the grating's properties. To design an efficient coupler it is important to gain a thorough physical understanding of the way these properties are affected, and how the grating and its surrounding structures relate to the operation of the coupling device as a whole. Note that this chapter does not make any attempt to quantitatively analyze the coupling strength at a microscopic level, but rather seeks to create a physical understanding of grating coupler operation, and to provide an insight into the design issues that confront such couplers.

Since grating couplers are non-magnetic, they are reciprocal devices. Accordingly, this chapter will switch back and forth between the in-coupling and out-coupling configurations for grating couplers, depending on which of these configurations better serves to explain a particular design concept.

7.1 The Design Problem

The design problem is summarized in Fig. 7.2. We need to suppress P_{trans} and P_{refl} while channeling all the power into either P_{back} or P_{forw}. Either P_{forw} or P_{back} may be suppressed by phase matching and appropriate choice of grating period. The suppression of P_{trans} and P_{refl} is not so straightforward, and after a brief discussion of momentum matching, much of the rest of the chapter is devoted to understanding the nature of P_{trans} and P_{refl}, together with ideas to suppress them. In fact, efficient grating design is just about suppressing these two beams.

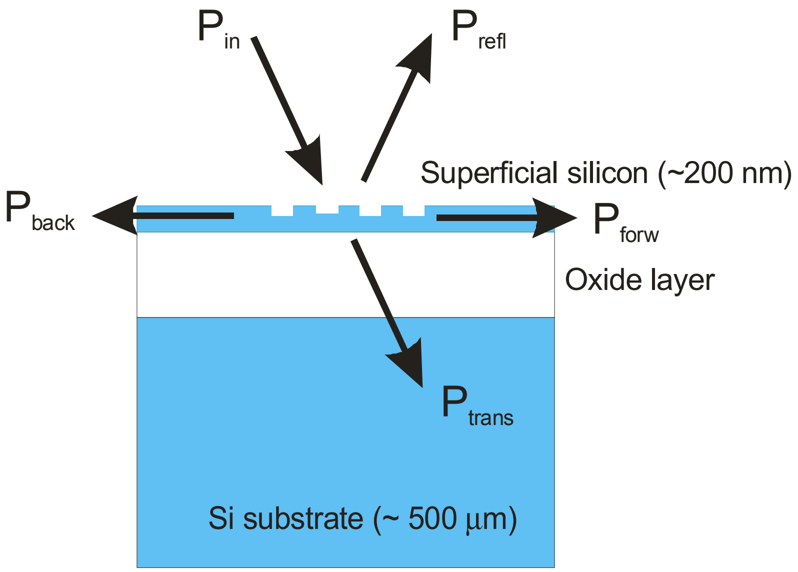

$$P_{in} = P_{back} + P_{forw} + P_{trans} + P_{refl}$$

Figure 7.2 The Design Problem. We need to suppress P_{trans} and P_{refl}, while channeling as much as possible of the input power into either P_{forw} or P_{back}.

7.2 Prior Work

This section discusses prior work in the area of grating couplers, with particular reference to efficiency enhancement. The first report of coupling from a beam into a thin film waveguide by using a grating was reported by Dakss et al [60]. The grating was made of photoresist and exposed by laser interferometry. This was followed by much work investigating grating couplers and periodic dielectric structures. [53-54, 61-65].

The theory of grating couplers was initially investigated using coupled mode theory [66], and then by a more sophisticated leaky wave approach [54-55,63], proposed by Tamir and Peng which provided some of the first analytical formulations for the microscopic design of grating couplers. These works, however, regarded the grating coupler as an inherently inefficient device, on account of a substantial portion of the incident energy being transmitted through to the substrate.

The first attempts to address the efficiency issue were through the addition of a small prism above the grating coupler [67], and through the use of blazing, which breaks the cover/substrate coupling symmetry of the grating coupler. In out-coupling mode this meant that the grating coupler preferentially coupled the guided mode into a cover mode. This meant that for incoming beams, the power transmitted through to the substrate was reduced. The first experimental demonstration of such a concept was by Aoyagi et al [68], who used an angled ion beam etch to blaze gratings in poly methyl methacrylate (PMMA) in a 7 to 30 degree range, showing an increase in the cover coupling as a function of blaze angle. This was followed by much theoretical and experimental work in blazed grating design [69-79]. While blazed gratings are well-established and proven as a technique to enhance coupling efficiency, they are not appealing for CMOS compatible integrated optics on account of the non-planar processing that is required to fabricate such devices.

The intensive work in the 1970s was followed by a hiatus through the 1980s. Activity in grating coupler research resumed in the 90s, starting with the use of grating couplers for planar optic disk pickup [80-81]. In the late 1990s and early 2000s, the grating coupler was revisited by a number of groups in an attempt to enhance its efficiency for use in integrated optics, including integrated optics on SOI substrates [82-84]. The presence of an additional high index contrast layer beneath the grating caused more attention to be paid to the macroscopic design properties of the grating, especially the effect of the buried oxide (BOX) layer. Emmons and Hall modeled the effect of the

BOX layer on grating performance in 1992 [59]. The macroscopic properties of grating design had originally been explored in a paper by Ulrich in 1972 [85], and many of the concepts presented there were revived in the context of efficiency. While blazing was revisited briefly in SOI [83], most groups began to recognize the importance of using a planar process to enhance efficiency.

The most successful recent designs to enhance coupling efficiency in SOI, include the use of substrate coupling together with a mirror above the grating to block the transmitted beam [82] achieving an in-coupling efficiency of 57%, and the use of a second grating to break the symmetry of normal fiber to waveguide coupling [84], achieving an in-coupling efficiency of 19%. While the mirror approach allows a large efficiency enhancement, it requires a backside polished substrate, since the beam is coupled through the substrate. The efficiency may also be decreased by diffraction in the thick substrate. The approach in [84], despite being planar, requires the presence of a reflective stack beneath the grating coupler to reduce insertion loss further. The area beneath the grating coupler may not be accessible for processing in a practical CMOS process.

7.3 Momentum Matching

The qualitative aspects of the momentum matching are very simple to understand. The tangential component of the wave vector of an incident light wave is too small to match to the wave vector of the surface wave in the high refractive index film. The grating coupler is meant to provide a spatial modulation of the light wave thus adding integer multiples of its own reciprocal lattice vector to the incident wave vector. If one of the resultant harmonics matches the wave vector of the surface wave, then the light couples into the waveguide. This is illustrated in Figure 7.3. Clearly, for a given wavelength and incident angle, it is possible to choose a grating period that matches the momentum of one of the guided modes with the horizontal component of the given free-space mode. The counter propagating mode may thus be suppressed since the contribution from the crystal momentum and its harmonics will lead to momenta that are either too great or too small to be supported by the waveguide. A sufficiently large magnitude of K_{grat}, will ensure the suppression of the higher order grating orders that serve to degrade the efficiency. Thus, the choice of period determines which of the modes we will couple into, as well as ensuring that higher grating orders are suppressed, thus eliminating a source of inefficiency.

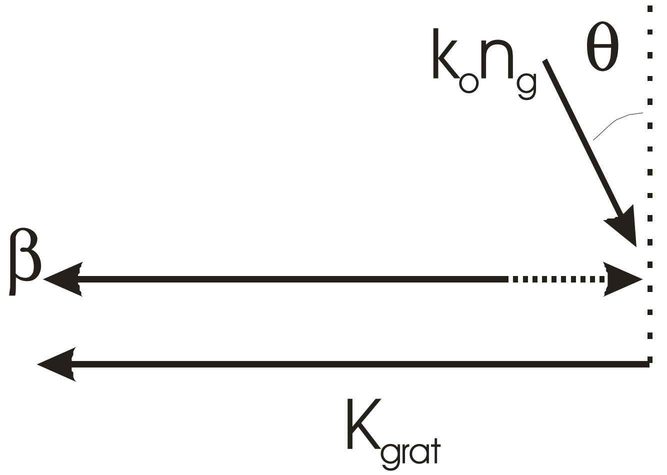

Figure 7.3 Momentum conservation in grating couplers. The horizontal component of the incident wave vector receives additional momentum (K_{grat}) from the spatial modulation due to the periodicity of the crystal. If one of the resultant harmonics matches the guided wave vector, coupling occurs.

7.4 The grating as an array of scattering elements

As a starting point, let us reframe the design problem in an out-coupling sense as shown in Figure 7.4. Assuming that the thin film is single mode, and that the grating period is chosen so that only one outcoupling diffraction order is present, then the grating creates two outcoupled beams: one in the cover and one in the substrate. Let us call these beams A, B and C as shown in the figure. Since the grating is a completely reciprocal device, the coupling coefficients $K_{AB} = K_{BA}$ and $K_{AC} = K_{CA}$. In other words, the efficiency of coupling from A to B must equal the coupling efficiency from B to A. To ensure efficient coupling from B to A, we need to maximize coupling from A to B, thus requiring the suppression of beam C.

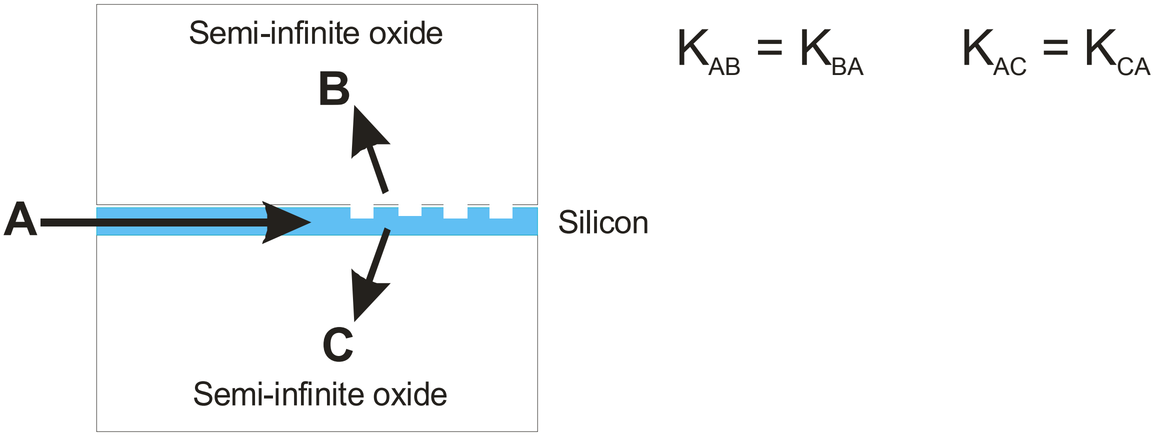

Figure 7.4 The grating in out-coupling configuration. Assuming the grating is phase matched to produce only one diffraction order, the grating scatters into two beams, B and C. Reciprocity dictates that the coupling coefficients $K_{AB} = K_{BA}$. Efficient design thus reduces to eliminating the beam C.

While reciprocity mathematically explains the equivalence of the coupling coefficients, K_{AB} and K_{BA} , it is worth our while to gain a physical understanding of exactly how this reciprocity comes about, in terms of beam creation and destruction. To simplify the problem a little, let us consider a grating with a 100% reflective mirror beneath it, as shown in Figure 7.5(a)

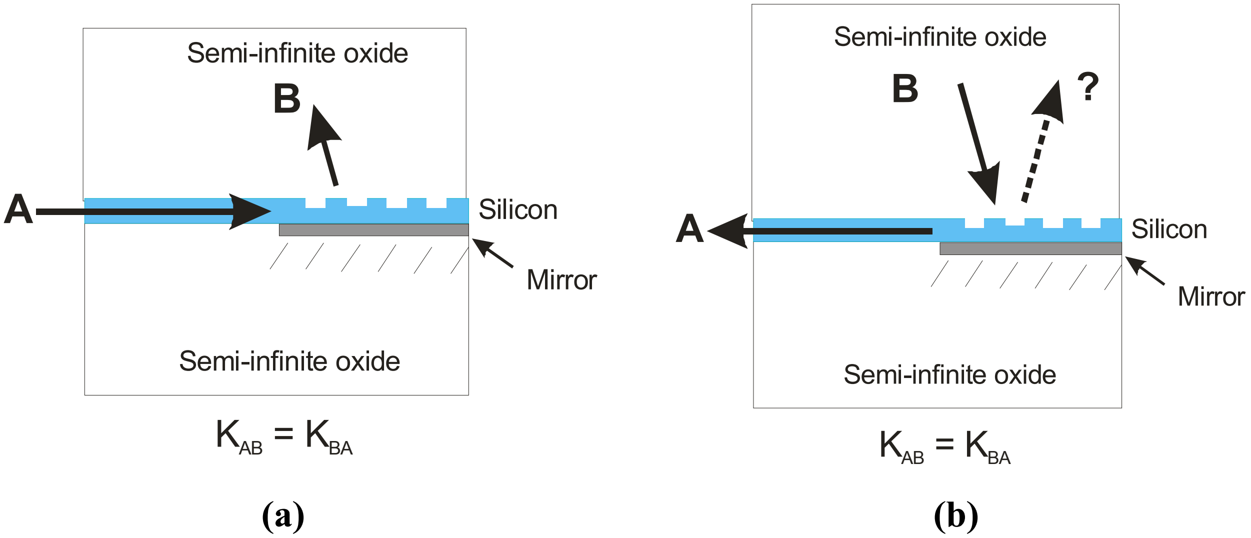

Figure 7.5 Consider a grating with a mirror underneath. This results in the elimination of half the phase space (a), thus eliminating beam C. In the in-coupling case (b), the beam B is converted completely into the guided mode A. However, what becomes of the reflected beam?

Clearly this would eliminate half the phase space, thus eliminating beam C, placing all the power in beam B. By reciprocity, if an input beam B is incident on the grating would all be converted to beam A. Reciprocity further suggests that if the input beam has the same profile and shape as the output beam, then the coupling will occur with an efficiency of 100%. What happens to the reflected power however? In the following paragraphs we will attempt to understand how the reflected beam is created, and the exact physical mechanism behind its elimination. This will lead to a better understanding of both the transmitted and reflected beams, and lead us to an understanding of the other design considerations viz. incident beam profile and beam width. Even though we use only half the phase space in our analysis, the results are easily generalized to a grating that is free to couple into both cover and substrate.

Let us consider the grating coupler as a series of distributed scattering centers, somewhat analogous to a phased array antenna as shown in Figure 7.6. Each element is small enough to ensure that only the amplitude and phase of the input electric field need be considered over the length of a single element.. Then, each of these individual scattering elements may be treated as a four port device as shown in the middle section of Figure 7.6. We may describe the scattering properties of this four port device by a complex scattering matrix.

$$\mathbf{S} = \begin{array}{ccccc} \textit{Ports} & 1 & 2 & 3 & 4 \\ 1 & 0 & s_{12} & 0 & s_{14} \\ 2 & s_{21} & 0 & s_{23} & 0 \\ 3 & 0 & s_{32} & 0 & s_{34} \\ 4 & s_{41} & 0 & s_{43} & 0 \end{array}$$

The zeros in the scattering matrix come from the phase matching selection rules of the grating which do not allow for a coupling coefficient between certain pairs of beams For example, there can be no coupling between ports 1 and 3 since the grating scatters some of the light from port 1 into port 2 and the rest goes straight through to port 4.

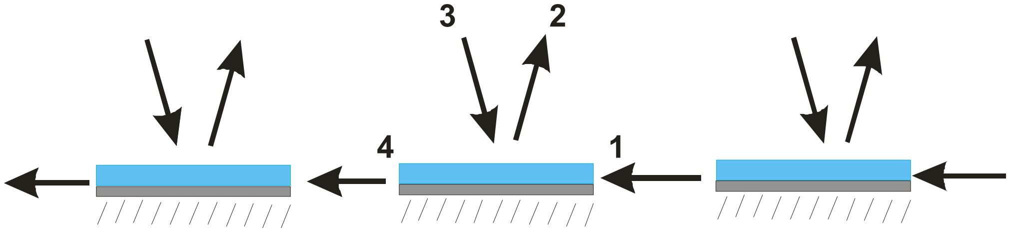

Figure 7.6 The grating may be treated as a series of scattering elements, analogous to a phased array antenna. Each of these scattering elements may then be represented by its own complex scattering matrix.

For an input field vector Ei, the scattering element yields

$$E_0 = \mathbf{S}E_i$$

Since the grating is made from lossless dielectrics and the mirror is 100% reflective, conservation of energy requires that the matrix ***S*** be unitary, or that $S \bullet S^+ = I$. This leads to the following equations that relate the scattering coefficients.

$$|s_{32}|^2 + |s_{34}|^2 = 1 \tag{7.1}$$

$$s_{12}s_{32}^* + s_{14}s_{34}^* = 0 \tag{7.2}$$

The first of the two equations suggests that the power in input beam 3, is divided between beam 2 and beam 4, which is in accordance with the phase matching condition of the grating. The second equation relates the specular reflection coefficient s_{32} with the leaky wave coefficient s_{12}. This relationship is of particular importance since our formulation implies that the reflected field coming from port 2 consists of two components given by:

$$E_2 = s_{12} \cdot E_1 + s_{32} \cdot E_3 = E_{leaky} + E_{specular} \tag{7.3}$$

The reflected field thus consists of:

1. The component that is reflected due to specular reflection from the high index surface
2. A second component that arises from light that is outcoupled from the grating. The outcoupled light was incoupled at a prior scattering center.

In addition, the phase matching condition allows us to treat s_{14} and s_{12} as being in phase. From equation (7.2), we can therefore infer that s_{32} and s_{12} are out of phase. This is not particularly surprising considering that one of the scattering coefficients is a reflection coefficient from a high index surface. It is significant that the two scattering coefficients are required to be out of phase, just from conservation of energy. This offers great promise for the design of an efficient grating. If the reflected and transmitted fields each have two components, then matching the field components in magnitude and ensuring that they are both of exactly opposite phase could potentially result in the elimination of these two beams. The concept of the reflected beams consisting of two components has been suggested in [86], but it has not been formally used for the design of more efficient couplers.

7.5 Reflection from a leaky wave surface

We will now use the knowledge gained from the previous section to investigate the effect of scattering strength on the reflection of a beam from a leaky wave surface. Consider a grating with a 100% reflective mirror phase matched to allow beams as in Figure 7.7.

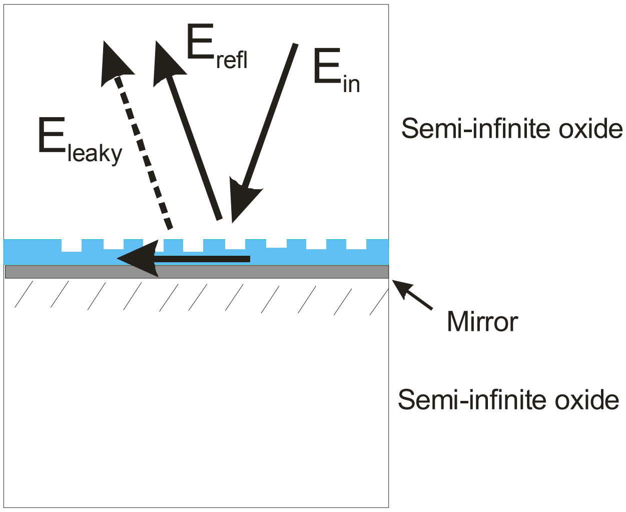

Figure 7.7 A grating with a reflector phase matched to allow the beams indicated. The diagram shows the two components of the reflected beam, created when the grating is excited with an input beam.

We now divide this grating into a hundred scattering centers of uniform strength, along its length from left to right, and excite it with an input field, $E_{in.}$ Figure 7.8 shows the input field incident on the grating as a function of scattering center. We have chosen a Gaussian input beam centered on the sixtieth scattering center.

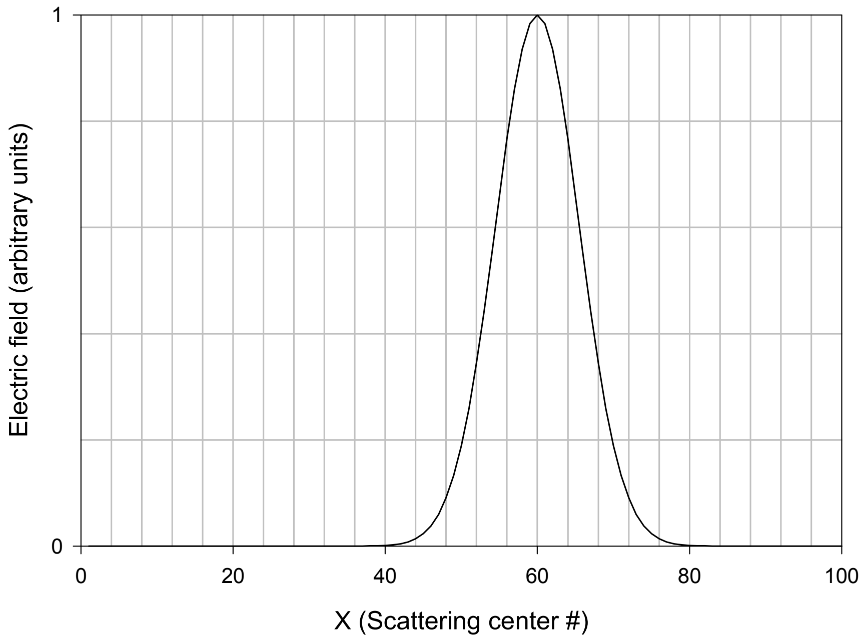

Figure 7.8 Input field profile E_{in} as a function of scattering center

Using the scattering matrix formulation in the previous section, it is now possible to determine the shape of the reflected field profile, for a given scattering strength. Figure 7.9 shows the reflected field profile for input beam to waveguide scattering strength magnitudes of 0.1, 0.2, 0.3, and 0.4. Each plot shows the contribution of the leaky wave component of the reflected beam, the specular reflection component of the reflected beam, and the general form of the overall reflected intensity. The graphs clearly indicate that the contribution of the leaky wave component increases with an increase in scattering strength. This is to be expected since more light is coupled into the waveguide and is coupled back out. This process of incoupling and outcoupling also leads to a lateral shift in the reflected beam which increases with an increase in grating strength. This is a characteristic of reflection from any leaky wave surface [86]. Gratings are no exception.

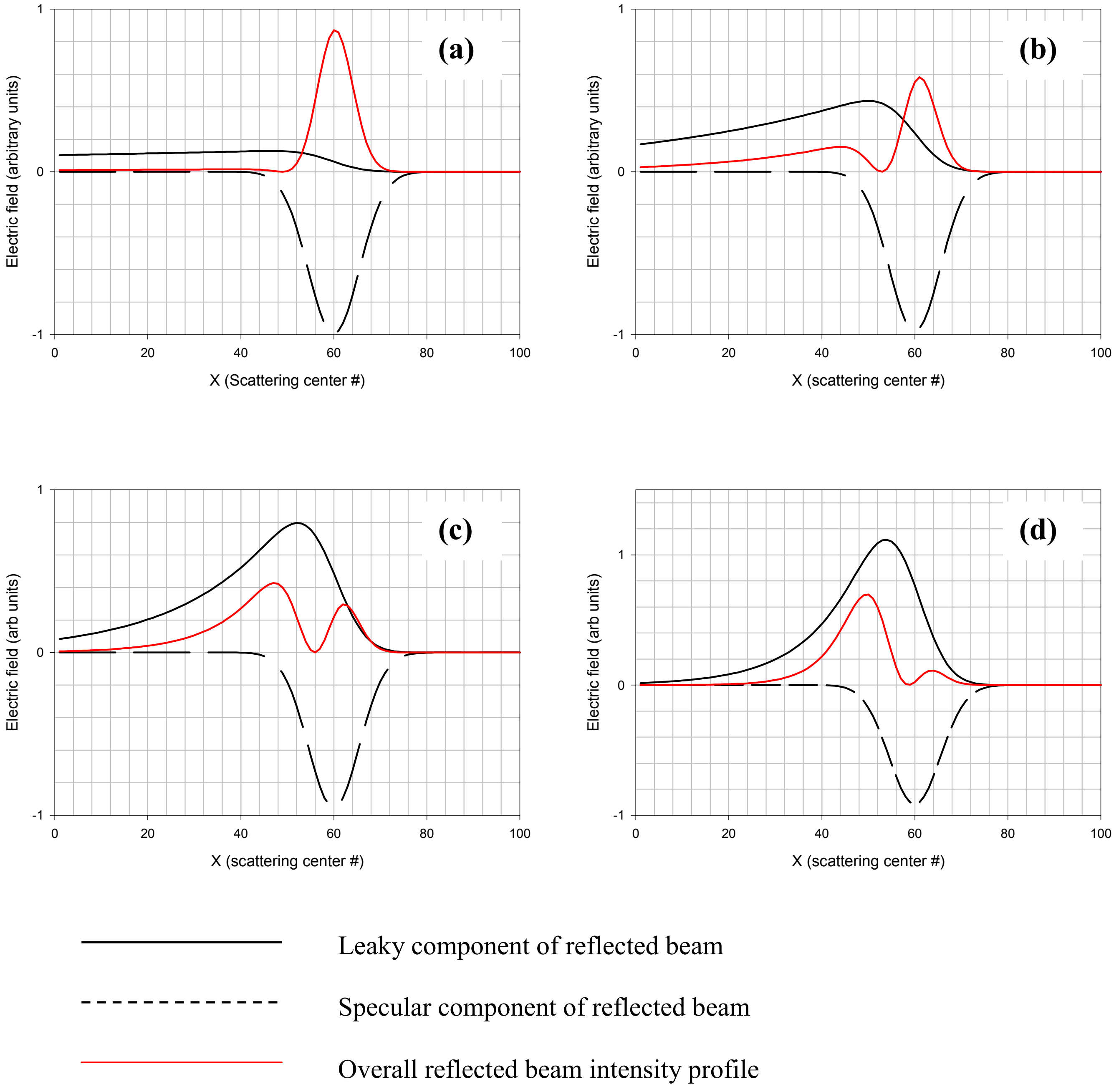

Figure 7.9 Reflected beam profiles including individual components for different input beam to waveguide scattering strength magnitudes of a) 0.1, b) 0.2, c) 0.3 and d) 0.4. A clear increase in the contribution of the leaky wave component as well as a decrease in its width can be seen with increase in scattering strength.

In addition to the increased contribution, it is also apparent the the width of the leaky wave contribution decreases with increase in scattering strength. For uniform strength gratings excited by Gaussian beams, the two contributions are spatially displaced from one another. The only way to get them to overlap is to design a grating with varying strength along its length.

Extending this to the more general case of both transmission and reflection, it can be seen that efficient grating design involves the spatial matching of the different components of reflection and transmission as well as matching their magnitudes and ensuring that that their phases are opposite. This requires significant additional control over the beams.

7.6 Proof of concept design

The previous section showed that it is important to exercise control over the phase and amplitude of the components of the reflected and transmitted beams as well as to match them spatially. The SOI material system provides us with an additional degree of control, due to the presence of a high index contrast interface below the grating. The thickness of the oxide layer may then be used to achieve the the best cover/substrate distribution of the outcoupled beam. In addition to this, the grating etch depth influences the cover/substrate coupling ratio [87]. A combination of appropriate grating etch depth and the correct choice of BOX thickness can thus result in high coupling efficiencies. However, it is important to note that the grating etch depth controls the strength of the grating [54], and therefore controls the coupling beam width. The grating etch depth must thus be designed together with the BOX thickness for a given beam width. In order to do this, it is important to solve Maxwell's equations in the high index contrast grating region so as to get an accurate value for the cover/substrate coupling ratio, as well as the grating strength.

Since SOI wafers come with BOX thicknesses that are either convenient to manufacture, or are designed for best electronic functionality, additional control is necessary to achieve the phases and amplitudes required of the reflected and transmitted field components. Additional control may be realized by adding high index contrast dielectric layers above the grating as shown in Figure 7.10. For a given BOX thickness, the remaining layers may then be designed so as to yield the best value of efficiency. It is important that any such design take the grating scattering into account, especially if the grating is strong. In fact, in a high index contrast system such as SOI, an accurate stack design can be achieved only with complete knowledge of the grating strength and the cover/substrate coupling ratio.

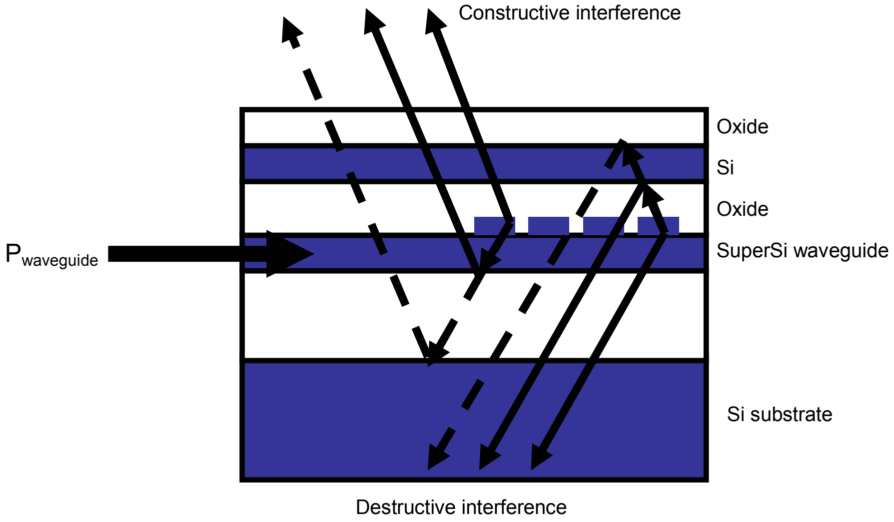

Figure 7.10 The amplitudes and phases of the cover and substrate beams can be controlled by the layers of a high index contrast dielectric stack. The desired ratio can be achieved by the most optimal design of the layer thicknesses.

7.7 Designing the coupler for a given input beam

The previous section illustrated that when a Gaussian beam is incident on a leaky wave structure, the reflection is slightly displaced. We need to achieve a grating design that matches the spatial position of the leaky field component and the reflected field component, apart from matching them in amplitude and phase. The issue is somewhat easier to understand from a reciprocal perspective. A uniform strength grating would produce a beam that varies exponentially along the length of the grating. Since the grating is scattering a percentage of the power as the mode propagates along its length, the maximum power scattered would be at the beginning of the grating when the maximum power is present in the waveguide. The incoming mode from a single mode fiber, however, is close to Gaussian in shape. This results in a decrease in coupling efficiency, to the degree that the spatial mode produced by the grating is mismatched with a Gaussian beam profile [54]. To solve this problem, we need to tailor the strength of the grating along its length. We need the grating to be the weakest at the point where the guided mode contains maximum power, and then increase in strength as the mode gets weaker. Tailoring the strength profile of the grating appropriately can match the grating to a Gaussian beam.

The required strength profile is easily obtained analytically [88]. However, it is clear that the best theoretical strength profile requires the grating strength to start from a value of zero, and to increase very gradually. The improvement in insertion loss is thus limited by how weak the grating can be made. Since planar CMOS processes do not allow the grating to vary in depth along its length, we may use duty cycle to achieve the variation in strength [54]. How weak we can make a grating, therefore depends on how small a duty cycle we can achieve, which in turn depends on the resolution of the lithography being used. In this way, going to smaller minimum feature size technologies would imrove grating efficiency.

Figure 7.11 shows the two components of reflection from the grating surface as a function of position, when the grating strength is tailored along its length to match an incoming Gaussian beam. As can be seen the reflected field component and leaky field component are perfectly matched in position and beam shape. This results in complete cancellation of the reflected beam, achieving highly efficient coupling.

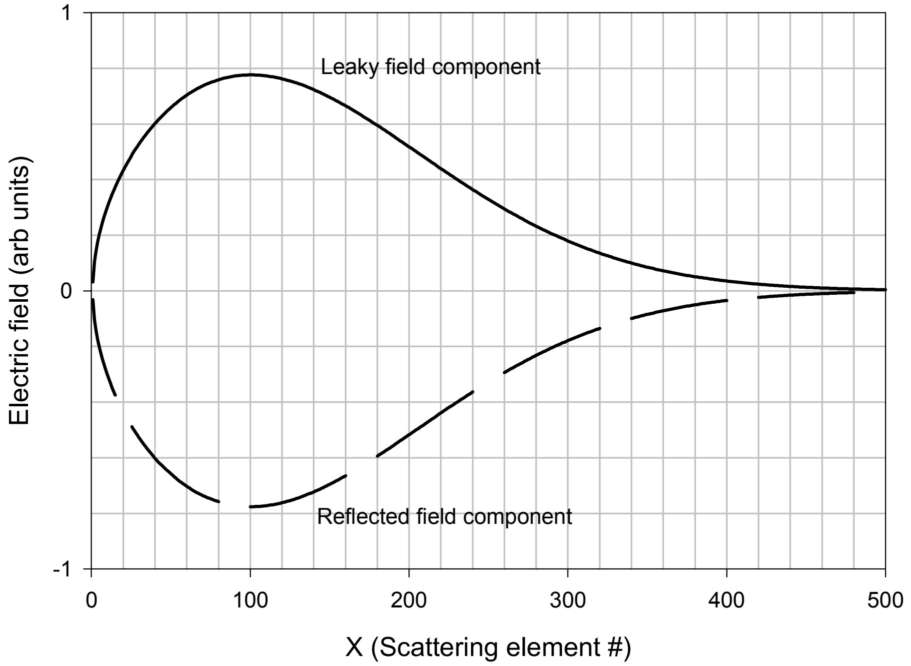

Figure 7.11 Reflected and leaky wave components of a Gaussian beam reflected from a variable strength grating coupler. The grating coupler strength is tailored along its length to match a Gaussian beam. The two components cancel resulting in highly efficient coupling.

7.8 Proof of concept design parameters

The most optimized structure of the stack proposed in 7.7, as well as the design of the grating etch depth, can be obtained only through the complete solution of Maxwell's equations. In order to arrive at a proof-of-concept design of the stack, we try to reduce the influence of the grating on the performance of the stack as much as possible. This means making the grating as shallow and as weak as possible. We may then model the dielectric stack, by modeling the grating as source, and neglect any secondary scattering effects. In practice, this is not the best way to obtain a solution for the following reasons:

- The grating is high index contrast, making it very difficult to obtain a very weak grating, except with uncontrollably shallow etch depths.
- Making a grating very weak increases its length, thus decreasing the coupling bandwidth.
- In practical systems we would wish to couple directly from fiber into the chip, requiring the grating to be designed for the mode width of a single mode fiber.
- The cover/substrate coupling ratio is a function of the grating depth [87]. Neglecting the contribution of the grating and treating it as a source, implicitly assumes no directional preference leading to an additional source of inaccuracy.
- The grating depth, BOX thickness and overlying layer thicknesses, together with the successive scatterings in the grating structure influence the eventual cover/substrate ratio. A properly optimized design optimizes over all these parameters.

We chose a waveguide width of 40 µm, and a grating depth of 40 microns. Lateral guiding is necessary in order to locate the grating at some distance from the edge of the thin film. This prevent scattering off the edge of the sample, and allows for the calibration of waveguide loss. The grating period was chosen to be 540 nm, resulting in a slightly backward incoupling angle for the single TE mode of the thin film waveguide. We chose to use a uniform grating, and compensate experimentally for this, by arranging for a maximum overlap of the input Gaussian beam with the grating's exponential mode. In the best case, the degradation in efficiency from this is only 20.1% [54].

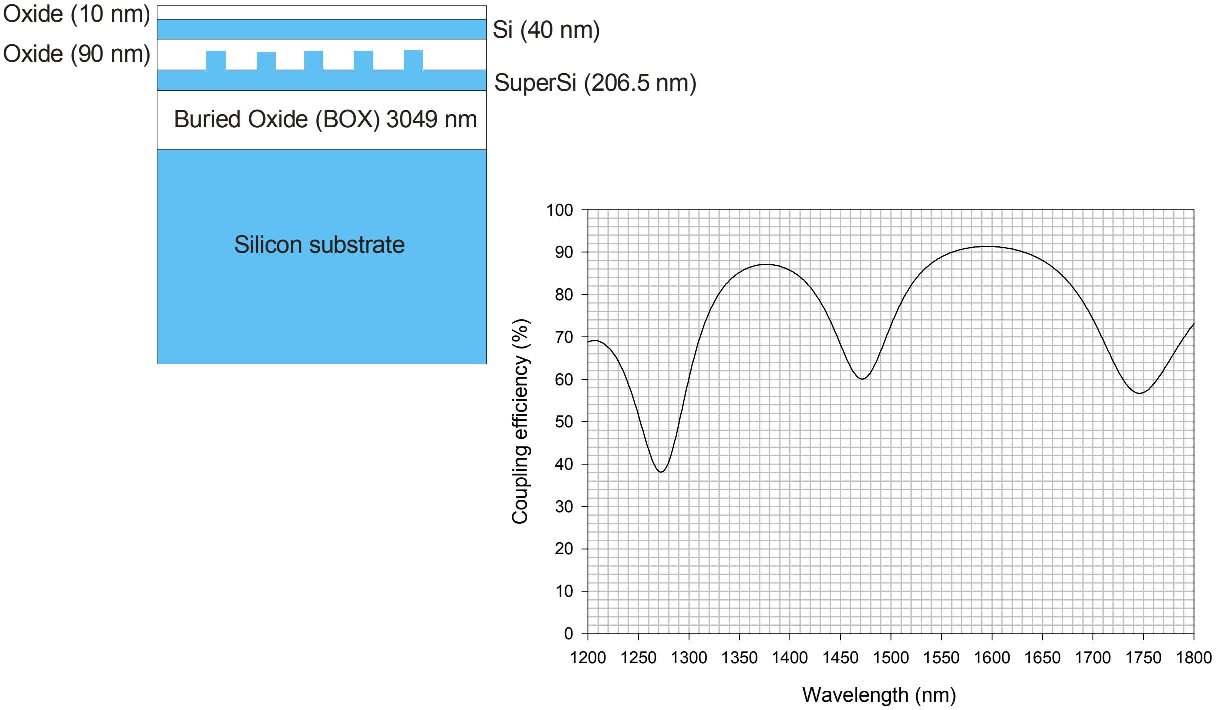

Figure 7.12 (a) The parameters of the high index contrast dielectric stack, and (b) the spectral response obtained by simulating the stack with a 2x2 complex transmission matrix approach. The grating is assumed to be very weak.

The stack above the grating together with the BOX layer was modeling using a 2x2 complex transmission matrix approach as described in [89]. The grating was treated as a sheet of current, thus acting as a source. The stack was designed to maximize the power in the cover region at the expense of the power in the substrate region. It should be noted that this technique is limited in accuracy since it neglects the scattering and coupling that occurs in the grating structure due to multiple reflections. The simulation thus increases in accuracy as the grating gets weaker. Using this assumption, optimization over the thicknesses shown in Figure 7.12(a), yielded the spectral response shown in Figure 7.12(b). The SuperSi and BOX layers were fixed in the commercial material procured from SOITEC, France. If the layers are thin enough, the grating bandwidth is not limited by the layer structure.

7.9 Conclusions

In this chapter, we developed a physical understanding for the source of the transmitted and reflected beams produced by a grating coupler when it is excited with an input beam. We proposed the use of a high index contrast dielectric stack to exercise control over the phases and amplitudes of these beams in order to achieve efficient coupling. Optimization of the stack may be performed together with the BOX thickness and the scattering properties of the grating, to obtain the lowest insertion loss structure.

Chapter 8 Fabrication of waveguide grating couplers

The design of waveguide grating couplers was discussed in Chapter 7. This chapter describes the fabrication of the grating couplers, and the high Δn dielectric stack described in the previous chapter.

Part of the justification for silicon based optoelectronics lies in the superior processing technology and knowledge that we have come to expect from the silicon semiconductor industry. As such, fabrication processes for Si optoelectronic devices need to be compatible with CMOS processing technology. CMOS processes are planar, and therefore preclude any steps that require gray scale masking, angled etching or off-normal deposition. All devices must therefore be planar. In addition, post-processing a CMOS circuit places an upper limit on the temperature that the substrate may be subjected to during fabrication of the optoelectronic device. This limitation comes from the eutectic point of Al and Si, which is approximately 577 C. Raising the wafer to this temperature after metallization would compromise the integrity of the electrical contacts. All the processes described in this chapter, will attempt to conform to the requirements of such low temperature, planar processes.

8.1 The high Δn material system

All devices were fabricated on commercial Silicon-on-Insulator (SOI) substrates procured from SOITEC, France. The SOI was manufactured using the Smart Cut method. The superficial silicon (SuperSi) is acceptor doped (~ 10^{15}), and is thus p-type, but this is not important for the purposes of a purely optical experiment. As is evident from Section

7.4, the most critical parameters of the basic material structure are the SuperSi and BOX thicknesses. The principal requirement is that the SuperSi thickness be such that it supports only a single optical mode at a wavelength of 1.55 microns, and that the BOX layer is thick enough to prevent leakage of that optical mode into the high index Si substrate. The remaining layers can be designed as in Section 7.7, so as to achieve the highest efficiency possible for given thicknesses of SuperSi and BOX layers.

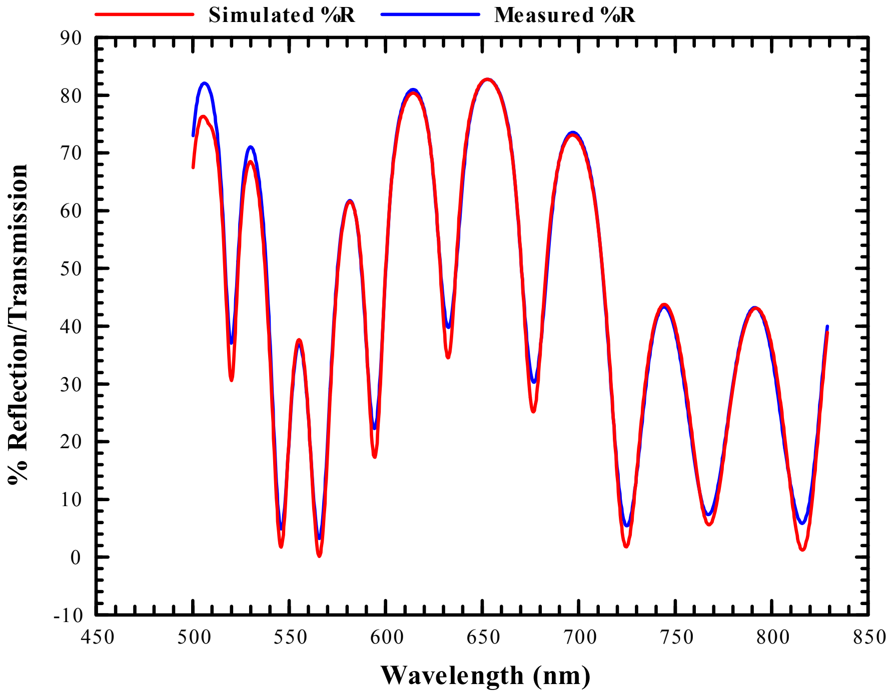

Figure 8.1 Measured and simulated reflectivity vs. wavelength curves for the Silicon-on-Insulator material structure from SOITEC, France. The most closely matched simulated (red) curve corresponds to SuperSi/BOX thicknesses of 206.5/3038.0 nm. The measured (blue) reflection spectrum was obtained from an SCI Filmtek spectrophotometer.

Figure 8.1 shows the reflectivity of the SOI material structure as a function of wavelength at normal incidence obtained from an SCI Filmtek spectrophotometer. The blue curve is a measured reflectance curve at normal incidence. The red curve is a simulated curve for SOI using standard NK material coefficients. The most closely matched simulated curve corresponds to SuperSi/BOX dimensions of 206.5/3038.0 nm.

8.2 Waveguide fabrication

Waveguides are defined in an iron oxide mask and patterned into AZ 5214 positive resist using contact ultraviolet photolithography. The pattern was transferred from the AZ 5214 into the SuperSi using a reactive ion etch (RIE). The BOX acts as a stop-etch layer. Since the superficial silicon is of high quality, the waveguide loss coefficient is dominated by scattering due to sidewall roughness. Care must be taken to obtain smooth and vertical etch profiles in order to reduce waveguide loss in practical devices, however it is not critical for the purposes of this experiment.

Waveguide loss is easily factored out of the experiment by fabricating waveguides of different lengths. In fact, a moderately high loss (15-20 dB/cm) waveguide actually assists the experiment by reducing the coupling between the waveguide edge and the grating coupler device, thus eliminating the need for any further engineering or accounting. This will be discussed further in Chapter 9. Practically, waveguide loss can be reduced by techniques such as oxidation smoothing [90] and hydrogen annealing [91].

Figure 8.2(a) shows a top view schematic of the waveguides fabricated in the superficial silicon. One end of the waveguide is cleaved so as to give us an optical interface. The waveguide thickness exactly matched the superficial silicon thickness and the widths were set at 40 microns. Figure 8.2(b) shows a scanning electron micrograph of one of the waveguides.

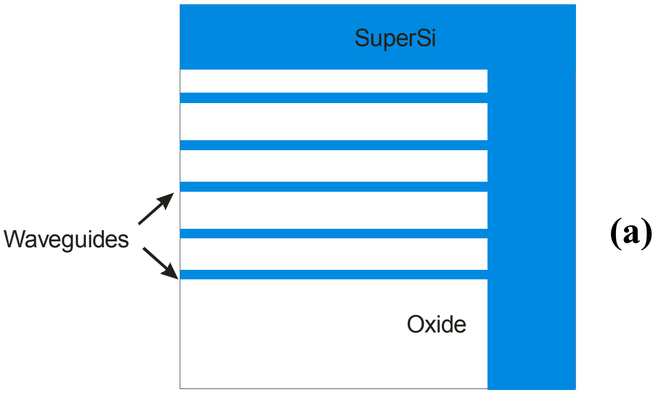

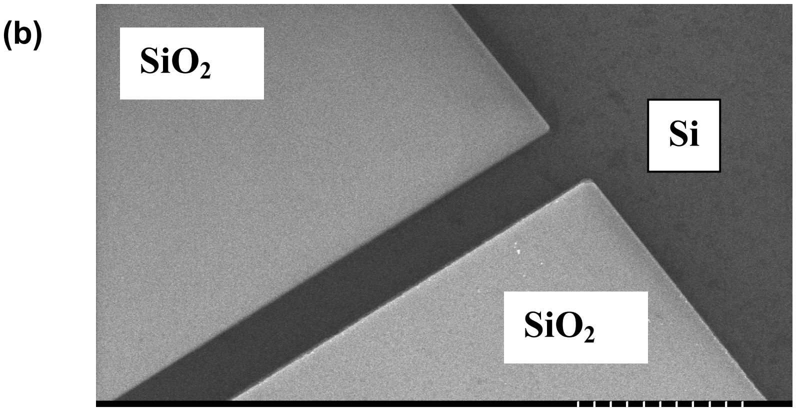

Figure 8.2(a) Top view schematic of waveguides fabricated on SOI chip and b) SEM image of one of the waveguides. The waveguides are 40 μm wide.

8.3 Grating Fabrication

Gratings may be fabricated in two ways. The grating may be etched directly into the silicon waveguide as shown in Fig. 8.3(a), or it may be housed in an oxide layer deposited right above the waveguide, as shown in Fig. 8.3(b). The first choice, while resulting in a better grating, requires very careful calibration and control of the etch rate. A high degree of etch uniformity is also necessary over the scale of a single chip.

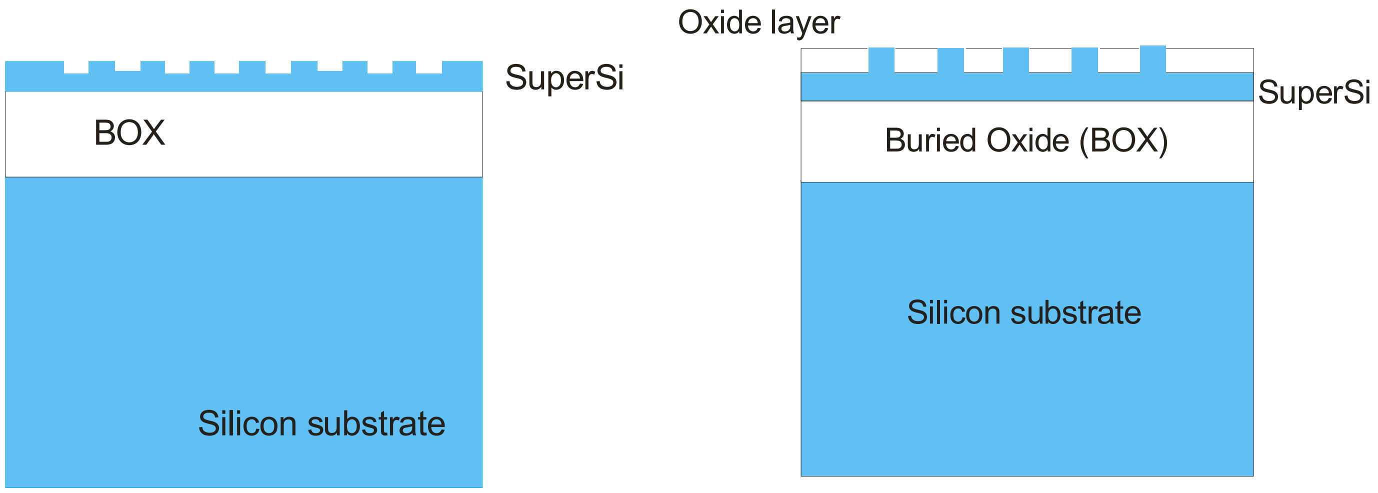

(a) **(b)**

Fig. 8.3 Gratings may be fabricated by a) etching directly into the silicon waveguide or b) by housing them in an oxide layer deposited right above the waveguide.

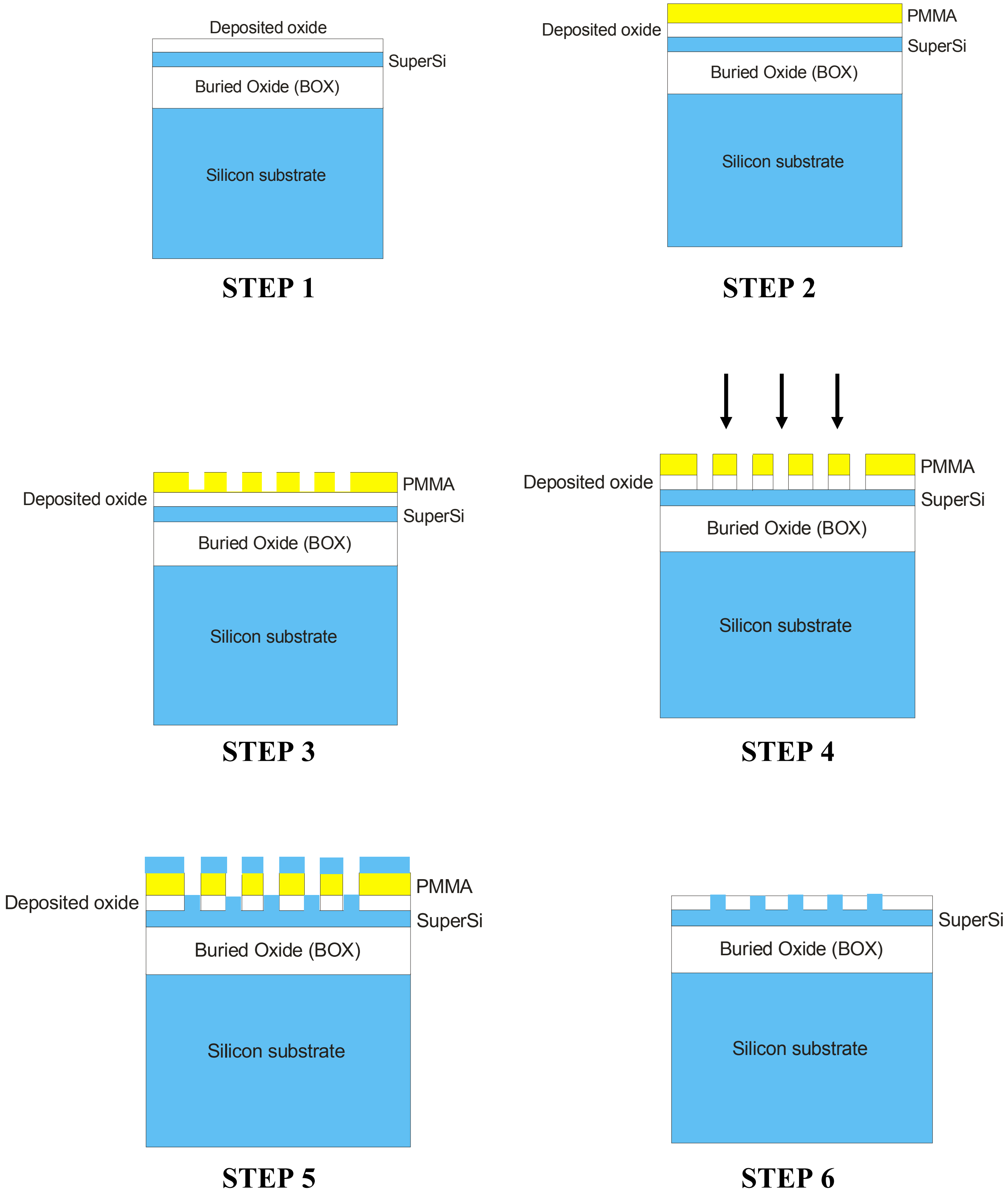

Figure 8.4 Process flow for the fabrication of grating couplers

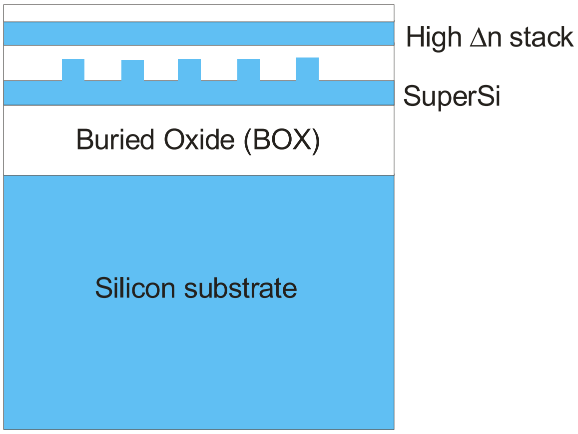

STEPS 7, 8 & 9

Figure 8.4 cont. Process flow for the fabrication of grating couplers

Excessively deep etches will strongly perturb the effective index of the waveguide, thus requiring extremely narrow in-coupling beam widths as was explained in Chapter 7.

The other option is to fabricate the grating in an oxide layer deposited immediately above the superficial silicon waveguide. This allows superior control over the thickness of the grating, by controlling the thickness of the deposited oxide.

We adopt the second approach to fabricating the grating. The process steps are illustrated in Figure 8.4 and described in the paragraphs that follow.

Step 1: A thin oxide layer is deposited directly above the SuperSi layer. We used an electron beam evaporation process, with a calibrated endpoint to achieve a pre-determined thickness of oxide.

Step 2: A thin film of poly methyl methacrylate (PMMA), or electron beam resist is spun on the sample.

Step 3: The PMMA is patterned to define the grating structure. The grating is aligned to the already fabricated waveguides using a laser interferometric stage and already deposited Titanium/gold alignment marks. While we used electron beam lithography in order to obtain the sub-micrometric patterns necessary to form the grating, the dimensions of the device are well within the reach of state of the art photolithographic techniques.

Step 4: The pattern is transferred from the PMMA into the oxide using a CHF_3 reactive ion etch. Since PMMA is a soft plastic, pattern transfer from PMMA into oxide with high fidelity is difficult, especially for sub-micron patterns. A high fidelity pattern transfer is achieved by using lower process and base pressures, as well as a pure CHF_3 RIE. When a lower process and base pressure is used, there is less oxygen in the system. Since oxygen etches organic material, lowering the base pressure reduces the PMMA etching rate, greatly improving selectivity. In addition to that, CHF_3 reacts with PMMA during the etch, forming a fluoropolymer which hardens the PMMA, thus improving the selectivity further.

Using a pure CHF_3 etch and low pressures slows down the etch rate considerably. Figure 8.5 shows an etch rate calibration for the oxide etch used to transfer the grating pattern. This technique has been used with great success for the transfer of photonic crystal nanopatterns into oxide over III-V semiconductors. In the case of oxide over Silicon, further tweaking of the etch parameters are required in order to obtain a high enough selectivity for the etch to stop at the SuperSi layer [92].

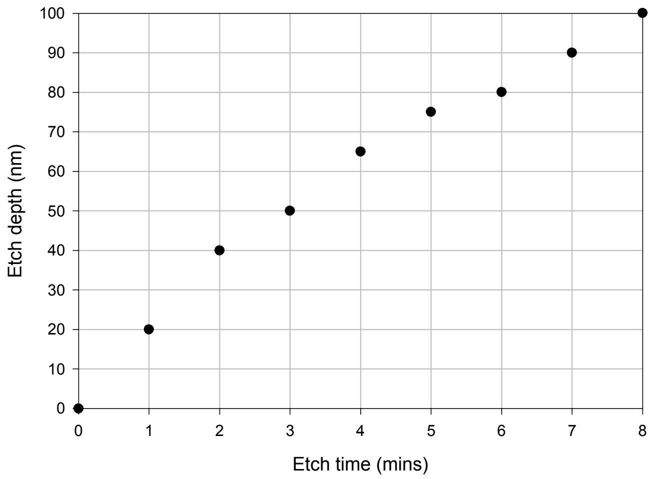

Figure 8.5 Reactive ion CHF_3 oxide etch rate calibration. It is important to keep the oxygen content of the plasma low in order to ensure high selectivity over PMMA for proper pattern transfer.

Step 5: The spaces in the oxide and PMMA are backfilled with electron beam evaporated silicon. This is necessary in order to planarize the device for the deposition of subsequent layers. This is the technique adopted in the lab, to work around the poor accuracy of chemical mechanical polishing (CMP) available, but planarization can be achieved commercially with highly accurate polishing. State of the art CMPs now achieve precision stops of 1 nm, which is largely a function of the material being polished and the endpoint detection method used [93].

Step 6: The PMMA is lifted-off with heated acetone. Figure 8.6(a) shows an SEM image of the grating aligned with the waveguides. Figure 8.6(b) shows a close up SEM micrograph of the planarized grating. The period is 0.54 microns.

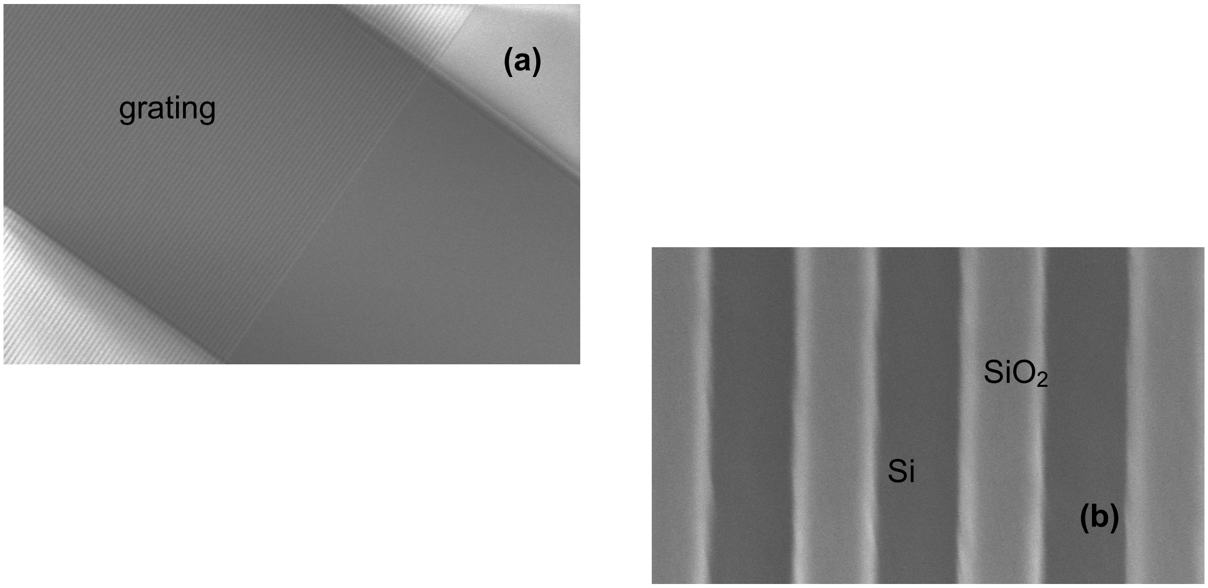

Figure 8.6 SEM micrographs of fabricated gratings. a) The grating aligned with the waveguide and b) close up of grating structure. The period is 0.54 μm. The waveguide is 40 μm wide.

Step 7: AZ 5214 photoresist is spun onto the sample, and squares are patterned into the photoresist right above the gratings. Alignment is performed visually. This step is necessary in order to ensure that the high index contrast stack is restricted to the area directly above the grating, so that it does not alter the waveguide properties significantly.

Step 8: The high index contrast dielectric stack is deposited using electron beam evaporation.

Step 9: The photoresist is lifted off with heated acetone, yielding the waveguide aligned grating couplers with the high index contrast stack above them.

8.4 Conclusions

In this chapter, we described a process for the fabrication of waveguide aligned grating couplers. We also described a process for the addition of a high index contrast dielectric stack directly above the grating coupler. Such devices lend themselves to easy fabrication with CMOS technology.

Chapter 9 Characterization of waveguide grating couplers

This chapter describes the experimental characterization of the waveguide grating couplers that were fabricated as described in the previous chapter. The aim of the experiment is to measure the insertion loss of the grating coupler embedded in the high index contrast stack. While designing the experiment, we must choose between an out-coupling configuration as shown in Figure 9.1(a), or an in-coupling configuration as shown in Figure 9.1(b). Out-coupling experiments [68,87] measure the ratio of the powers coupled into the cover and substrate in order to determine overall coupling efficiency. The insertion loss, in such experiments, can be estimated by using:

$$\mathrm{IL} = 10 \log \frac{P\mathrm{cov}er + Psubstrate}{Psubstrate}$$

Positive values of IL indicate a loss. This measure of insertion loss, assumes that any inefficiency in the grating arises solely from the existence of an outcoupled substrate mode. It neglects any parasitic scattering effects, or the effect of waveguide loss, and is therefore an idealized value of the insertion loss.

Intuition suggests that an outcoupling measurement should be easier, on account of the much larger phase space available for the light to couple out to. However, the out-coupling measurement requires the prior existence of a guided mode. End-fire coupling may be used to excite the guided mode, however this somewhat offsets the ease of the

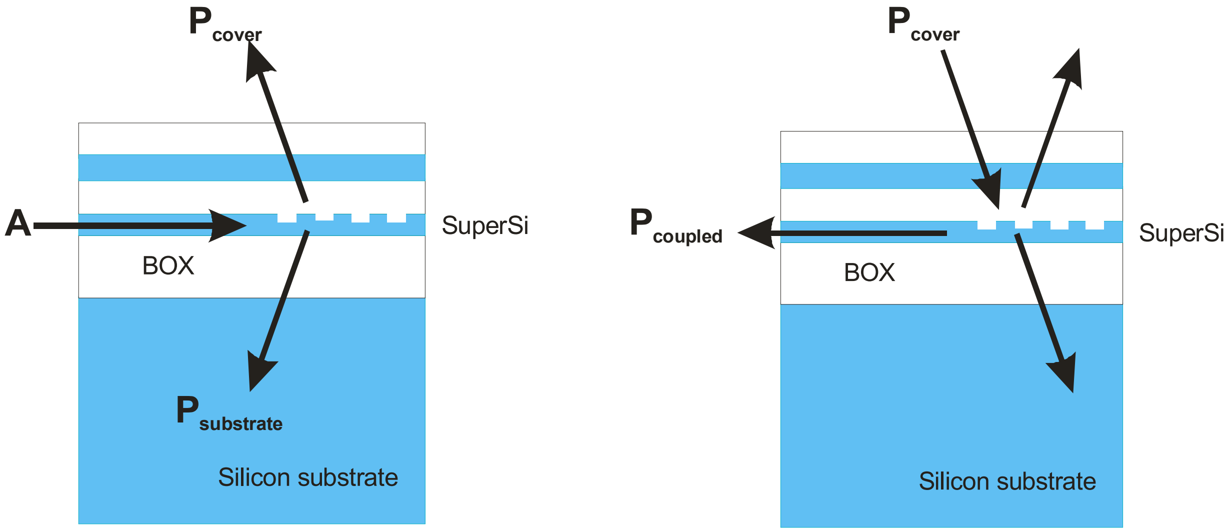

(a) (b)

Figure 9.1 Grating configurations for efficiency measurement. a) Out-coupling measurement depends on the existence of a guided mode in the waveguide, and underestimates the insertion loss. b) In-coupling measurements are experimentally more involved, but yield a more direct and accurate value of the insertion loss.

experiment on account of its low efficiency. A second grating may be used [94], however this adds more unknowns to the experiment. We choose to do an in-coupling measurement, since it yields a more direct result, and is reflective of actual device performance. All experiments are performed in the optical C-band around 1.55 µm.

9.1 Experimental parameters

As mentioned in Chapter 7, it is important to be able to experimentally control and vary multiple parameters, in order to find the point of highest efficiency in the parameter space. This degree of experimental control is necessary to compensate for fabrication tolerances as well as the lack of knowledge of the exact microscopic coupling strength. Experimental control over the following parameters is necessary:

1. *Wavelength*

   The wavelength needs to be varied to find the exact momentum matched point of the air mode to the waveguide mode. It is also important to determine the grating's spectral response and bandwidth.

2. *Incident beam angle*

   The incident beam angle also needs to be varied to find the moment matched point. Fabrication inaccuracies, as well as inaccuracies in the experimental setup require control over this angle in order to arrive at the optimum coupling arrangement.

3. *Incident beam polarization.*

   The grating is designed for a single polarization, making control over the incident polarization necessary in order to ensure optimum coupling.

4. *Incident beam width*

   The incident beam width is roughly inversely proportional to the grating strength as demonstrated in section 9. To compensate for the lack of knowledge of the grating strength, control over the incident beam width is required. The shallow gratings fabricated, as well as the waveguide width we have chosen, suggest that control of the beamwidth is important in the vicinity of 40 microns.

5. *Lateral alignment of the beam with the grating.*

   As shown in section 7.7, the coupling efficiency is a strong function of the lateral position of the beam. In addition, the waveguide is multimode in the plane of the Si thin film, requiring careful alignment in order to ensure maximum overlap of the waveguide mode with the incoming Guassian mode.

9.2 Experimental Setup

A top view schematic of the fabricated sample layout is shown in Figure 9.2. Gratings are fabricated at different lengths from a cleaved facet. The different waveguide lengths allow for the calibration of waveguide loss. Coupling into the waveguides may be experimentally established in two ways. One way is to measure a dip in the beam reflected from or transmitted through the grating structure. While this will establish the coupling phenomenon, it lacks enough information to provide us with a number for the efficiency, unless both the transmitted and reflected beams are measured simultaneously. Furthermore, unless the substrate is backside polished and diffraction in the substrate is properly accounted for, results obtained from such a measurement will underestimate the insertion loss arising from such a coupler.

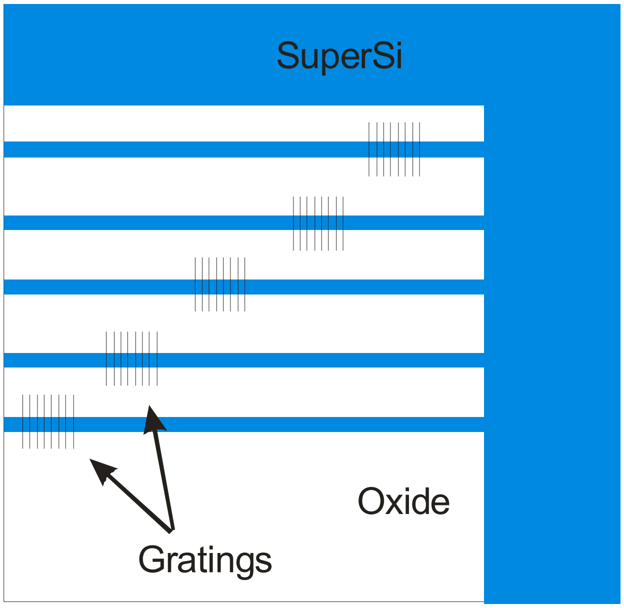

Figure 9.2 Top view schematic of the sample. Gratings are fabricated at different distances from a cleaved output facet. The different waveguide lengths allow for waveguide loss calibration. Light may be collected at the output facet giving a direct measurement of the power in the waveguide.

The second way, and the one we adopt, is to couple light into the waveguide using the grating, and to measure the light that is out-coupled from the cleaved waveguide facet. Insertion loss may be determined by considering the input and output powers and accounting for the various losses along the way. Coupling is established by imaging the waveguide edge and selecting the light in the mode with a spatial filter. Additionally, coupling may be established by a high degree of sensitivity to the input polarization, as well as a comparison between on-device and off-device illumination. Figure 9.3 shows a diagram and close-up photograph of the experimental setup. Light is coupled into fiber from a tunable external cavity laser diode tunable between 1510 and 1590 nm. The light

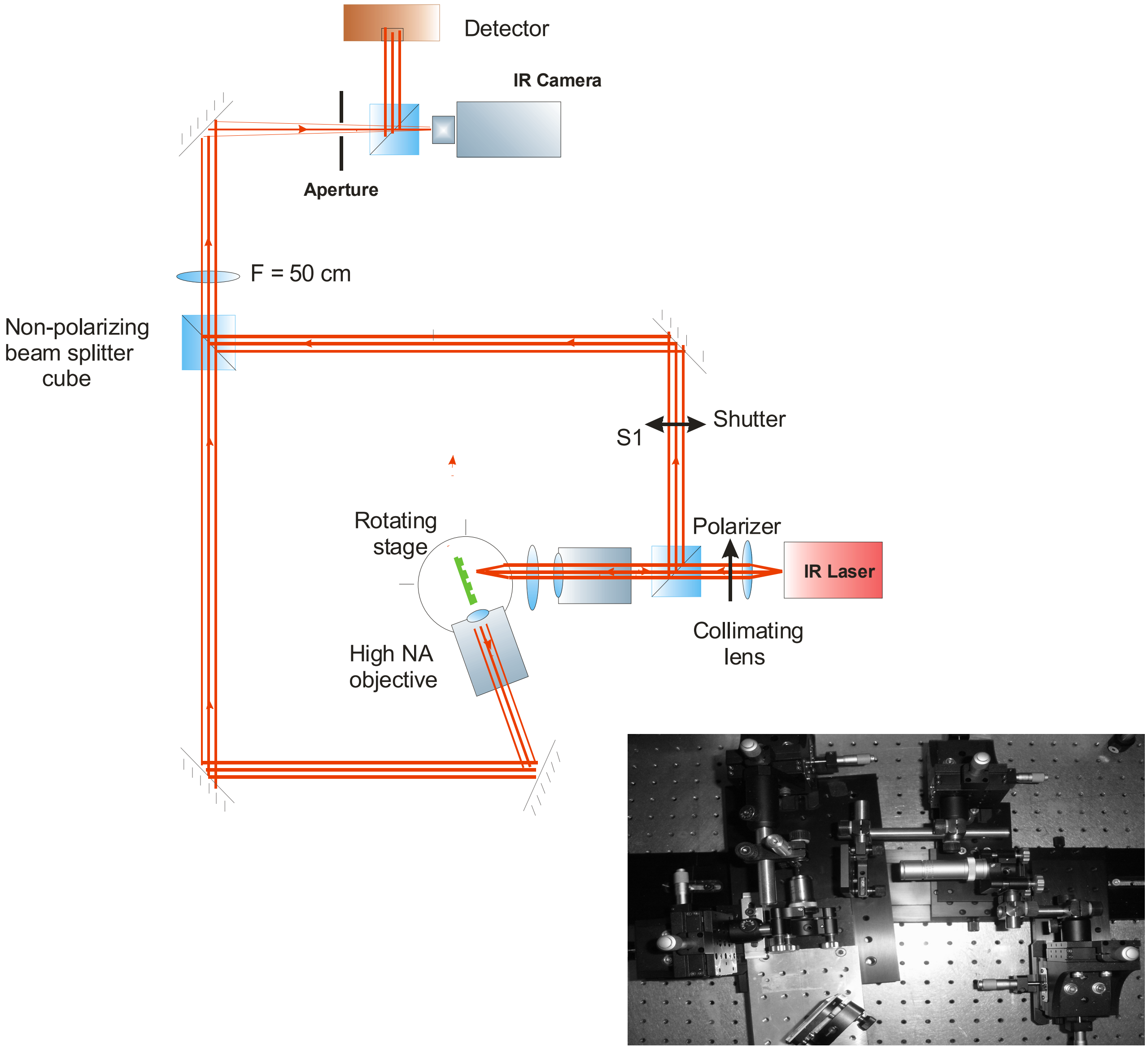

Figure 9.3 Diagram of experimental setup. Beam width adjustment is accomplished by a microscope objective and an aspheric lens. The photograph shows the rotating stage and the beam width adjustment optics, together with the collection optics.

is passed through a polarization controller and a collimating assembly. This is followed by a polarizer and a beam width adjustment assembly consisting of a microscope objective and an aspheric lens. Different beam widths are achieved through the use of different aspheric lenses and by varying the distances between the MO, lens and sample. All optics are mounted on three axis stages and include pitch and yaw adjustment. All the stages are mounted on a rail aligned with the optical axis, allowing maximum range while adjusting relative distances. The beam width is measured by replacing the sample with a scanning piezoelectric knife edge connected to a ramp generator and differentiating circuit, commercially obtained from ThorLabs Inc. The beam profile is observable on an oscilloscope, and may also be used to fine tune the optical system.

The sample is mounted on a rotating stage, and has six degrees of freedom. The collection assembly consists of a high numerical aperture microscope objective, and a dual mirror system. The microscope objective and one mirror are mounted on the rotating stage along with the sample, in order to facilitate easy alignment of the collection assembly. The waveguide end is imaged onto a lead oxy-sulphide camera through a pinhole which spatially filters any parasitic optical signal.

All optics are initially aligned using a visible HeNe laser beam, which is then replaced by the 1550 nm laser. Alignment to the grating couplers is done visually, using the scattering obtained when the HeNe laser falls on the stack and grating structure. Finer alignment is performed by maximizing the power outcoupled from the waveguide.

The insertion loss of the grating coupler is determined by the following equation:

$$IL = P_{in} - P_{opt} - P_{waveguide} - P_{reflection} - P_{collection} - P_{out} \tag{9.1}$$

Where, the symbols used are defined as follows:

P_{in} is the input optical power.

P_{opt} is the loss in the optical system leading up to the grating coupler, which is measured before the experiment.

$P_{waveguide}$ is the waveguide loss, which is measured as described in the next section.

$P_{reflection}$ is due to Fresnel reflection at the silicon/air interface at the waveguide facet and is assumed to be roughly 30% or 1.54 dB

$P_{collection}$ is the loss in the collection optics, also evaluated before the experiment. It has a value of 2 dB.

P_{out} is the collected and measured optical power from the waveguide facet.

When P_{in} and P_{out} are expressed in dBm, and P_{opt}, $P_{waveguide}$, $P_{reflection}$ and $P_{collection}$ are expressed in dB, we get a value for insertion loss (IL), in units of dB.

9.3 Experimental Results and Discussion

After aligning with the grating, we carefully optimized the output power, by fine tuning the alignment and the angle. Since each grating is a different distance from the waveguide edge, repeating this experiment for the different gratings yields a plot of output power vs. waveguide length as shown in Figure 9.4.

We may rewrite Equation 9.1 as

$$P_{out} = C - P_{waveguide}$$

since IL, P_{in}, P_{opt}, $P_{reflection}$ and $P_{collection}$ are all constant for constant input power.

Now $P_{waveguide} = \alpha L$

If L is in cm, α is the loss coefficient of the waveguide in dB/cm

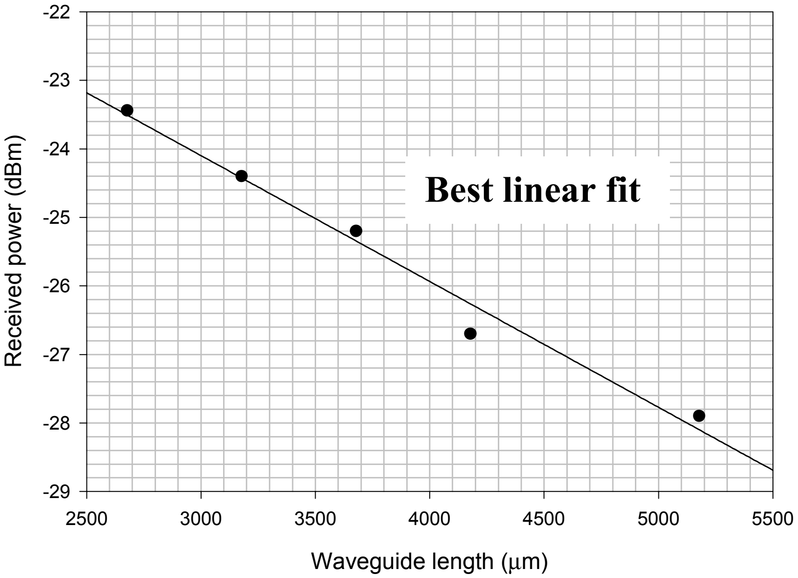

Figure 9.4 Waveguide loss calibration. The best linear fit to the received power for different waveguide lengths, yields an extracted waveguide loss of 18.33 dB/cm. Gratings on waveguides of different lengths are assumed to be equally efficient.

The negative slope of the best linear fit to the data yields a value for $\alpha = 18.33$ dB/cm. The waveguide loss measurement assumes that the insertion loss does not vary across the different gratings on the same chip, and it is therefore very important to perform this measurement before capping the gratings with the high index contrast stack. We then cap the gratings as described in Steps 7 to 9 of Section 8.3, and measure the insertion loss as a function of wavelength. The waveguide loss α, as determined from our previous measurement is applied as in Equation 9.1.

. For the wavelength test, once the output power is maximized for a given alignment, only the wavelength and polarization are varied to maximize the output power at a given wavelength. All losses are accounted for as in Equation 9.1.

Figure 9.4 shows a graph of insertion loss vs. wavelength for the capped structure. The device shows a minimum insertion loss of 5.9 dB at a wavelength of 1526.5 nm. The polarization dependent loss (PDL) of the device is measured by varying the input polarization for minimum output power. The PDL is in excess of 35 dB. The 3 dB bandwidth of the device is approximately 8 nm, but is due to the use of a long grating and the large beam width. Realizing a higher coupling bandwidth will require the use of shorter, deeper and stronger gratings which will require more comprehensive electromagnetic simulations.

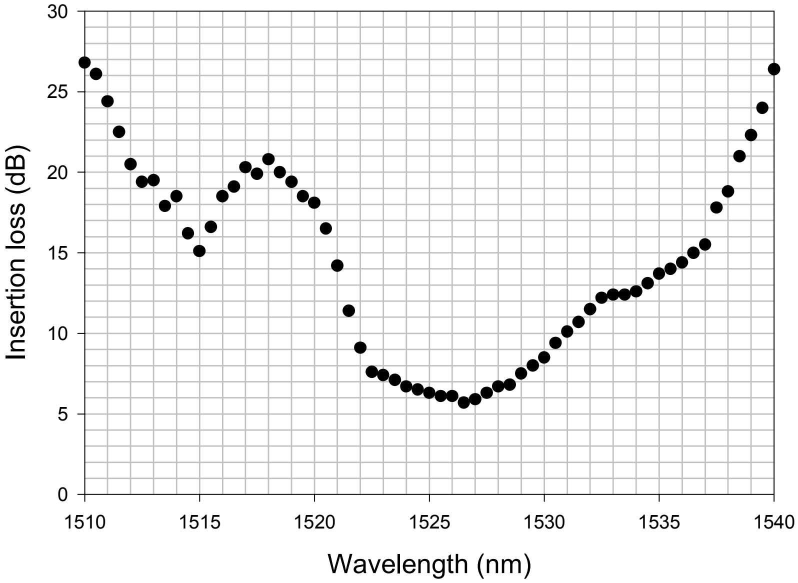

Figure 9.5 Graph of insertion loss vs. wavelength for embedded grating coupler

Figure 9.5 shows a variation in the insertion loss at 1526.5 nm as a function of a deviation from the optimum incident beam angle. Since both the angle and the wavelength determine the appropriate phase matching condition, any drift in the design wavelength of practical gratings may be compensated within limits by varying the input angle.

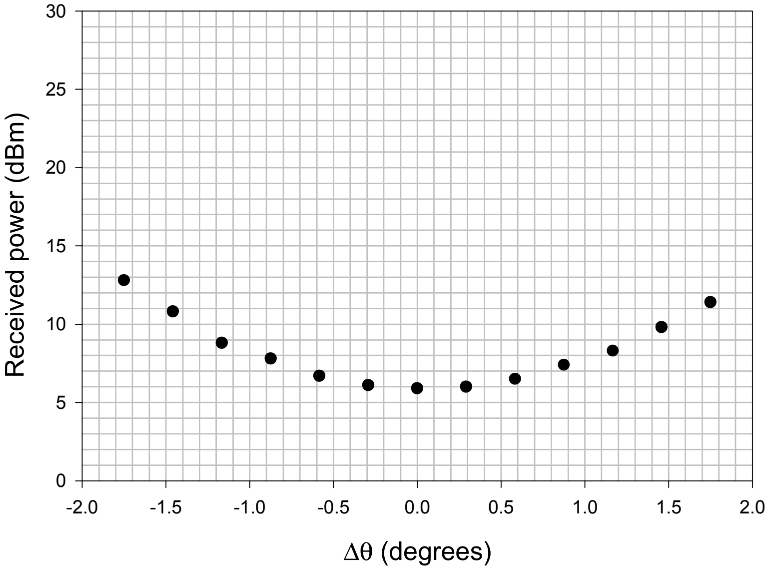

Figure 9.6 Insertion loss vs. deviation from optimum angle.

Figure 9.6 shows the insertion loss as a function of the positional deviation along an axis parallel to the grating grooves. Since the beam is moving equally off the grating in both directions the curve is symmetrical.

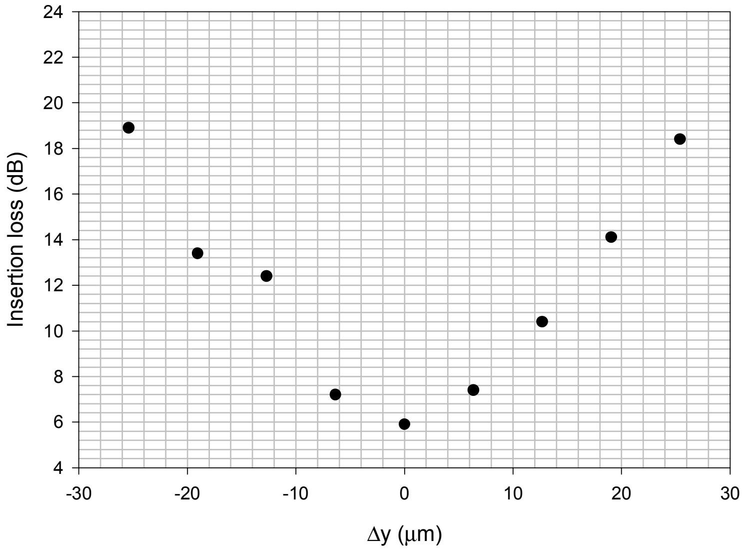

Figure 9.7 Insertion loss vs. deviation from optimum position in a direction parallel to the grating grooves

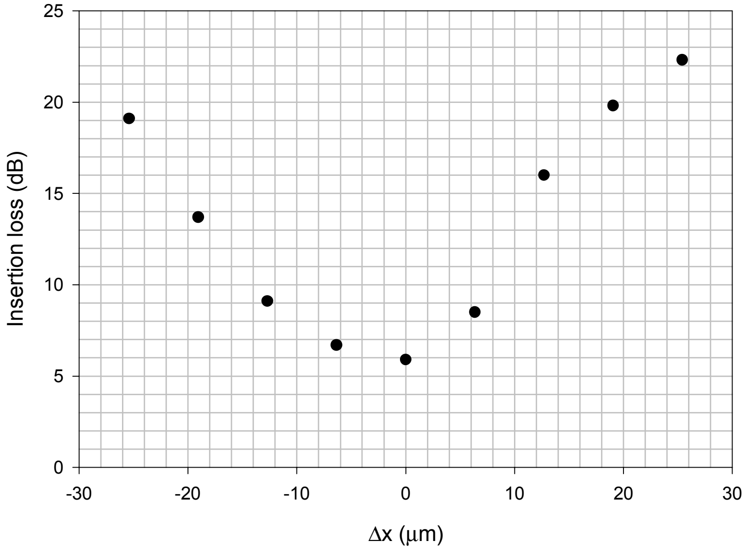

Figure 9.8 Insertion loss vs. deviation from optimum position in a direction perpendicular to the grating grooves

Figure 9.7 shows a plot of insertion loss vs. the deviation in a direction perpendicular to the grating grooves. Clearly the situation for which the beam moves on to the grating is better than the situation when the beam begins to move off the grating, explaining the asymmetry of the curve. Moving on the grating causes a spatial disturbance in the position of the two components of the reflected and transmitted beams, resulting in less efficient cancellation as discussed in Chapter 7.

9.4 Conclusions

In this chapter, we demonstrated a reduced insertion loss grating coupler, embedded in a high index contrast dielectric stack. The coupling bandwidth is limited by the large beam width used. While an improvement may be made by reducing the beam width, the coupling bandwidth will ultimately be limited by the beam width of single mode fiber. The efficiency itself is limited by the lack of knowledge of the exact scattering properties of the grating, the approximations used in the design of the dielectric stack, the spatial overlap with the waveguide mode and the loss in the amorphous silicon and in the waveguide.

While the experiment suggests that the efficiency of a grating coupler can be enhanced by embedding it in an appropriately designed stack, the design of the stack itself is a non-trivial problem. For the purposes of this experiment, the grating was designed to be very shallow, and its presence was neglected while designing the stack, however it is important to note that any attempt to design the stack for best efficiency, must necessarily take into account the scattering properties of the high index contrast grating, especially those gratings designed for fiber coupling. Failure to do so will lead to an inefficient design, or erroneous conclusions regarding the properties of the stack. Furthermore, it is important to note that given a certain SOI wafer, with a pre-established BOX thickness, it may be possible to enhance efficiency with an overlying stack, however this may not be true for all BOX thicknesses. There exist certain BOX thicknesses, for which the addition of additional layers can only serve to degrade the efficiency.

The grating coupler is a very complex and design intensive device, even in its single polarization form. For efficient performance, a complete solution of Maxwell's equations is necessary in the grating region, in order to obtain the exact scattering coefficients of the coupler, together with the exact knowledge of the desired mode shape and the mode propagation constant. This can then be used to obtain the most favorable design of the BOX and overlying layer structure.

Chapter 10 Conclusions

In this project, we first reviewed the previous work on RF photonic single sideband transmission systems. The fact that single sideband occupies only half the bandwidth on only one side of the optical carrier, prompted Smith, Novak and Ahmed [2] to proposed this as an ideal system to eliminate dispersion penalties present in the long distance transmission of RF sub-carrier multiplexed systems. Soon after this was proposed it caught the attention of a large number of systems researchers who used this concept to implement various functions right from high bit-rate systems [25], to quantum cryptographic links [95].

The growth of Internet usage and the proliferation of number new network applications has revolutionized the field of optical communications. Every Hertz available in optical fibers is now valuable for carrying network traffic. The prevailing trend for capacity optical communications is dense WDM technology. However, at the beginning of this project dense WDM was not very dense. State of the art WDM had 10 Gb/s channels spaced 100 GHz apart, which was roughly 10% spectral utilization. The next generation of WDM systems is no more than 2X better than this.

SSB signals seemed to offer a solution to this problem. However as we showed in Chapter 2, it is not possible to pack these signals close together owing to the poor quality of the differentiating optical filters. It turns out that the penalty due to this in terms of spectral efficiency is quite large. Even though tremendous effort is being invested in optical filters, the roll-off is yet to reach electrical standards.

In this project, we proposed a tandem single sideband system to counter this problem. Tandem single sideband involves the transmission of both sidebands, but with different data. In this way, the spacing between the optical carriers is doubled without a compromise in spectral efficiency. In addition tandem single sideband systems inherit all the dispersion related advantages of pure SSB systems. In Chapter 3, we demonstrated that a single sideband modulator such as the one proposed in [2] could be modified with appropriate electrical connections to function as a tandem single sideband modulator. We used a coarse optical filter to distinguish between the sidebands, and showed that the two sidebands were carrying different data. We also tested the susceptibility of the modulation process to imperfections in the microwave components used. We showed that the modulator is fairly robust with respect to phase and RF power differences between the two electrodes and that the bias could be used to compensate for any inter-sideband cross-talk caused by these ill-effects.

Despite the apparent advantages of tandem single sideband, in order for it to be successful as a way of increasing spectral efficiency we still needed a more intelligent receiver scheme. A form of coherent detection seemed to be necessary, since we wished to pick signals out of a very crowded spectrum without the use of a sharp optical filter. Coherent detection requires the use of a local oscillator, which requires complicated phase locking and polarization tracking in the optical domain. As a solution to this problem, in Chapter 4, we demonstrated a tandem single sideband receiver using optical heterodyne detection without the need for an optical local oscillator. A dual-electrode modulator such as the one used in the transmitter was used to coherently frequency shift the TSSB spectrum so that it could be heterodyned against the original optical carrier. Such remote heterodyne detection has been done before [96] with promising results, but to our knowledge it had never been implemented along with a frequency shift. While the receiver enabled us to receive a single sideband from a crowded TSSB spectrum by achieving heterodyne detection without an optical local oscillator, the spectral efficiency was still limited by the bandpass nature of the microwave components used. The disadvantages of the design were that it required a narrow and sharp Fiber Fabry Perot optical filter to eliminate the up-shifted carrier in order to prevent it from heterodyning with the original sidebands and causing interference. It also used an expensive active component to differentiate between the sidebands.

While single sideband and tandem single sideband modulation eliminates the dispersion penalty caused by the phase walk-off between the two sidebands, it is prone to phase noise caused by chromatic dispersion induced phase decorrelation. The chromatic dispersion that occurs in the narrowband signal on one side of the optical carrie, however, can easily be compensated for in the electrical domain since the detection is coherent [25].

In Chapter 5, we showed how the dual-electrode modulator connected in the configuration we suggested in Chapters 3 and 4, could be used to accomplish a number of RF functions in the optical domain such as frequency doubling, spectral inversion as well as frequency translation, all without the need for an optical local oscillator. We also showed how our design could be used to implement a direct sequence optical CDMA system. Optical CDMA systems have up to now depended on optical orthogonal codes, since full code orthogonality was not possible owing to the unipolar nature of the optical intensity. However in ours system since the code selection occurs before photodetection, the bipolar nature of the optical field is exploited allowing full code orthogonality. In addition, the spectral separation that occurs due to the coherent frequency shift, reduces cumulative shot noise and beat noise, that are caused by signals from within the same bandwidth falling on a photodetector simultaneously. We show how such a system could be used in a high granularity actively demultiplexed transmission system consisting of a number of low bit rate spread spectrum encoded channels. The scheme we described could also be used to carry direct sequency encoded microwave CDMA channels over fiber optic links with the ability to demultiplex them in the optical domain.

Conventional WDM has been established as the best way of multiplexing different channels onto optical fibers. The proposals in this thesis do not in any way attempt to contest this. However, if employed correctly they can be used to increase the granularity and hence the network layer capabilities of a WDM system. In order for most of these suggestions to become practical there needs to be a low cost way of implementing these designs. Future progress in optical integration may make components such as the ones required in this project much cheaper and easier to use, thus opening the road to more sophisticated techniques based on the ones in this report. The ideas contained in this report may also be adapted to the field of fiber-wireless networks especially for applications such as remote RF oscillator delivery and other RF operations as shown in Chapter 5. The fact that DE-MZMs demonstrate great potential for integration suggest that in the long term such devices may be used for active demultiplexing in schemes such as those discussed in 5.4 or other similar schemes.

It remains to be seen whether the total throughput of an optical SCM QAM tandem single sideband system would be able to better the trunking capacities of today. The need to pack more and more RF channels onto a single wavelength, thus increasing the modulation depth would call for much better, linearized modulators. A proper estimation of the capacity however, would require a more careful study of the dispersion effects on RF photonic signals. Since a great deal of optical power would need to be put into the fiber, it is important to realize the effect of fiber non-linearities on an RF photonic signal as well as on multiple densely packed signals of this kind.

The receiver architectures proposed in Chapters 1 to 5 required highly linear, high performance active components such as efficient modulators and photodetectors. Such devices make the cost and complexity of such receiver architectures prohibitive. Integration has the potential to address these issues for high volume applications, but successful integration in one material system has eluded optics for some time. Chapter 6 described some of the background behind the recent effort to accomplish hybridized photonic/electronic integration using silicon CMOS processes on a Silicon-on-Insulator (SOI) platform. Leveraging the processing knowledge of the electronic semiconductor industry can help achieve high yields and better fabrication tolerances in optics as well. The superficial silicon of SOI forms a natural waveguiding layer as well, offering a medium where photonics and electronics could possibly co-exist. In addition, SOI is a high index contrast material system allowing much larger scales of photonic integration due to smaller bend radii and greater optical confinement. Silicon, however, is not a material conducive to making light sources, thus requiring light to be coupled into the chip from an external source. This requires the design of an efficient interface to couple light from single mode optical fiber into thin film SOI photonic integrated circuits. This is a non-trivial problem requiring considerable engineering and computation.

Chapter 7 described some of the issues confronting the design of low insertion loss grating coupler interfaces. We showed how the beams that are produced when a leaky wave surface like a grating coupler is excited by an incident beam, consist of multiple components that may be balanced against each other to achieve high efficiencies through the creation of desirable interference patterns. In order to gain control over the amplitudes and phases of the beams, we proposed the optimization of the BOX layer together with the addition and optimization of three high index contrast layers above the grating structure. The layer structure could be optimized using a transmission matrix approach along with the complex scattering matrix of the grating. To obtain the complex scattering matrix, however, we need a full solution of Maxwell's equations in the grating region. In order to perform a proof-of-concept design while avoiding computational complexity, we proposed the use of a transmission matrix approach to designing the layer structure, while treating the grating as a very weak perturbation. In order to make the approximation as valid as possible, we proposed the use of a shallow and long grating. In addition to the dielectric stack, it is necessary to tailor the strength of the grating along its length to optimize coupling from a Gaussian beam. The grating needs to start very weak, with strength that increases gradually along its length. The improvement in insertion loss, however, is limited by how weak the grating can be made. In planar CMOS processes, since the depth of the grating cannot be varied along its length, strength is controlled through changes in duty cycle. The insertion loss improvement thus becomes limited by the maximum achievable lithographic resolution.

In Chapter 8, we described a process flow for the fabrication of the grating couplers embedded in a high index contrast stack. Electron beam lithography was used to achieve the resolution required for grating fabrication, but the dimensions of the devices are well within the reach of photolithography. We chose to house the grating in an oxide layer deposited right above the superficial silicon, on account of the control it gave us over the grating depth. In a commercial CMOS fabrication facility, however, the grating could be implemented by partially etching the silicon layer using a controlled etch. To planarize the devices, we backfilled the grating with amorphous silicon, however commercial polishing processes are capable of achieving the accurate thicknesses required..

Chapter 9 described the characterization of the grating couplers. We used a setup that allowed variations in the width, angle, wavelength and polarization of the incident input beam. This allowed us maximum control in order to compensate for inaccuracy in the design of the grating parameters. Experiments yielded a best insertion loss of 5.9 dB at a wavelength of 1526.5 nm. The 3 dB bandwidth of the device was 8 nm. The bandwidth limitation arises due to the large incident beam width and the length of the grating coupler. A larger beamwidth falling on a longer coupler, results in the illumination of more grating periods, thus defining the momentum more precisely. This reduces the coupling bandwidth of the grating. In fiber-waveguide coupling, the bandwidth would be restricted by the spot size obtained from single mode fiber.

The grating coupler is a key enabling device for an integrated high index contrast technology. The coupler is, however, by nature an inefficient device. In order to enhance its efficiency, considerable engineering is necessary. This engineering usually takes the form of controlling the optical power distribution in various beams in the vicinity of the grating, and created by the grating itself. SOI offers us control over the distribution of power around a grating, by providing us with two high index contrast interfaces below the grating. We showed in this dissertation that efficiency may be enhanced by designing the BOX layer in concert with an overlying high index contrast dielectric stack. The optimized design of such stacks and the grating itself is a computationally intensive exercise requiring the rigorous solution of Maxwell’s equations. If the grating and its accompanying stack structure are properly optimized using complete solutions to Maxwell’s equations, very low insertion losses may be achieved.

Bibliography

1. H. Taub and D.L. Schilling, “Principles of Communication Systems”, *McGraw Hill Book Co.*, 1996.
2. G.H. Smith, D. Novak and Z. Ahmed, “Technique for Optical SSB Generation to overcome Dispersion Penalties in Fiber Radio systems”, *Electronics Letters*, vol. 33, no. 1, 2nd January 1997, p. 74
3. B. Davies and J. Conradi, “Hybrid Modulator Structures for Subcarrier and Harmonic Subcarrier Optical Single Sideband”, *Photonics Technology Letters*, vol. 10, no. 4, April 1998, p. 600
4. E. Vergnol, F. Devaux, D. Tanguy and E. Penard, “Integrated Lightwave Millimetric Single Sideband Source: Design and Issues”, *Journal of Lightwave Technology*, vol. 16, no. 7, July 1998, p. 1276
5. G.H. Smith, D. Novak and Z. Ahmed, “Overcoming Chromatic-Dispersion Effects in Fiber-Wireless Systems Incorporating External Modulator”, *IEEE Transactions on Microwave Theory & Techniques*, vol. 45, no. 8, August 1997, p. 1410
6. D. Novak, G.H. Smith, A.J. Lowery, H.F. Liu and R.B. Waterhouse, “Millimeter wave fiber-wireless transmission systems with reduced effects of fiber chromatic dispersion”, *Optical and Quantum Electronics,* vol. 30 (1998), p. 1021
7. D. Wake, I.C. Smith, N.G. Walker, I.D. Hamming and R.D. Carver, *Electronics Letters,* no. 28, 1992, p. 2024
8. J.J. O’Reilly, P.M. Lane, R. Heidemann an R. Hofstetter, *Electronics Letters,* vol. 28, 1992, p. 2309

9. R. Nagarajan, S. Levy and J.E. Bowers, *Journal of Lightwave Technology,* vol. 12 (1994), p. 127

10. J.B, Goerges, M.H. Kiang, K. Heppel, M. Sayed and K.Y. Lau, *Trans on Microwave Theory & Techniques,* vol. 43 (1995), p. 2229

11. D. Novak, Z. Ahmed, R.B. Waterhouse and R.S. Tucker, *Trans on Microwave Theory & Techniques,* vol. 43 (1995), p. 2257

12. D. Wake, C.R. Lima and P.A. Davies, *Trans on Microwave Theory & Techniques,* vol. 43 (1995), p. 2270

13. D. Kim, M. Pelusi, Z. Ahmed, D. Novak, H.F. Liu and Y. Ogawa, *Electronics Letters,* vol. 31 (1995), p. 733

14. Z. Ahmed, H.F. Liu, D. Novak, M.D. Pelusi, Y. Ogawa and D.Y. Kim, *Electronics Letters,* vol. 31 (1995), p. 1254

15. L. Noel, D. Marcenac and D. Wake, *Electronics Letters,* vol. 32 (1996), p. 1997

16. T. E. Darcie, "Subcarrier Multiplexing for Lightwave Networks and Video Distribution Systems", *IEEE J. Select. Areas Commun.,* vol. 8, no. 7, pp. 1240-1248, September 1990

17. W. Zhang, J.A.R. Williams, L.A. Everall, L. Zhang and I. Bennion, "Investigation of Fibre Grating Single Sideband Filtering in a Radio-Fibre System", paper WB4, CLEO Pacific Rim 1999, p. 133

18. S. Haykin, "Communication Systems 3/e", *John Wiley & Sons,* 1995

19. A. Nirmalathas, G.H. Smith and D. Novak, "Sensitivity Analysis of Optical SSB Generation using a dual-electrode Mach-Zehnder modulator", *International Topical Meeting on Microwave Photonics,* Piscataway NJ 1998, p. 79

20. B. Mukherjee, “Optical Communication Networks”, *McGraw Hill,* 1997

21. G.P Agrawal, “Fiber Optic Communication Systems”, *Wiley Interscience*, 1997

22. Y.M. Lin, W.I. Way and G.K. Chang, “A Novel Optical Label Swapping Technique Using Erasable Optical Single-Sideband Sub-carrier label”, *IEEE Photonics Technology Letters,* vol. 12, no. 8, August 2000.

23. G. Rossi, O. Jerphagnon, B.E. Olsson and D.J. Blumenthal, “Optical SCM data extraction using a Fiber-Loop Mirron for WDM Network Systems”, *IEEE Photonics Technology Letters,* vol. 12, no. 7, July 2000.

24. U. Gliese, S. Norskov and T.N. Nielsen, “Chromatic Dispersion in Fiber-Optic Microwave and Millimeter wave links”, *Transactions on Microwave Theory & Techniques,* vol. 44, no. 10, October 1996.

25. M. Sieben, J. Conradi and D.E. Dodds, “Optical Single Sideband Transmission at 10 Gb/s Using only Electrical Dispersion Compensation”, *IEEE Journal of Lightwave Technology*, vol. 17, no. 10, October 1999.

26. U. Gliese, T.N. Nielsen, S. Norskov and K.E. Stubkjaer, “Multifunctional Fiber-Optic Microwave Links Based on Remote Heterodyne Detection”, *Trans on Microwave Theory & Techniques,* vol. 46, no. 5, May 1998.

27. M.Y. Frankel and R.D. Esman, “Optical Single Sideband Suppressed-Carrier Modulator for Wide-Band Signal Processing”, *IEEE Journal of Lightwave Technology,* vol. 16, no. 5, May 1998

28. K. Higuma, S. Oikawa, Y. Hashimoto, H. Nagata and M. Izutsu, “X-cut lithium niobate optical single sideband modulator”, *Electronics Letters,* vol. 37, no. 8, p. 515

29. S. Shimotsu, S. Oikawa, T. Saitou, N. Mitsugi, K. Kubodera, T. Kawanishi and M. Izutsu, “Single Side-Band Modulation Performance of a Lithium Niobate Integrated Modulator Consisting of Four-Phase Modulator Waveguides”, *IEEE Photonics Technology Letters,* vol. 13, no. 4, April 2001.

30. J. Wu and C.L. Lin, “Fiber-optic code division add-drop multiplexers”, *Journal of Lightwave Technology*, vol. 18, no. 6, June 2000, p. 819

31. C.F. Lam, D.T.K. Tong, M.C. Wu and E. Yablonovitch, “Experimental Demonstration of Bipolar Optical CDMA system Using a Balanced Transmitter and Complementary Spectral Encoder”, *IEEE Photonics Technology Letters,* vol. 10, no. 10, Oct 1998, p. 1504

32. R. Soref, “Applications of Silicon-Based Optoelectronics”, MRS Bulletin, pp. 20-24, April 1998.

33. B. Jalali, P.D. Trinh, S. Yegnanarayanan and F. Coppinger, “Guided-wave optics in silicon-on-insulator technology”, IEE Proc. Optoelectronics, Vol. 143, No.5, pp. 307-311, October 1996.

34. B. Jalali, S. Yegnanarayanan et al, “Advances in Silicon-on-Insulator Optoelectronics”, IEEE Journal of Selected Topics in Quantum Electronics, Vol. 4(6), p.938, 1998

35. T. Baba, A. Motegi, T. Iwai, N. Fukaya, Y. Watanabe and A. Sakai, “Light Propagation Characteristics of Straight Line Defect Waveguides in Photonic Crystal Slabs Fabricated on a Silicon-on-Insulator substrate”, IEEE Journal of Quantum Electronics, Vol. 38, No. 2, July 2002.

36. S. Coffa, G. Franzo and F. Priolo, “Light Emission from Er-Doped Si: Materials, Properties, Mechanisms and Device Performance”, MRS Bulletin, pp. 25-32, 1998

37. L. Tsybeskov, “Nanocrystalline Silicon for Optoelectronic Applications”, MRS Bulletin, pp. 33-38, 1998

38. E. A. Fitzgerald and L.C. Kimerling, “Silicon-Based Microphotonics and Integrated Optoelectronics”, MRS Bulletin, pp. 39-47, 1998

39. P.G. Kik and A. Polman, “Erbium Doped Optical Waveguide Amplifiers on Silicon”, MRS Bulleting, pp. 48-54, 1998

40. Ch. Buchal and M. Loken, “Silicon Based Metal Semiconductor Metal Detectors”, MRS Bulletin, pp. 55-59, 1998

41. J.C. Sturm, “Advanced Colum IV Epitaxial Materials for Silicon-Based Optoelectronics”, MRS Bulletin, pp. 60-64, 1998.

42. B.E. Little, J.S. Foresi, G. Steinmeyer, E.R. Thoen, S.T. Chu, H.A. Haus, E.P. Ippen, L.C. Kimerling and W. Greene, “Ultra-Compact Si-SiO_2 Microring Resonator Optical Channel Dropping Filters”, IEEE Photonics Technology Letters, Vol. 10, No. 4, April 1998.

43. G. Masini, L. Colace and G. Assanto, “Si based optoelectronics for communications”, Materials Science and Engineering, B89 (2002), 2-9.

44. P.D. Trinh, S. Yegnanarayanan and B. Jalali, “5x9 Integrated Optical Star Coupler Technology”, IEEE Photonics Technology Letter, Vol. 8, No. 6, June 1996.

45. P. Dainesi, A. Kung, M. Chabloz, A. Lagos, Ph. Fluckiger, A. Ionescu, P. Fazan, M. Declerq, Ph. Renaud and Ph. Robert, “CMOS Compatible Fully Integrated Mach-

Zehnder interferometer in SOI Technology", IEEE Photonics Technology Letters, Vol. 12, No. 6, June 2000.

46. A. Liu, R. Jones, L. Liao, D.S. Rubio, D. Rubin, O. Cohen, R. Nicolaescu and M. Paniccia, "A high speed Silicon optical modulator based on a metal-oxide-semiconductor capacitor", Nature, Vol. 427, 12 February 2004.
47. C.K. Tang and G.T. Reed, "Highly efficient optical phase modulator in SOI waveguides", Electronics Letters, Vol. 31, No. 6, p. 451.
48. Landru N, Pascal D, Koster A, Laval S. "Optical modulation at 1.3 mu m on silicon-on-insulator (SIMOX) standard substrate for spatial light modulator applications." Electronics Letters, vol.36, no.2, 20 Jan. 2000, pp.161-3. Publisher: IEE, UK.
49. Cutolo A, Iodice M, Spirito P, Zeni L, "Silicon electro-optic modulator based on a three terminal device integrated in a low-loss single-mode SOI waveguide", Journal of Lightwave Technology, vol.15, no.3, March 1997, pp.505-18. Publisher: IEEE, USA.
50. Masini G, Colace L, Assanto G. 2.5 gbit/s polycrystalline germanium-on-silicon photodetector operating from 1.3 to 1.55 μm", Applied Physics Letters, vol.82, no.15, 14 April 2003, pp.2524-6. Publisher: AIP, USA.
51. Fama S, Colace L, Masini G, Assanto G, Hsin-Chiao Luan, "High performance germanium-on-silicon detectors for optical communications", Applied Physics Letters, vol.81, no.4, 22 July 2002, pp.586-8.

52. O. Boyraz and B. Jalali, “Demonstration of a Silicon Raman Laser”, Optics Express, Vol. 12, No. 21, p. 5269.

53. T. Tamir (Editor), “Integrated Optics”, Topics in Applied Physics Vol. 7, Springer-Verlag, 1975.

54. Tamir T, Peng ST. “Analysis and design of grating couplers.”, Applied Physics, vol.14, no.3, Nov. 1977, pp.235-54.

55. Shuzhang Zhang, Tamir T. “Analysis and design of broadband grating couplers.”, IEEE Journal of Quantum Electronics, vol.29, no.11, Nov. 1993, pp.2813-24

56. R. Petit (Editor), “Electromagnetic Theory of Gratings”, Topics in Current Physics, Vol. 22, Springer-Verlag, 1980.

57. M.D. Salik, P. Chavel, “Resonant Excitation Analysis of waveguide grating couplers”, Optics Communications, 193(2001), pp. 127-131.

58. N. Landru, D. Pascal, A. Koster, “Modelling of two-dimensional grating couplers on silicon-on-insulator waveguides using a beam-propagation method”, Optics Communications, 196(2001), pp. 139-147.

59. R.M. Emmons and D.G. Hall, “Buried-Oxide Silicon-On-Insulator Structures II: Waveguide Grating Couplers”, IEEE Journal of Quantum Electronicss, Vol. 28, No.1, January 1992.

60. M.L. Dakss, L. Kuhn, P.F. Heindrich and B.A. Scott, Applied Physics Letters, Vol. 16, pp. 523 (1970)

61. M. Neviere, R. Petit and M. Cadilhac, “About the Theory of optical Grating Coupler-Waveguide Systems”, Optics Communications, Vol. 8, No. 2, June 1973.

62. M. Neviere, P. Vincent, R. Petit and M. Cadilhac, “Determination of the Coupling Coefficient of a Holographic Thin Film Coupler”, Optics Communications, Vol. 9, No. 3, Nov. 1973.

63. J.H. Harris, R.K. Winn and D.G. Dalgoutte, “Theory and Design of Periodic Couplers”, Applied Optics, Vol. 11, No. 10, October, 1972.

64. S.T. Peng, T. Tamir and H.L Bertoni, “Theory of Periodic Dielectric Waveguides”, IEEE Transactions on Microwave Theory & Techniques, Vol. MTT-23, No. 1 , January 1975.

65. R. Ulrich, “Optimum Excitation of Optical Surface Waves”, Journal of the Optical Society of America, Vol. 61, No. 11, November 1971.

66. Yariv A, “Coupled-mode theory for guided-wave optics”, IEEE Journal of Quantum Electronics, vol.QE9, no.9, Sept. 1973, pp.919-33.

67. Dalgoutte DG. “A high efficiency thin grating coupler for integrated optics”, Optics Communications, vol.8, no.2, June 1973, pp.124-7.

68. Aoyagi T, Aoyagi Y, Namba S. "High efficiency blazed grating couplers", Applied Physics Letters, vol.29, no.5, 1 Sept. 1976, pp.303-4.
69. Chang KC, Shah V, Tamir T., "Scattering and guiding of waves by dielectric gratings with arbitrary profiles.", Journal of the Optical Society of America, vol.70, no.7, July 1980, pp.804-13.
70. Streifer W, Burnham RD, Scifres DR., "Analysis of grating-coupled radiation in GaAs:GaAlAs lasers and waveguides. II. Blazing effects.", IEEE Journal of Quantum Electronics, vol.QE-12, no.8, Aug. 1976, pp.494-9.
71. Ming Li, Sheard SJ., "Waveguide couplers using parallelogramic-shaped blazed gratings.", Optics Communications, vol.109, no.3-4, 1 July 1994, pp.239-45.
72. Hagberg M, Eriksson N, Larsson A., "Investigation of high-efficiency surface-emitting lasers with blazed grating outcouplers.", IEEE Journal of Quantum Electronics, vol.32, no.9, Sept. 1996, pp.1596-605
73. Chang KC, Tamir T., "Bragg-reflection approach for blazed dielectric gratings.", Optics Communications, vol.26, no.3, Sept. 1978, pp.327-30.
74. Chang KC, Tamir T., "Simplified approach to surface-wave scattering by blazed dielectric gratings.", Applied Optics, vol.19, no.2, 15 Jan. 1980, pp.282-8.
75. Peng ST, Tamir T., "Directional blazing of waves guided by asymmetrical dielectric gratings.", Optics Communications, vol.11, no.4, Aug. 1974, pp.405-9.
76. Gruss A, Tam KT, Tamir T., "Blazed dielectric gratings with high beam-coupling efficiencies.", Applied Physics Letters, vol.36, no.7, 1 April 1980, pp.523-5.
77. Ang TW, Reed GT, Evans AGR, Routley PR, Josey MR., "Fabrication of silicon-blazed gratings for couplers.", Fiber & Integrated Optics, vol.19, no.1, 2000, pp.25-9.

78. Ming Li, Sheard SJ. “Experimental study of waveguide grating couplers with parallelogramic tooth profiles.”, Optical Engineering, vol.35, no.11, Nov. 1996, pp.3101-6.

79. Laao T, Sheard S, Ming Li, Hanguo Zhu, Prewett P. “High-efficiency focusing waveguide grating coupler with parallelogramic groove profiles.”, Journal of Lightwave Technology, vol.15, no.7, July 1997, pp.1142-8.

80. T. Shiono and H. Ogawa, “Planar-optic-disk pickup with diffractive micro-optics”, Applied Optics, Vol. 33, No. 31, 1 November 1994.

81. J.C. Lehureau, “Impact of diffractive optics on the design of optical pick up”, SPIE Vol. 2783, pp. 22-29.

82. Orobtchouk R, Layadi A, Gualous H, Pascal D, Koster A, Laval S. “High-efficiency light coupling in a submicrometric silicon-on-insulator waveguide.”, Applied Optics, vol.39, no.31, 1 Nov. 2000, pp.5773-7.

83. Ang TW, Reed GT, Vonsovici A, Evans AGR, Routley PR, Josey MR. “Highly efficient unibond silicon-on-insulator blazed grating couplers.”, Applied Physics Letters, vol.77, no.25, 18 Dec. 2000, pp.4214-16.

84. Taillaert D, Bogaerts W, Bienstman P, Krauss TF, Van Daele P, Moerman I, Verstuyft S, De Mesel K, Baets R. “An out-of-plane grating coupler for efficient butt-coupling between compact planar waveguides and single-mode fibers.”, IEEE Journal of Quantum Electronics, vol.38, no.7, July 2002, pp.949-55.

85. Ulrich R. “Efficiency of optical-grating couplers.”, Journal of the Optical Society of America, vol.63, no.11, Nov. 1973, pp.1419-31

86. Tamir T, Bertoni HL. “Lateral displacement of optical beams at multilayered and periodic structures.”, Journal of the Optical Society of America, vol.61, no.10, Oct. 1971, pp.1397-413.

87. Ang TW, Reed GT, Vonsovici A, Evans AGR, Routley PR, Josey MR. “Effects of grating heights on highly efficient unibond SOI waveguide grating couplers.”, IEEE Photonics Technology Letters, vol.12, no.1, Jan. 2000, pp.59-61.

88. Waldhausl R, Schnabel B, Dannberg P, Kley E-B, Brauer A, Karthe W. “Efficient coupling into polymer waveguides by gratings.”, Applied Optics, vol.36, no.36, 20 Dec. 1997, pp.9383-90.

89. P. Yeh, “Optical Waves in Layered Media”, Wiley-Interscience, 1988.

90. Lee KK, Lim DR, Kimerling LC, Shin J, Cerrina F. “Fabrication of ultralow-loss Si/SiO/sub 2/ waveguides by roughness reduction.”, Optics Letters, vol.26, no.23, 1 Dec. 2001, pp.1888-90.

91. Yang-Kyu Choi, Leland Chang, Ranade P, Jeong-Soo Lee, Daewon Ha, Balasubramanian S, Agarwal A, Ameen M, Tsu-Jae King, Bokor J. “FinFET process refinements for improved mobility and gate work function engineering.”, International Electron Devices Meeting. Technical Digest (Cat. No.02CH37358). IEEE. 2002, pp.259-62.

92. Rueger NR, Doemling MF, Schaepkens M, Beulens JJ, Standaert TEFM, Oehrlein GS. “Selective etching of SiO/sub 2/ over polycrystalline silicon using CHF/sub 3/ in an inductively coupled plasma reactor.”, Journal of Vacuum Science & Technology A-Vacuum Surfaces & Films, vol.17, no.5, Sept. 1999, pp.2492-502.

93. P.R. Bandaru, private communication.

94. Waldausl R, Schnabel B, Kley E-B, Brauer A. "Efficient focusing polymer waveguide grating couplers", Electronics Letters, vol.33, no.7, 27 March 1997, pp.623-4.

95. J.M. Merolla, Y. Mazurenko, J.P. Goedgebuer and W.T. Rhodes, "Single photon interference in Sidebands of Phase-Modulated Light for Quantum Cryptography", Physical Review Letters, vol. 82, no. 8, February 1999.

96. K. Kitayama, "Highly Spectrum Efficient OFDM/PDM Wireless Networks by using Optical SSB Modulation", IEEE Journal of Lightwave Technology, vol. 16, no. 6, p. 969, June 1998.